

UNIVERSITA' DEGLI STUDI DI NAPOLI FEDERICO II



DEPARTMENT OF INDUSTRIAL ENGINEERING

PH.D. THESIS IN INDUSTRIAL ENGINEERING

**AERO-THERMO-ELASTIC METHODS FOR THE
ANALYSIS OF AN HYPERSONIC DEPLOYABLE
AERODYNAMIC DECELERATOR**

Tutors:

Prof. Sergio De Rosa

Prof. Francesco Franco

Prof. Raffaele Savino

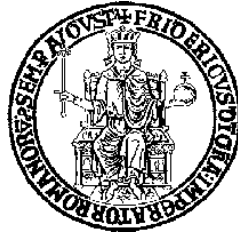
Chairman:

Prof. Michele Grassi

Candidate:

Ing. Pietro Pasolini

UNIVERSITA' DEGLI STUDI DI NAPOLI FEDERICO II



DEPARTMENT OF INDUSTRIAL ENGINEERING



PH.D. THESIS IN INDUSTRIAL ENGINEERING

**AERO-THERMO-ELASTIC METHODS FOR THE
ANALYSIS OF AN HYPERSONIC DEPLOYABLE
AERODYNAMIC DECELERATOR**

Tutors:

Prof. Sergio De Rosa

Prof. Francesco Franco

Prof. Raffaele Savino

Chairman:

Prof. Michele Grassi

Candidate:

Ing. Pietro Pasolini

SHEMA (DT 6, 4-9)

HEAR, O ISRAEL!

THE LORD IS OUR GOD, THE LORD IS ONE!

YOU SHALL LOVE THE LORD YOUR GOD

WITH ALL YOUR HEART,

WITH ALL YOUR SOUL AND WITH ALL YOUR MIGHT.

THESE WORDS, WHICH I AM COMMANDING YOU

TODAY, SHALL BE ON YOUR HEART.

YOU SHALL TEACH THEM DILIGENTLY

TO YOUR SONS AND SHALL TALK OF THEM WHEN

YOU SIT IN YOUR HOUSE

AND WHEN YOU WALK BY THE WAY AND WHEN YOU

LIE DOWN AND WHEN YOU RISE UP.

YOU SHALL BIND THEM AS A SIGN ON YOUR HAND

AND THEY SHALL BE AS FRONTALS

ON YOUR FOREHEAD.

YOU SHALL WRITE THEM ON THE DOORPOSTS OF

YOUR HOUSE AND ON YOUR GATES.

Acknowledgements

At the end of a journey lasted three years saying thanks to all the people that you met on your way is almost impossible, but I will try to accomplish this hard task.

First, of course, I have to mention my tutors, Pr. Sergio De Rosa, Pr. Francesco Franco and Pr. Raffaele Savino; they have been more than just supervisors, they have been a guide to me. Thank you for your advices, thank you because you showed me that is it possible to be a good worker and an awesome person at the same time. If I only become the half of the man that you are, I know for sure that I would have no problem in my future.

Then, I want to express my thanks to Dr. Dowell. I will never forget our meetings. Even though you are the “Michael Jordan” of the aeroelasticity, you were humble and always open to suggestion. I will jealously keep your notes, and one day I will read them, and I will remember that to change the world with kindness, humility and professionalism is possible.

Obviously, great thanks goes to my office-mates Giuseppe e Vittorio. Thank you for the time spent together, for all your advices, and for all the time that I wasted yours with my stupid questions. I could not ask for better colleagues.

Now it is U.S. time. I want to thank all the people that made my visiting experience amazing.

First of all the Italian crew. Thank you Clarice, for your kindness and joy. Thank you Lidia, you are one of the most helpful person I have ever met. But most of all thank you Maria, I will never forget when we met the first day, I was scared in the hall of your lab because everything was new for me, and after you walked down the stairs and we had lunch together I went home relieved, because I knew that I had found a great friend.

Then I want to thanks Michal, I will miss our speech in the office, thanks to you I grew up not only as a man, but as a believer too, and I have a new point of view of the religion.

How not to mention the U.S. crew: Kevin, David and Mauricio. I will never forget our pool games, our “drunk” trips, our soccer games, and how you made me feel like one of you even if I was a stranger at the beginning.

Every decent acknowledgment has a part dedicated to the friends that you have grown up with. In my case, this part would be longer than the PhD thesis itself. I cannot mention

just a few friends that meant something to me, because they are a lot and I thank God for that. First of all, Sergio, I have no words to describe the bond that we share, you are more than just a friend, you are a brother to me; thank you for your support and for your help in times of need. Thank you Nicola, even if we have known each other all our lives, we will be friends forever. Thank you Daniele, even though you chose me as your best man at your wedding, your best gift to me was the birth of your daughter Irene, I'll try to be the best uncle for her and for all the nephews that will come. Thank you Diego, Peppe, Roberto, Ennie, Bruno, Checca, Liana, Martina, Chiara, Annamaria, Flavia, Stefania, Claudia, Fabiana, Marcella, Orlando (I hope I didn't forget anyone), you made my life worth to be lived. Special thanks goes to my little brothers of the group "Sole in Fiamme" and my co-"educators". You made me feel that everything is possible with God.

Of course, my family covers the most important part of this page. Without you, dad and mom, I wouldn't be the person that I am. I hope that you'll be always proud of me.

Last, but not the least, the person who has changed my life. Before you, Chiara, I was lost in a life without any purpose. I know for sure that God has prepared a common path for the both of us. You have filled my life with joy and love, and you have always been my first supporter. I'm looking forward for a life together and I know that the flame of our love will never be extinguished.

Preface and Goals

Only in the last decade, the interest in structures with flexible deployable/inflatable Thermal Protection System (TPS) for atmospheric entry has received a significant improvement. Several space missions, requiring entry in different planets atmospheres including Earth, Mars, Titan, and Neptune, are being studied.

The characterization of the Aero-Thermo-Elastic (ATE) behavior of a flexible structure during atmospheric entry is a Fluid-Structure-Interaction (FSI) problem. The deflection of the flexible TPS subjected to aerodynamic and thermal loads influences the flow field, modifying in turn the thermal and aerodynamic behaviors. If this loop of influences results in an energy extraction from the flow stream, the structure may experience flutter, resulting in a self-oscillation of the structure, and in an eventual failure.

Figure 1 shows the accuracy level required from each subject of the hypersonic Aero-thermo-elasticity of flexible structures.

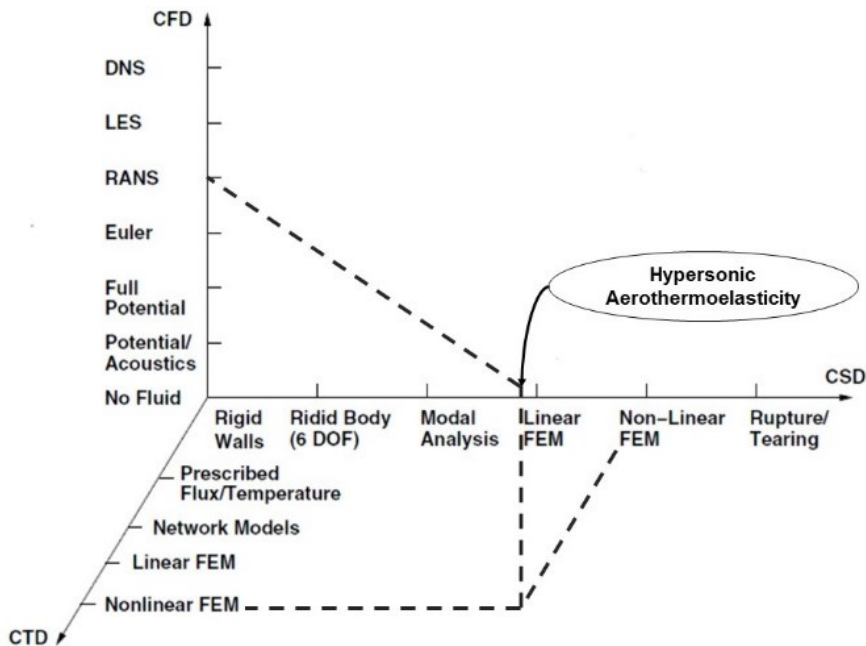


Figure 1 - Fluid-Structure-Thermal Interaction Solutions using Computational Structural Dynamic, Computational Thermo-Dynamic, and Computational Fluid Dynamic analysis methods.

Furthermore, Computational Aero-Thermo-Elasticity (CATE) generally refers to the coupling of high-level Computational Fluid Dynamic (CFD) solvers with high-level structural dynamic solvers (generally using FEA approach).

In order to discuss the ATE problem, it is useful to extend the well known Collar's triangle [1] to a rectangle (see Figure 2). In general, there are various degrees of coupling among all the rectangle elements.

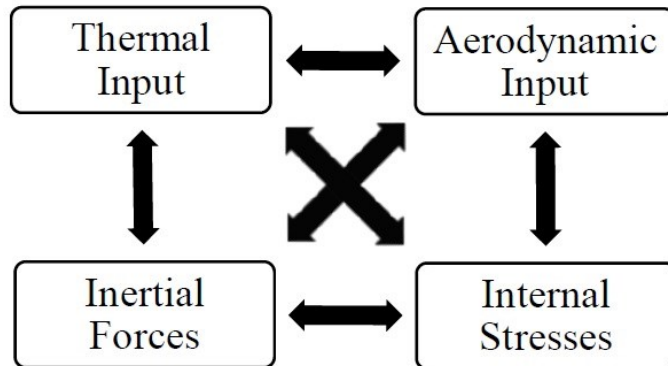


Figure 2 - Aero-thermo-elastic (ATE) rectangle [1].

Due to the complexity of the ATE problem, it is common use to uncouple the ATE rectangle.

For example, the ATE coupling is conceivable if the aero-thermal (AT) characteristic time, given by the ratio between the square of the characteristic length and the thermal diffusivity of the material, is comparable to the aero-elastic (AE) characteristic time, given by the ratio between one to natural frequency of the structure.

Even though it is possible to reduce the computational cost of the problem uncoupling the parts of the ATE rectangle, the costs in terms of money and computational time of the non-linear ATE calculation are still quite high.

It is for the aforementioned reasons that it is needed to provide us with theoretical and experimental non-linear tools capable of give us a preliminary indication of the ATE behavior of the structure.

The aim of this PhD thesis will be focused on the assessment and validation of non-linear AE and AT computational methodologies of a flexible structure, to this end more than one deployable configuration will be presented.

In order to carry out a numerical preliminary aero-thermo-dynamic and AE investigation of a flexible TPS structure, it would be helpful to perform:

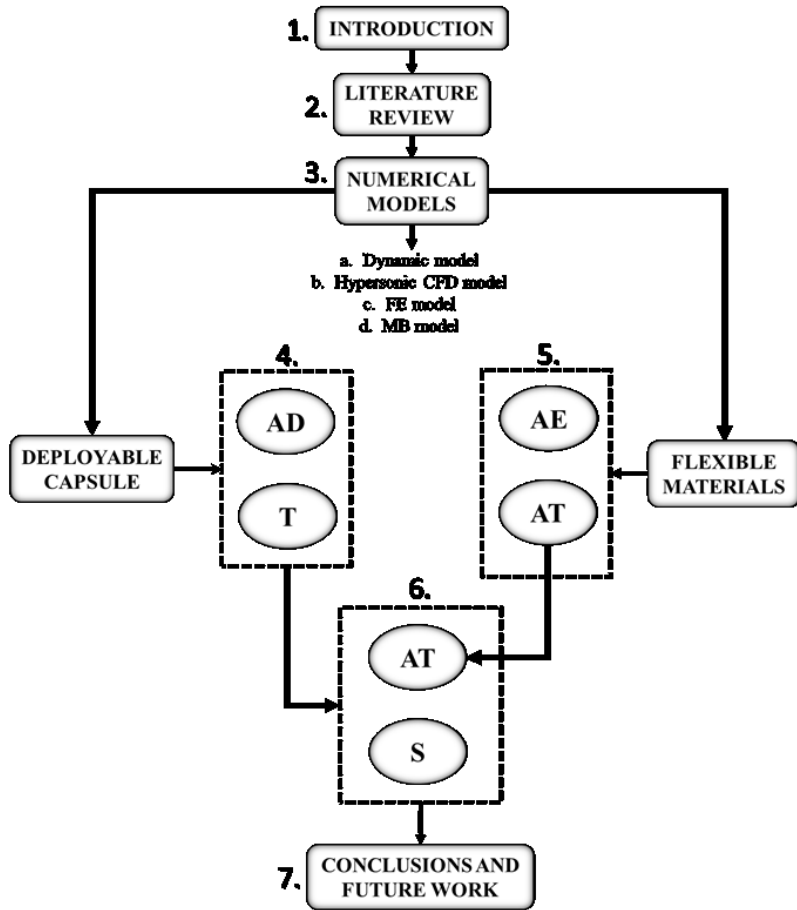
- A preliminary evaluation of the main aerodynamic (AD) and thermal (T) parameters in hypersonic flow conditions of a deployable capsule.
- An AE and AT study of the material types and configurations capable of facing the dynamic and thermal loads during the operative life of the capsule.
- An AT and Structural (S) assessment of the thermal and dynamic loads influence on the deployable capsule configuration in hypersonic flow conditions.

Therefore, in order to show a computational methodology to preliminary evaluate the main dynamic and thermal loads of a deployable capsule in hypersonic flow conditions, the EDL study of the Small Mars Satellite (SMS) mission will be presented.

Furthermore, the AT study of a material layup will be discussed, in order to present a loosely coupled FSI partitioned approach based on the integration of structural and CFD commercial software. Thus, the AE behavior of a square flexible TPS will be studied, in order to present and validate a simplified non-linear analytical tool capable to derive the equations of motion using a numerical code based on the natural modes of the structure (MB).

Finally, the aforementioned FSI coupled approach will be applied to evaluate the AT response of a deployable capsule configuration in hypersonic flow conditions. While a non-linear FEA of the TPS flexible texture will be performed, in order to evaluate the structural behavior of the capsule structure in the same hypersonic flow conditions.

In Figure 3, a flow chart of the thesis organization is reported.



AD=Aerodynamic Analysis
T=Thermal Analysis
AE=Aero-Elastic Analysis
AT=Aero-Thermal Analysis
S=Structural Analysis

Figure 3 – Flow chart of the thesis outline

Table of Contents

Preface and Goals	6
1. Introduction	18
1.1 Outline of Thesis.....	19
1.2 Introduction to the HIAD and HDAD configurations: Present and Past.....	21
1.3 Advantages of using a deployable/inflatable aerobrake for atmospheric entry.....	25
2. Aero-Elastic and Aero-Thermo-Elastic Theories for Hypersonic Applications: State-of-the-Art	27
2.1. FSI approach for Aero-thermo-elastic applications.....	28
2.2. Current ATE studies of flexible TPS.....	33
3. Numerical Models	39
3.1 Dynamic models.....	39
3.2 Hypersonic CFD model.....	41
3.3 Non-linear FE model.....	44
3.4 Non-linear theoretical model based on the natural modes of the structure.....	47
4. Aerodynamic (AD) and Thermal (T) Analysis of a Deployable Capsule	51
4.1 Preliminary aerodynamic and thermal analysis.....	52
4.2 Hypersonic CFD aerothermodynamics.....	58
5. Aero-Thermal (AT) and Aero-Elastic (AE) Analysis of Flexible Materials	71
5.1 AT response of a multi-layer TPS using a FSI loosely coupled approach.....	71
5.2 Non-linear AE response of a multi-layer TPS.....	77
5.2.1 Structural non-linear response of the TPS.....	79
5.2.2 AE non-linear response of the TPS surrounded by hypersonic flow.....	87
6. Aero-Thermal (AT) and Structural (S) Analysis of a Deployable Capsule	98
6.1 Aero-Thermal analysis (AT).....	102
6.2 Structural analysis (S).....	107
7. Conclusions and Future Work	110
Appendix I	112
References	115

List of Figures

Figure 1 - Fluid-Structure-Thermal Interaction Solutions using Computational Structural Dynamic, Computational Thermo-Dynamic, and Computational Fluid Dynamic analysis methods.....	6
Figure 2 - Aero-thermo-elastic (ATE) rectangle [1].....	7
Figure 3 – Flow chart of the thesis outline	9
Figure 1.1 – Evolution of the HIAD/HDAD concept	18
Figure 1.1.1 – Flow chart of the thesis outline.....	20
Figure 1.2.1– The Parashield concept in deployed (left) and closed (right) configuration [2].....	21
Figure 1.2.2 – An artistic view of the IRDT capsule from Space [3].....	22
Figure 1.2.3- An artistic view of the IRVE-3 capsule from Space.....	22
Figure 1.2.4 - Nominal Entry, Descent, and Landing for the MER mission [17].	23
Figure 1.2.5 - EDL sequence of events for SMS [23].....	24
Figure 1.3.1 – Comparison among different entry trajectory parameters as a function of the ballistic coefficients: Mach number (a), Flight duration (b), Stagnation point pressure (c), Heat Flux (d). [7].....	26
Figure 2.1 - History of IAD technology development efforts [24].	28
Figure 2.1.1 - Fluid and Structure solvers for aero-elastic simulation for a closely coupled model [39].....	30
Figure 2.1.2 - Degree of coupling of the ATE problem [27].	31
Figure 2.1.3 - Basic structure of the ATE problem [26].	32
Figure 2.1.4 - Coupled fluid structural analysis [39].	32
Figure 2.1.5 - Generic cycle of the conventional serial staggered procedure [41].	33
Figure 2.2.1 - TPS coupon tensioned over the mounting frame (left), and during GVTs (right) [60].	35
Figure 2.2.2 - TPS coupon mounted in the 8' HTT sled [60].	35
Figure 2.2.3 - Different stages in testing of a 70° half angle afterbody attached ballute [61]......	36
Figure 2.2.4 - Schlieren image for Glenn Research Center Supersonic Wind Tunnel inflatable model [62]......	36
Figure 2.2.5 - IRVE-3 Mission Events [64]......	37
Figure 2.2.6 - Sled loaded with samples [68].	38
Figure 2.2.7 - Test article at the end of the PWT test [22]......	38
Figure 3.1.1 – Sketch of the acting loads on a re-entry capsule.....	40
Figure 4.1 - EDL operation sequence.	51
Figure 4.1.1 - Maximum stagnation point pressure	53
Figure 4.1.2 - Maximum stagnation point heat flux.....	53
Figure 4.1.3 - Maximum stagnation point radiative equilibrium temperature	54
Figure 4.1.4 - Landing velocity	54
Figure 4.1.5 - Mars entry trajectory duration (a), the entry velocity (b), maximum stagnation point pressure (c), the maximum stagnation point heat flux (d), the maximum radiative equilibrium temperature (e) and the Mach number (f).....	55

Figure 4.1.6 – Speed (a), Mach number (b), Stagnation point heat flux (c) and stagnation point pressure (d) of SMS and three previous Mars landers (Viking, MPF and Phoenix)	57
Figure 4.1.7 – SMS landing speed using a subsonic parachute	58
Figure 4.2.1– <i>Knudsen number</i>	59
Figure 4.2.2 - Two-dimensional (a) and three-dimensional (b) CFD mesh.....	60
Figure 4.2.3 - CFD pressure distribution at 30 Km	61
Figure 4.2.4 - CFD pressure distribution at 40 Km	61
Figure 4.2.5 - CFD pressure distribution at 50 Km	62
Figure 4.2.6 - CFD pressure distribution at 60 Km	62
Figure 4.2.7 - CFD pressure distribution at 70 Km	62
Figure 4.2.8 - CFD heat flux distribution at 30 Km.....	63
Figure 4.2.9 - CFD heat flux distribution at 50 Km.....	63
Figure 4.2.10 - CFD heat flux distribution at 70 Km.....	64
Figure 4.2.11 – CFD and Newton theory comparison results.....	64
Figure 4.2.12 – CFD and Tauber/Sutton equation comparison results	65
Figure 4.2.13 – CFD drag coefficient.....	65
Figure 4.2.14 - Mach number (a), Pressure (b) and Temperature (c) contours at maximum stagnation point pressure condition (40 Km)	66
Figure 4.2.15 - Mach number (a), Pressure (b) and Temperature (c) contours at maximum stagnation point heat flux condition (50 Km).....	67
Figure 4.2.16 - CFD surface SMS pressure contour at maximum stagnation point pressure condition (40 Km).....	67
Figure 4.2.17 - CFD surface SMS heat flux contour at maximum stagnation point pressure condition (40 Km)	68
Figure 4.2.18 - CFD surface SMS temperature contour at maximum stagnation point pressure condition (40 Km)	68
Figure 4.2.19 - CFD surface SMS pressure contour at maximum stagnation point heat flux condition (50 Km)	69
Figure 4.2.20 - CFD surface SMS heat flux contour at maximum stagnation point heat flux condition (50 Km)	69
Figure 4.2.21 - CFD surface SMS temperature contour at maximum stagnation point heat flux condition (50 Km)	70
Figure 5.1.2 - Implicit staggered algorithm for each time step	73
Figure 5.1.3 - TPS coupon layout 6 and thermocouple locations	74
Figure 5.1.4 - CFD and FEM coupling models.....	75
Figure 5.1.5 - Comparison between experimental and numerical results at Thermocouple 1 (T1) (a), Thermocouple 2 (T2) (b), and Thermocouple 3 (T3) (c).....	76
Figure 5.2.1 – TPD sample layout	77
Figure 5.2.2 - <i>Finite Element Mesh</i>	78

Figure 5.2.3 – <i>Stitching pattern using spring elements</i>	78
Figure 5.2.1.1 - Non-linear impulse response comparison normalized for the case with $\zeta_{1,2}=0.01$: FFT displacement (a) and FFT acceleration (b).	82
Figure 5.2.1.2 - Non-linear impulse response comparison normalized for the case with $\zeta_{1,2}=0.05$: FFT displacement (a) and FFT acceleration (b).	83
Figure 5.2.1.3 - Non-linear impulse response comparison normalized for the case with $\zeta_{1,2}=0.1$: FFT displacement (a) and FFT acceleration (b).	84
Figure 5.2.1.4 - Non-linear impulse response comparison normalized for the pre-tensioned case with $\zeta_{1,2}=0.01$	85
Figure 5.2.1.5 – Sketch of the TPS under the sinusoidal force applied to the center of the specimen	85
Figure 5.2.1.6 – Time history of the W/th_N ratio for the sinusoidal analysis with $f=17.89$ and $F_{\text{magnitude}}=0.5$	86
Figure 5.2.1.7 –RMS of the W/th_N ratio as a function of the frequency of the TPS for $F_{\text{magnitude}}=0.01, 0.1$ and 0.5 (N): untensioned case	87
Figure 5.2.1.8 - RMS of the W/th_N ratio as a function of the frequency of the TPS for $F_{\text{magnitude}}=0.01, 0.1$ and 0.5 (N): pre-tensioned case	87
Figure 5.2.2.1 - Limit cycle amplitudes as a function of dynamic pressure untensioned (a) and deflection time history at $x/a, x/b=0.8,0.5, AoA=10^\circ$, untensioned (b).....	89
Figure 5.2.2.2 - Non-linear response comparison between experiment and theory for #RUN22 (a) and #RUN23 (b) at $x/a, x/b=0.8,0.5$	90
Figure 5.2.2.3 - Deflection time history comparison at $x/a, x/b=0.8,0.5, AoA=2.5^\circ$, untensioned	92
Figure 5.2.2.4 - Deflection time history comparison at $x/a, x/b=0.8,0.5, AoA=10^\circ$, untensioned	93
Figure 5.2.2.5 - Deflection time history comparison at $x/a, x/b=0.8,0.5, AoA=10^\circ$, pre-tensioned.....	93
Figure 5.2.2.6 - Limit cycle amplitudes as a function of dynamic pressure untensioned (a) and tensioned (b). ..	94
Figure 5.2.2.7 - Sketch of the four different stitching patterns: A (a), B (b), C (c), D (d)	96
Figure 5.2.2.8 - Limit cycle amplitudes as a function of dynamic pressure: pre-tensioned.	97
Figure 5.2.2.9 - Deflection time history comparison at $x/a, x/b=0.8,0.5, AoA=2.5^\circ$, pre-tensioned.....	97
Figure 5.2.2.10 - Deflection time history comparison at $x/a, x/b=0.8,0.5, AoA=5^\circ$, pre-tensioned.....	97
Figure 6.1 - Schematic configuration for a re-entry demonstrator to be testes on board REXUS rocket (half cone angle 45°) [13].....	98
Figure 6.2 - Computing mesh for CFD analyses	99
Figure 6.3 - Maximum heat flux condition CFD Results.....	100
Figure 6.4 - Maximum stagnation point pressure condition CFD results	101
Figure 6.1.1 - Capsule model front (a) and back (b).....	103
Figure 6.1.2 - Temperature distribution front (a) and back (b)	104
Figure 6.1.3 - Capsule body temperature distribution.....	104
Figure 6.1.4 - Temperature distribution front (a), and back (b).....	106
Figure 6.1.5 - Capsule body temperature distribution.....	106
Figure 6.2.1 - Capsule FEM	108

Figure 6.2.2 - TPS deflection magnitude contour	108
Figure 6.2.3 - TPS Von Mises stress contour	109
Figure 6.2.4 – TPS Von Mises stress contour (zoom)	109

List of Tables

Table 4.1.1 - COSPAR Mars Reference Atmosphere Model	52
Table 4.1.2- Mars landers entry parameters [21]	56
Table 4.2.1– Input data to CFD	59
Table 5.1.1 - Definition of low-pressure tunnel conditions [62].....	72
Table 5.1.2 - CFD results comparison	72
Table 5.1.3 - Layup 6 material properties [62]	74
Table 5.2.1 - Material properties of the TPS layers	77
Table 5.2.1.1 – linear MB and FE natural frequencies using the eigenvalue extraction	80
Table 5.2.2.1 - Measured Mach number and dynamic pressure in the 8' HTT [56].....	88
Table 5.2.2.2 - Natural frequencies comparison	91
Table 5.2.2.3 - Natural frequencies.....	96
Table 6.1- Flight conditions at maximum heat flux and max stagnation pressure evaluated by Iacovazzo, Carandente, Savino and Zuppari [13].	99
Table 6.2 – CFD results.....	102
Table 6.1.1 - Capsule thermal materials properties.....	102
Table 6.2.1 - Structural model material properties	107

List of Acronyms

<i>AE</i>	<i>Aero-Elastic</i>
<i>AKK</i>	<i>Aluminized Kapton Kevlar</i>
<i>AoA</i>	<i>Angle of Attack</i>
<i>AT</i>	<i>Aero-Thermal</i>
<i>ATE</i>	<i>Aero-Thermo-Elastic</i>
<i>AUSM</i>	<i>Advanced Upstream Splitting Method</i>
<i>CATE</i>	<i>Computational Aero Thermo Elasticity</i>
<i>CATE</i>	<i>Computational Aero-Thermo-Elasticity</i>
<i>CFD</i>	<i>Computational Fluid Dynamic</i>
<i>EDL</i>	<i>Entry, Descent and Landing</i>
<i>FFT</i>	<i>Fast Fourier Transform</i>
<i>FPA</i>	<i>Flight Path Angle</i>
<i>FSI</i>	<i>Fluid Structure Interaction</i>
<i>GVT</i>	<i>Ground Vibration Test</i>
<i>HDAD</i>	<i>Hypersonic Deployable Aerodynamic Decelerator</i>
<i>HIAD</i>	<i>Hypersonic Inflatable Aerodynamic Decelerator</i>
<i>HHT</i>	<i>Hilbert Hughes Taylor</i>
<i>HTT</i>	<i>High Temperature Tunnel</i>
<i>IRDT</i>	<i>Inflatable Re-entry and Descent Technology</i>
<i>IRENE</i>	<i>Italian Re-Entry Nacelle</i>
<i>IRVE</i>	<i>Inflatable Re-entry Vehicle Experiment</i>
<i>IRVE</i>	<i>Inflatable Re-entry Vehicle Experiment</i>
<i>LCO</i>	<i>Limit Cycle Oscillation</i>
<i>LEO</i>	<i>Low Earth Orbit</i>
<i>MB</i>	<i>Modal Based</i>
<i>MOLA</i>	<i>Mars Orbiter Laser Altimeter</i>
<i>ODE</i>	<i>Ordinary Differential Equation</i>
<i>PT</i>	<i>Piston Theory</i>
<i>RMS</i>	<i>Root Mean Square</i>
<i>SMS</i>	<i>Small Mars Satellite</i>
<i>TC</i>	<i>Test Case</i>
<i>TPS</i>	<i>Thermal Protection System</i>

Nomenclature

a	Sample length
b	Sample width
Cd	Drag coefficient
D	Bending stiffness or Drag
E	Young's modulus
\mathcal{E}	Total energy
F	Airy stress function
$\underline{\mathcal{F}}$	Non-dissipative part of the flux vector
F_{app}	Magnitude force
f_{nm}	Stress function modal coordinate
$\underline{\mathcal{G}}$	Dissipative part of the flux vector
g	Gravity acceleration
h	Material thickness
h_N	Nextel thickness
Kn	Knudsen number
k^{St}	Stitch's spring constant
L	Lift or Lagrangian
M, mass^L	Plate mass per area
N_x, N_y, N_{xy}	In-plane stress resultants
N_x^A, N_y^A	Applied tension in x and y direction
p_0	Stagnation point pressure
q	Dynamic pressure $\frac{1}{2} \rho V^2$
\dot{q}_0	Stagnation point heat flux
q_{nm}	Deflection function modal coordinate
r	Radius of curvature of the trajectory
Rc	Nose curvature radius
$\underline{\mathcal{S}}$	Product vector
T, Tw	Air temperature or kinetic energy and Wall temperature
w	Plate deflection
x_0, y_0	Force location in x and y direction
x_i, y_i	Stitch location in x and y direction
U	Elastic potential energy
U_B, U_S, U^{St}	Bending, Stretching and Stitching energies
$\underline{\mathcal{U}}$	Vector of conserved quantities
\dot{u}, \ddot{u}	Nodal velocity and acceleration
α	HHT numerical stability parameter
α_R, β_R	Damping factors in FEA
β	HHT numerical stability parameter or Ballistic coefficient
γ	HHT numerical stability parameter or Flight path angle
δ	Dirac function

ϕ_{nm}	<i>Mode-shape function</i>
Δp	<i>Pressure loading on panel</i>
λ	<i>Latitude</i>
A	<i>Longitude</i>
ν	<i>Poisson ratio</i>
ζ_i	<i>Critical damping of the i-th mode</i>
σ_d	<i>Damping stress</i>
ψ	<i>Azimuth angle</i>
τ_d	<i>Dissipative part of the stress vector</i>
ω_m	<i>Mars angular velocity</i>
ω_i	<i>Frequency of the i-th mode</i>
ρ	<i>Atmospheric density</i>

1. Introduction

The idea to build capsules with a deployable/inflatable Thermal Protection System (TPS) for atmospheric entry goes back to the 1960s [1], but only recently, in a global scenario where the terms “cheap” and “reusable” play a key role in the aerospace industry, these type of structures have found a place as a valuable substitute of the current aerobreaks technologies. Recent studies have been focused on Hypersonic Inflatable Aerodynamic Decelerator (HIAD) and Hypersonic Deployable Aerodynamic Decelerator (HDAD) technologies.

As shown in Figure 1.1, great effort has been made to study an innovative deployable/inflatable concept in the late ten years.

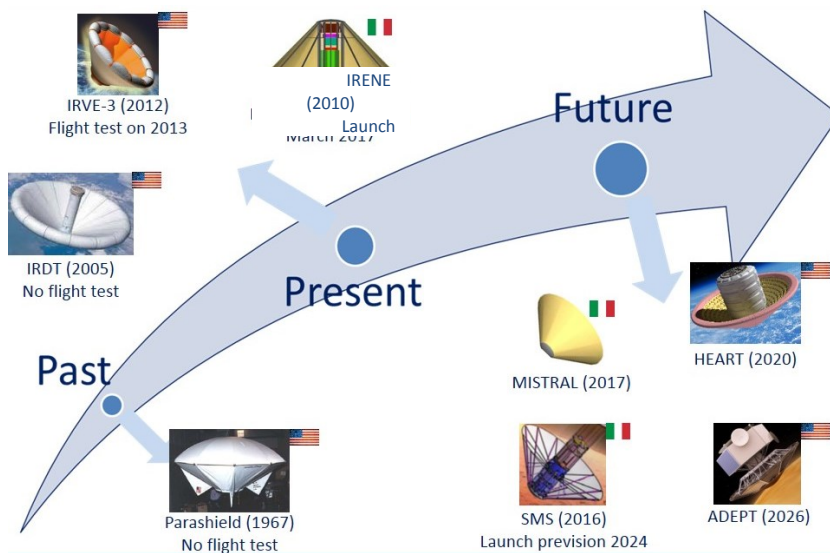


Figure 1.1 – Evolution of the HIAD/HDAD concept

1.1 Outline of Thesis

The thesis is organized as follows.

In Section 1, a brief introduction to the current Earth and Mars deployable/inflatable technologies and a description on the advantage of using a deployable/inflatable TPS are presented.

A literature review of the State-of-the-art AE and ATE computational and experimental methods, focusing on research progress on the FSI behavior of flexible structures, is presented in Section 2.

Then, a description of the numerical models used in this thesis, and the development of a non-linear AE theoretical model, based on the natural modes of the structure, are discussed in Section 3.

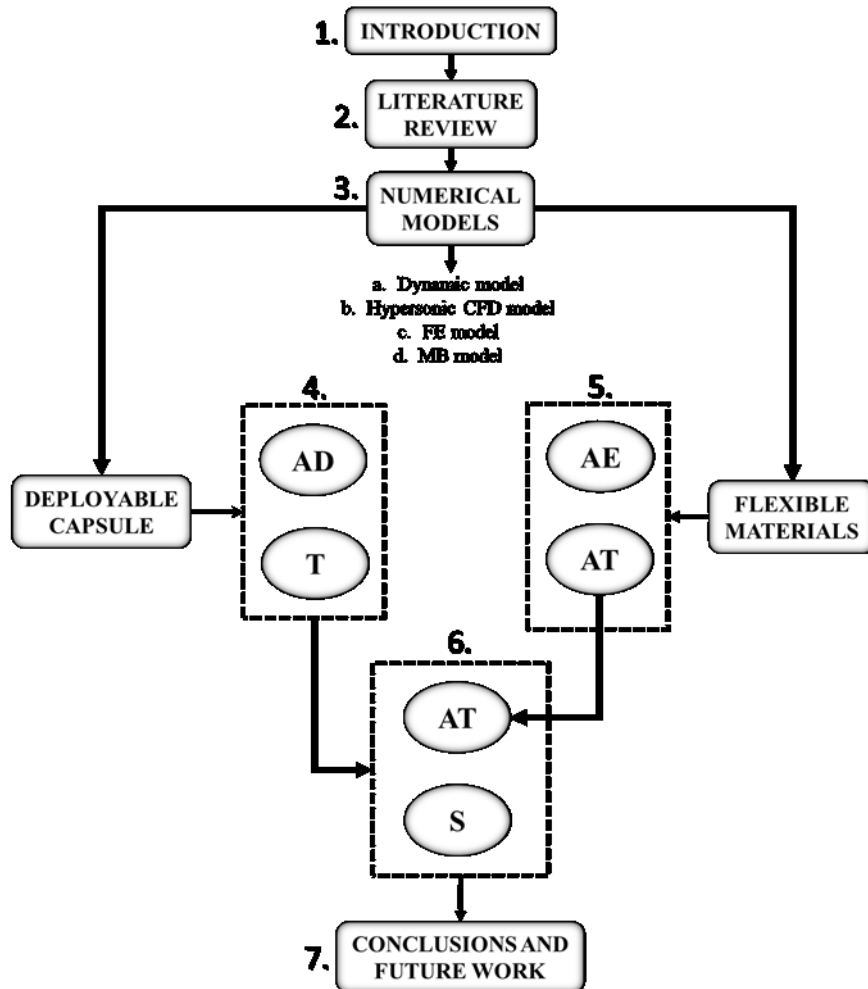
In Section 4, in order to show a computational methodology to preliminary evaluate the main dynamic and thermal loads of a deployable capsule in hypersonic flow conditions, the EDL study of the Small Mars Satellite (SMS) mission is presented. More attention has been placed on the improvements given by the deployable configuration respect to the previous Mars missions, which all mounted a fixed heat shield.

Furthermore, in Section 5, the AT study of a material layup is discussed, in order to present and validate a loosely coupled FSI partitioned approach based on the integration of FE (for the structural domain) and CFD (for the fluid domain) commercial software. Thus, the AE behavior of a multi-layered flexible TPS is studied, in order to present and validate the simplified non-linear analytical tool capable to derive the equations of motion using a numerical code based on the natural modes of the structure (MB) presented in Section 3.

Finally, in Section 6, the AT and the static structural response of a deployable capsule in hypersonic flow conditions during a re-entry trajectory from LEO is presented. First, the FSI loosely coupled approach is applied to evaluate the AT response of the capsule at maximum heat flux conditions during the re-entry path. Then, at maximum stagnation-point pressure conditions, a non-linear FEA of the flexible heat shield has been performed, in order to evaluate the structural resistance of the TPS.

Main conclusions and future work are summarized in Section 7.

In Figure 1.1.1, a flow chart of the thesis organization is reported.



AD=Aerodynamic Analysis
T=Thermal Analysis
AE=Aero-Elastic Analysis
AT=Aero-Thermal Analysis
S=Structural Analysis

Figure 1.1.1 – Flow chart of the thesis outline.

1.2 Introduction to the HIAD and HDAD configurations: Present and Past

Only few concepts for mechanically deployable atmospheric re-entry systems exist. One of the firsts was a deployable capsule, developed by Akin (1990), using an umbrella-like heat shield, made of silicon fabrics, called Parashield [2] (Figure 1.2.1).

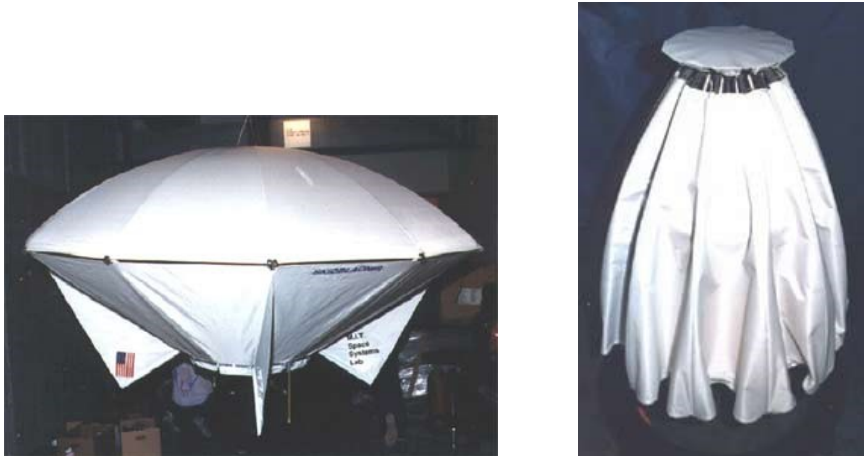


Figure 1.2.1– The Parashield concept in deployed (left) and closed (right) configuration [2].

Great effort has been made during the last decade on the study and testing of HIAD configurations. One of the first examples is the Inflatable Re-entry and Descent Technology (IRDT) [3] (see Figure 1.2.2). Although the flight confirmed the basic feasibility of the technology, both the IRDT-1 mission, scheduled in February 2000, and IRDT-2 mission, scheduled in May 2005, failed.

At this moment, the most advanced program, including experimental flight test and aero-elastic assessments, is the Inflatable Re-entry Vehicle Experiment (IRVE) [3]-[5] (see Figure 1.2.3). Due to the success of the IRVE mission, NASA is currently working on the High Energy Atmospheric Reentry Test (HEART), which is a design concept for a flight test that would demonstrate a larger HIAD with a diameter of almost 8 meters.



Figure 1.2.2 – An artistic view of the IRDT capsule from Space [3].

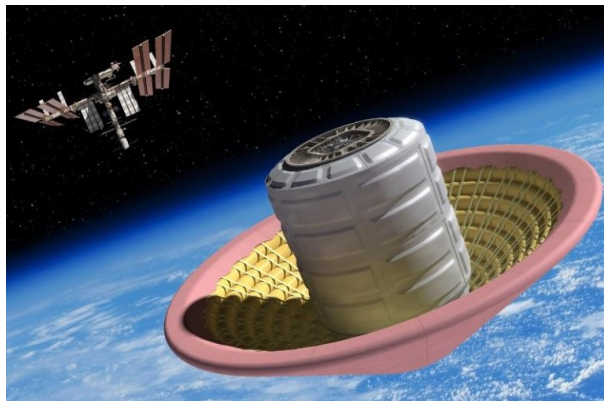


Figure 1.2.3- An artistic view of the IRVE-3 capsule from Space

The University of Naples “Federico II” is currently working in cooperation with other small and medium enterprises, on the development of a Hypersonic Deployable Aerodynamic Decelerator (HDAD) named IRENE (Italian Re-Entry Nacelle) [7] - [13]. This research program, coordinated by the ASI (Agenzia Spaziale Italiana) and the ESA (European Space Agency), has the purpose to demonstrate the possibility to develop, in the near future, a low-cost deployable capsule to enable future space missions, including payloads return on Earth from the ISS and/or recoverable scientific experiments in Low Earth Orbit (LEO).

It is remarkable how, up to now, all previous Mars exploration missions have used a capsule with a fore body fixed heat shield to protect the lander during the high aerodynamic

heating portion of the atmospheric entry. They all had an expensive supersonic parachute system, and sometimes they have employed complex and costly systems based on thrusters and retro-rockets [14] - [16].

Figure 1.2.4 shows a typical EDL sequence of events for the MER mission [17]. As shown a supersonic parachute, and both thrusters and airbag have been used.

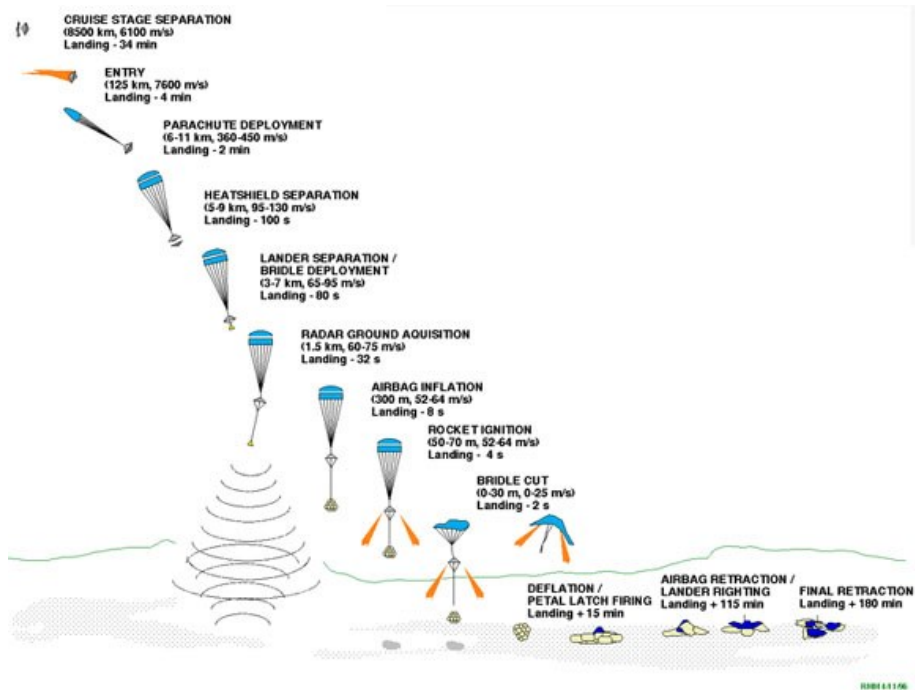


Figure 1.2.4 - Nominal Entry, Descent, and Landing for the MER mission [17].

Recent studies have also investigated the possibility of using the deployable/inflatable technology for the planetary exploration [18] - [20].

Currently, the University of Naples “Federico II”, the Astronomical Observatory of Capodimonte and the Space Studies Institute of Catalonia in cooperation with small and medium enterprises, are studying the development of a deployable capsule for the exploration of the Mars surface, under the program Small Mars Satellite (SMS).

The SMS mission is a proposed mission to Mars, currently under feasibility study promoted and funded by the European Space Agency (ESA). The mission aims at delivering

a small, low-cost lander on the surface of the red planet by using the innovative “umbrella-like” heat shield concept known as IRENE [21] - [23].

The SMS mission has the twofold objective of delivering a small lander to Mars using the deployable heat shield, and of carrying on board a Dust Particle Analyzer (DPA) and an Aerial Drone (AD).

The umbrella-like mechanism has the function of heat shield and aerobrake during Mars entry. The shield is retracted at launch and during the interplanetary cruise. This feature allows adopting a small launcher, such as the European VEGA Rocket, gives higher flexibility in the shield design, and provides advantages achieving a lower ballistic coefficient at planetary entry.

Figure 1.2.5 shows the EDL trajectory of the SMS mission. As shown, thanks to the deployable configuration only a subsonic parachute and a passive shock absorption system (e.g. vented airbags) are necessary for the capsule touch down.

At present, the SMS mission is the most advanced European program for Mars exploration that has the purpose to demonstrate the feasibility of a deployable heat shield as aerodynamic decelerator.

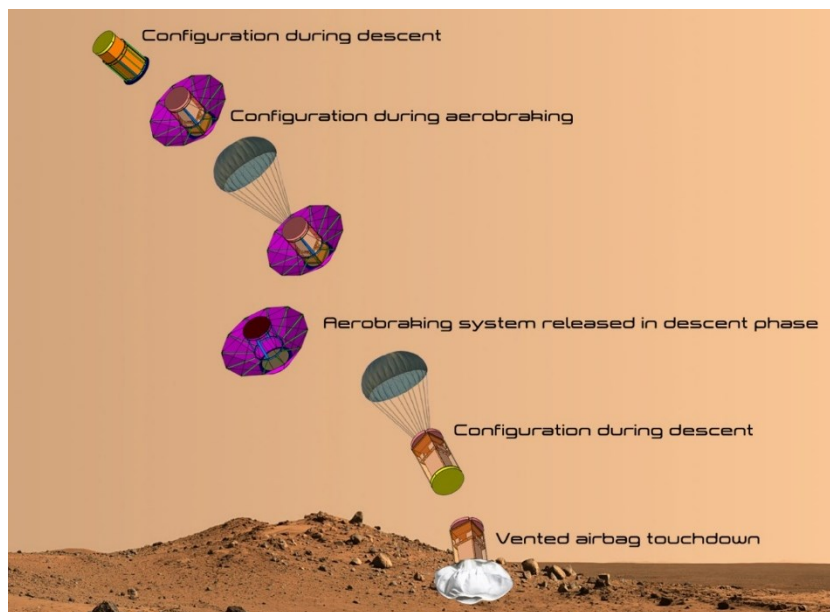


Figure 1.2.5 - EDL sequence of events for SMS [23].

1.3 Advantages of using a deployable/inflatable aerobrake for atmospheric entry

A structure, in which the TPS can be easily accommodated in launch vehicles in a folded configuration and deployed only during re-entry phase, offers the advantage to increase the mass/volume ratio at launch, thereby providing easy payload accommodation in the launcher fairing. When deployed, the ballistic coefficient is relatively low, implying a large deceleration in the upper rarefied region of the atmosphere, with consequent reduction of the thermal and dynamic loads. The above-mentioned ballistic coefficient is defined by the ratio between mass and the product of exposed surface times the drag coefficient.

The reduction of the ballistic coefficient offer several benefits:

- Reduction of the aerodynamic and aero-thermo-dynamic loads along the hypersonic entry flight path.
- Possible use of simplified aerodynamic brake systems, instead of complicated and expensive touch down systems (such as thrusters or supersonic parachutes), since the capsule reaches the subsonic regime at higher altitudes, compared to the existing aero braking systems.
- Improvement of the adaptability of the system, with the possibility to use the flexible shield both as thermal protection system and as aero brake.
- The unique possibility to land at higher altitudes (i.e., higher than MOLA 0 level) with a low-cost system.

Furthermore, the flexibility of the system can offer the advantage to modulate the TPS surface area, in order to control the entry trajectory of the capsule and correctly orient the capsule through the descending path.

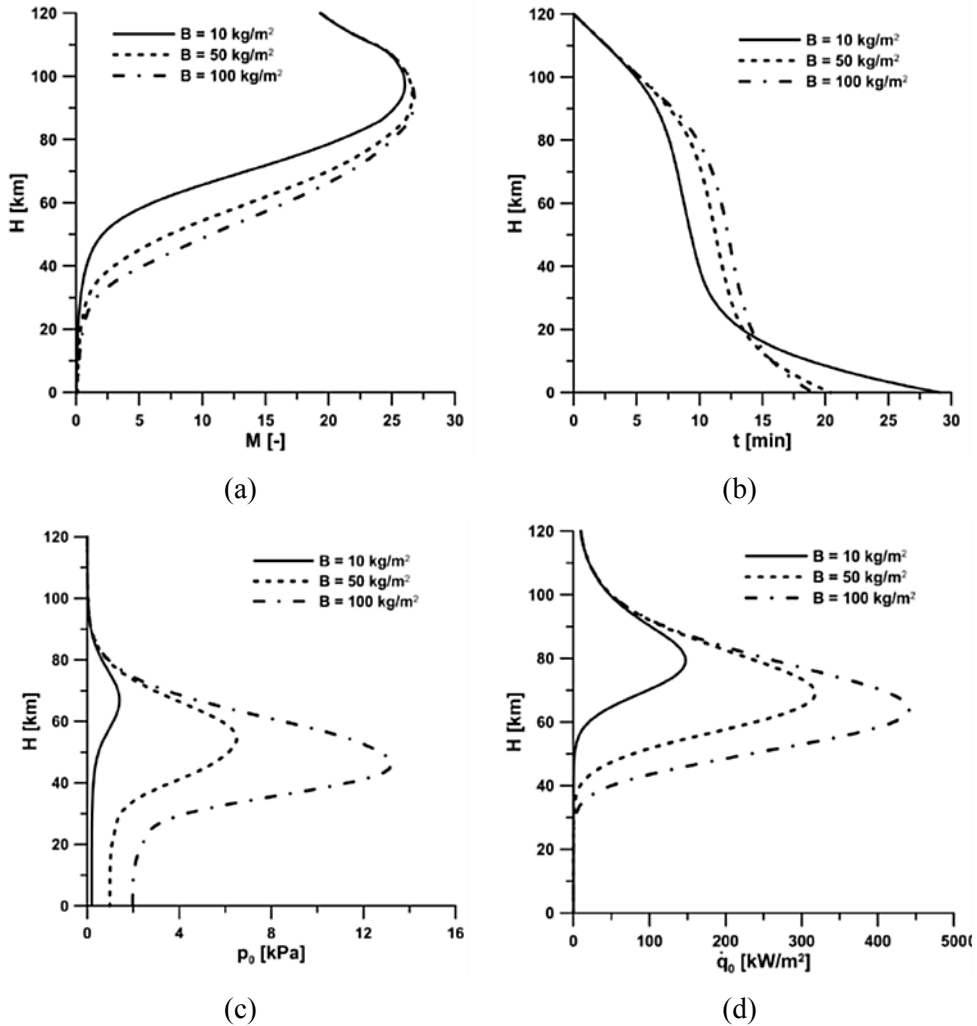


Figure 1.3.1 – Comparison among different entry trajectory parameters as a function of the ballistic coefficients: Mach number (a), Flight duration (b), Stagnation point pressure (c), Heat Flux (d). [7]

As shown in Figure 1.3.1 [7] it is evident that a lower ballistic coefficient offers a reduction of the aerodynamic and thermal loads during the entry phase (see Figure 1.3.1 (c)-(d)), and implies a more significant Mach number reduction at higher altitudes (see Figure 1.3.1 (a)).

2. Aero-Elastic and Aero-Thermo-Elastic Theories for Hypersonic Applications: State-of-the-Art

The analysis of re-entry conditions for non-lifting capsules with deployable TPS includes ATE studies to predict the dynamic behavior of the flexible heat shield. The conditions that the capsule experiences during re-entry, in particular high dynamic pressure, high temperatures and high heat fluxes with consequent large deformation of the flexible structures implies that the aero-thermo-elasticity plays a central role in the analysis and optimization of hypersonic vehicles and components.

The combined extreme aerodynamic heating and loading, acting on the capsule, produces complex interactions between the flow, dynamics, and structure. In terms of testing capabilities, the hard task to test aero-elastically scaled models in wind tunnels, implies that AE simulations are critical for the hypersonic regime. Due to the complexity of the ATE problem, simple, but quite accurate, numerical tools that make use of linearized analytical solution, can reduce the cost of the test campaign and give valuable information in order to prepare high-fidelity numerical models. Since the study of the ATE behavior of membranes surrounded by hypersonic flow is a non-linear problem, it is needed to provide ourselves with numerical tools that take into account the structural non-linearity. Even though the ATE problem of a structure in hypersonic regime has been studied starting from the late 1950's [1], only recent studies have focused the attention on this FSI problem. For example, as shown in Figure 2.1, there has been a long period of inactivity on the study of the Inflatable Aerodynamic Decelerators (IADs) between the late 1970's and the early 2000's. Only recently, this type of configuration and the consequent study of the hypersonic ATE behavior of flexible structures and membranes have received a strong thrust.

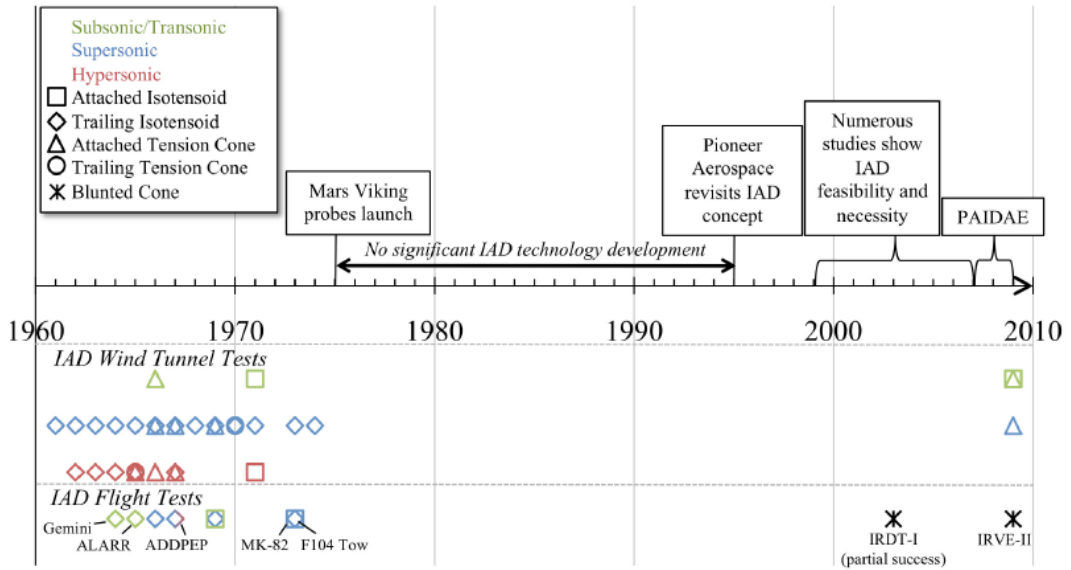


Figure 2.1 - History of IAD technology development efforts [24].

In the present section, a description of the state-of-art of the FSI problem for ATE applications is presented, with particular attention to the numerical and experimental ATE studies on flexible TPSs.

2.1. FSI approach for Aero-thermo-elastic applications

Mc Namara et al. [25] - [27] summarize all the most important aspects and recent developments of the modern hypersonic ATE problem.

There are two aspects to take into account to model an ATE system.

- To set the appropriate degree of complexity of each single discipline (fluid, thermal, and structural), before the coupling.
- To set the appropriate ATE coupling strategy.

As known, due to the simplicity of his formulation, the most widely used theory that approximate the unsteady aerodynamics is the piston theory (PT) [28], [29]. Even if several studies [25] have proven that the accuracy of the piston theory diminishes with increasing Mach number and surface inclination to the free stream, computational efficiency and ease of implementation make this method attractive for preliminary design of hypersonic

configurations. A good approximate criterion is that the product of Mach number and surface inclination is less than one [26]. However, due to the limitation of PT to conduct the aerodynamic calculation on a relatively simple geometry, and the increases in computational power, high-fidelity aerodynamic analysis using CFD has emerged as a viable approach for hypersonic ATE [30].

The same applies to the modeling of the structural dynamics which makes use of Rayleigh–Ritz and/or Galerkin methods [29] when the geometry is quite simple (i.e. plates, beams, etc). However, with the requirement to accurately model complex structural configurations, the FEM is the preferred approach for modeling hypersonic vehicle structural dynamic [31], [32].

Furthermore, since the ATE analysis using coupled CFD-FEM approaches presents a significant computational cost due to very large numbers of Degrees of Freedom (DOFs), and the need for a high number of repeated analyses due to uncertainties and design optimization [31], [32], a Reduced-Order Modeling (ROM) approach have been investigated. This approach seeks to provide an accurate description of a system at a computational cost that is a fraction of that needed for a CFD-FEM analysis. Typical approaches for constructing aerodynamic ROMs are proper orthogonal decomposition (POD) [33] - [35], Volterra series [34], and surrogates [36] - [38].

Since ROM methods are not part of the present work of thesis, they will not be investigated in detail.

Figure 2.1.1 [39] shows the fluid and structure solvers along with the methodologies for aero-elastic simulation for a closely coupled model.

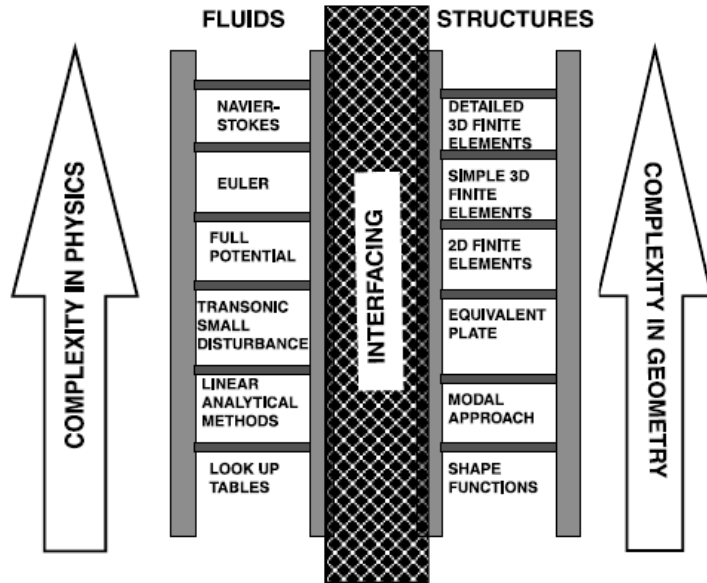


Figure 2.1.1 - Fluid and Structure solvers for aero-elastic simulation for a closely coupled model [39].

Furthermore, an extended review of the FSI approaches for AE applications has been investigated by Kamakoti and Shyy [40]. They have identified three types of FSI coupling:

- Fully Coupled: the governing fluid and structural equations are combined, solved and integrated in time simultaneously.
- Loosely Coupled: the structural and fluid equations are solved using two separate solvers. Only external interaction between the fluid and structure modules are performed. Therefore, the information is exchanged after partial or complete convergence of each module.
- Closely Coupled: the fluid and structure equations are solved separately using different solvers but are coupled into one single module with exchange of information at the interface using an interface module thereby making the entire model tightly coupled.

Currently the state-of-art of the Computational Aero Thermo Elasticity (CATE) study is the closely coupled model, which couples the fluid and structural solvers in a tight way, thereby making it an efficient method for complex nonlinear problems.

Typically, as shown in [27], the ATE problem is simplified by neglecting weak couplings, as well as the effect of aerodynamic pressure on aerodynamic heating. Figure 2.1.2 [27] shows the degree of coupling of the ATE problem.

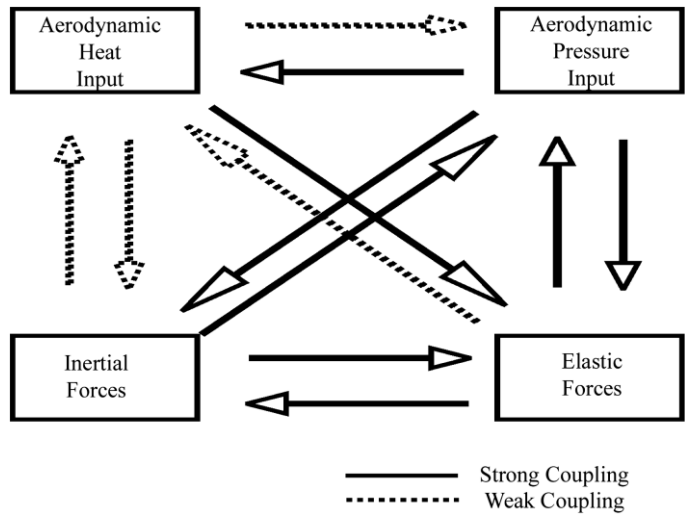


Figure 2.1.2 - Degree of coupling of the ATE problem [27].

In such an approach, the AT solution is obtained first, using a reference geometry of the structure. Subsequently, the AE analysis is carried out using an updated structure based on the resulting temperature distribution (see Figure 2.1.3). This simplification of the ATE problem is named “one-way coupling”, and relies on three important assumptions;

- 1) Thermodynamic coupling between heat generation and elastic deformation is negligible.
- 2) The characteristic time of the aero-thermal system is large relative to the time periods of the natural modes of the AE system, which means that the dynamic AE coupling is small.
- 3) Static AE coupling is insufficient to alter the temperature distribution from the reference condition.

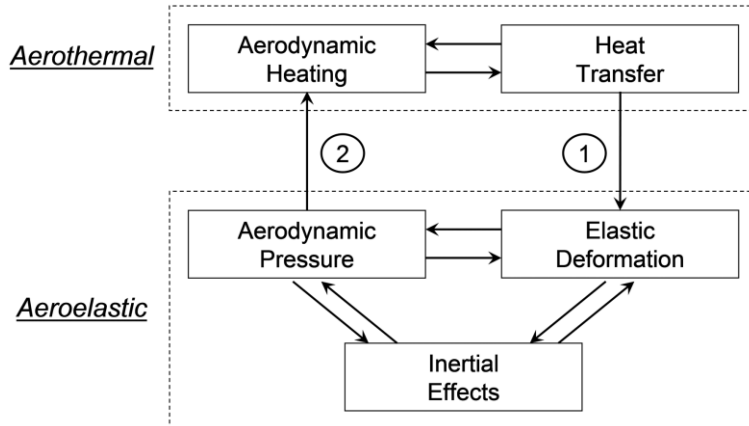


Figure 2.1.3 - Basic structure of the ATE problem [26].

Figure 2.1.4 [39] illustrates how a coupled fluid-structure aero-elastic analysis works. Fluid and structural solutions are independently computed, i.e. using Computational Fluid Dynamic (CFD) for the fluid analysis and the Finite Element Analysis (FEA) for the structural analysis, and the information is passed between them at the interfaces. At every time step the pressure data (C_p) from CFD are mapped onto structural grid points and the force vector $\{Z\}$ is computed. Then, the structural displacements are computed from CSD analysis and the deflections are mapped onto fluid grids that move accordingly.

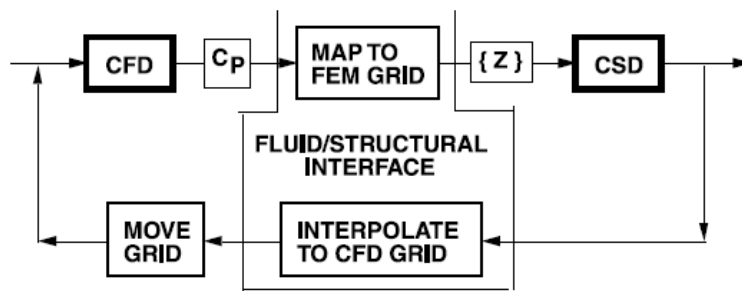


Figure 2.1.4 - Coupled fluid structural analysis [39].

In such a partitioned procedure for FSI or AE computations, the fluid and structure subsystems are time-integrated by different schemes that are tailored to their different mathematical models, and solved by a staggered numerical algorithm. A partitioned procedure for solving FSI problems is described below [41].

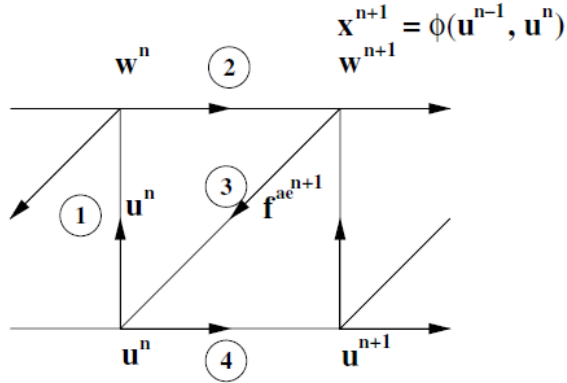


Figure 2.1.5 - Generic cycle of the conventional serial staggered procedure [41].

Following the procedure illustrated in Figure 2.1.5, at step (1) the motion of the boundary of the structure is transferred to the fluid subsystem and the position of the fluid dynamic mesh is consequently updated. Then, at step number (2) the fluid subsystem advance to the next time station and compute new pressure and fluid stress fields. At step (3) these fields are converted into a new load and transfer it to the structure, and finally at step number (4) the structure subsystem advance to the next time-station.

In an implicit time scheme, this transfer can occur more times per step, until convergence is reached.

In the present work, a partitioned Fluid Structure Interaction (FSI) approach based on the integration of different commercial software (*Cd-Adapco STAR-CCM+ v.10* [42] and *Abaqus/Standard v6.13* [43]) will be presented, and a simplified non-linear analytical tool capable to derive the equations of motion using a numerical code based on the natural modes of the structure will be provided.

2.2. Current ATE studies of flexible TPS

While there are many papers on the panel AE and ATE behavior [44], [46], there are but a handful of papers that specifically address membrane flutter. Even though the term membrane is reserved for zero bending rigidity structures, almost all of these studies consider the membrane flutter problem to be a limiting case of a plate as bending rigidity approaches zero or in-plane tension approaches infinity [29], [47] - [49]. The first attempt to

develop an analysis using the membrane equation of a two-dimensional membrane with a constant tension force and supersonic static aerodynamic approximation has been carried out by Ellen [50].

Due to the challenging hypersonic flow regime and the complexity of coupling fluid and structural solvers in an accurate and computationally efficient manner, high-fidelity computational modeling of flexible inflatable TPS has been limited [51], [52]. Kramer et al. [53] have developed a series of FSI simulations of an aerodynamic tension-cone decelerator prototype using a loosely coupled approach between a large deformation analysis of thin-shells formulation for the structural domain, and a large-eddy simulation of compressible turbulent flows formulation for the fluid domain.

Rohrschneider, in his PhD thesis [54], has developed an aerodynamic tool that implements an engineering estimate of hypersonic aerodynamics with a moving boundary condition to determine the flutter point of a thin-film ballute on a Titan aero-capture trajectory.

Furthermore, Wang et al. [55] have performed a non-linear AE analysis for a modeled ballute system with wrinkling phenomena considered, coupling the explicit nonlinear finite element code DYNA3D, with a modified Newtonian flow theory, in order to provide hypersonic aerodynamic loading, using a higher fidelity CFD approach, gas kinetic Bhatnagar-Gross-Krook-Xu (BGKX) method.

Although the accuracy of such a methods is quite high since they used a tight coupling between high-fidelity solvers, the computational cost of those methods could remain an obstacle in the preliminary design phase of a HIAD/HDAD concept.

In order to overtake the computational cost problem related to the FSI coupling, Goldman and Dowell have studied the possibility of coupling a simplified nonlinear structural theory based on a hybrid Ryleigh-Ritz-Galerkin method [29] with the first order PT [56] and a supersonic potential flow aerodynamic theory [57], [58]. This model makes possible to give a preliminary solution of the AE response of a conical shell, resting on several circumferential elastic supports. Basis of the aforementioned work is the study of a square TPS coupon which experiences trailing edge oscillatory behavior during experimental testing in the 8' High Temperature Tunnel (HTT) [59]. In this work, the authors performed experimental Ground Vibration Tests (GVTs) (see Figure 2.2.1) and wind tunnel

tests in the 8' HTT (see Figure 2.2.2), and developed a set of theoretical techniques to characterize the aero-elasticity of the thermal protection system (TPS) on the NASA Hypersonic Inflatable Aerodynamic Decelerator (HIAD).

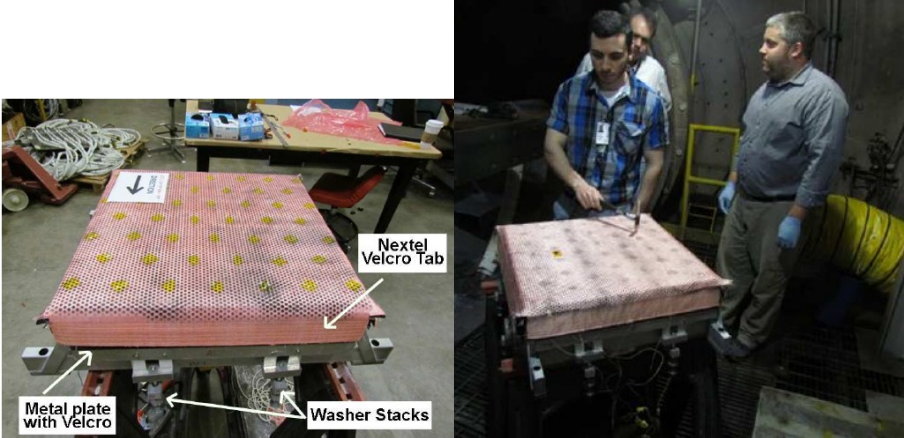


Figure 2.2.1 - TPS coupon tensioned over the mounting frame (left), and during GVTs (right)[59].

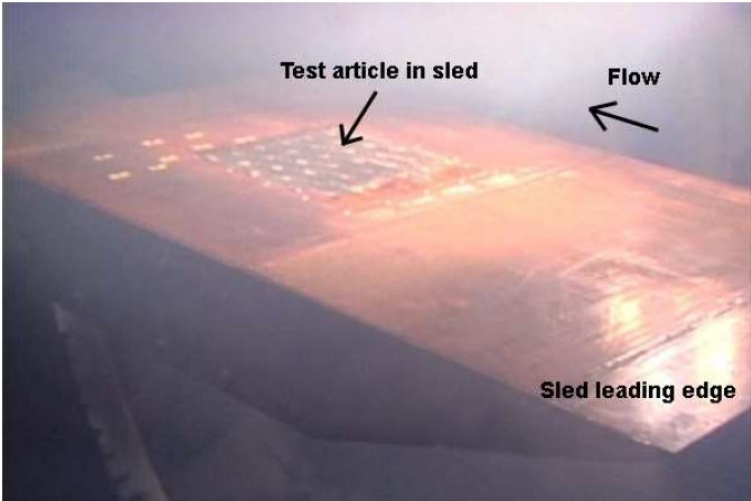


Figure 2.2.2 - TPS coupon mounted in the 8' HTT sled [59].

These studies represent the basis for the development and the experimental validation of the non-linear analytical tool presented in this thesis work.

Before the aforementioned study, a few works have been conducted on a scaled model of a tension-cone in a supersonic wind tunnel under a range of flow conditions. One of the first experimental work has been carried out in 2006 by Buck [61], where he describes

several tests conducted to develop the capability for testing lightweight, flexible materials in hypersonic facilities (see Figure 2.2.3). Clark et al. [62] have investigated the supersonic aerodynamic and aero-elastic characteristics of a tension cone inflatable aerodynamic decelerator in the Langley Aero-thermo-dynamics Laboratory 20-Inch Hypersonic CF₄ and 31-Inch Mach 10 Air blow-down wind tunnels (see Figure 2.2.4).

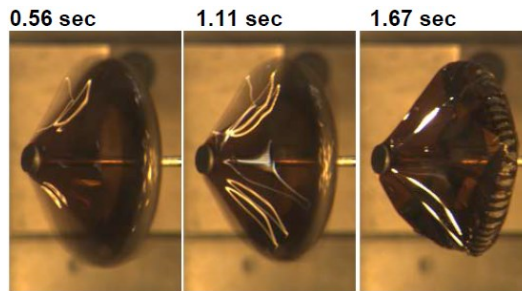


Figure 2.2.3 - Different stages in testing of a 70° half angle afterbody attached ballute [61].

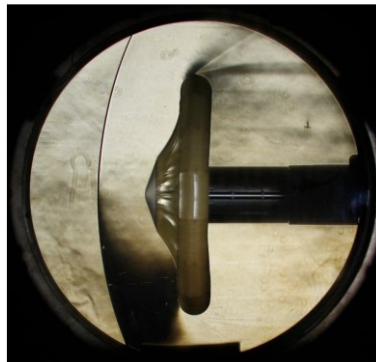


Figure 2.2.4 - Schlieren image for Glenn Research Center Supersonic Wind Tunnel inflatable model [62].

At today, the most advanced HIAD program, which has been tested for a suborbital entry mission, is the IRVE program, which has been successfully launched in two occasions, in 2009 with the IRVE-2 mission [63] and in 2012 with the IRVE-3 mission [64] respectively (see Figure 2.2.5).

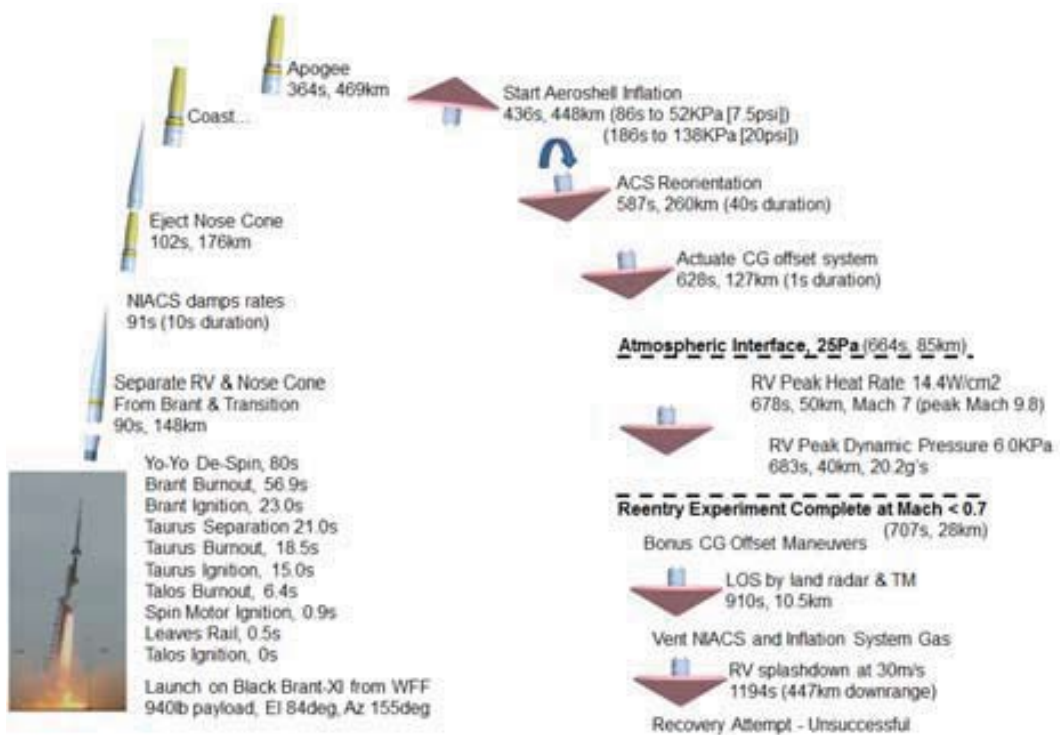


Figure 2.2.5 - IRVE-3 Mission Events [64].

Furthermore, the most advanced testing campaign with the purpose to study the thermal response of material layups supporting an inflatable aero shell, in order to identify expected material response and failure times, was conducted at NASA Langley Research Center [65], [66] in the frame of the PAIDAE program [67]. Material layups were tested in the 8'HTT (see Figure 2.2.6), where they were subjected to hypersonic aero-thermal heating conditions, similar to those expected for a Mars entry.

At the moment, the most advanced testing campaign on a HDAD configuration has been developed in the framework of the IRENE project. In order to investigate the thermal response of a deployable TPS, a scaled model of the IRENE capsule has been successfully tested in the Plasma Wind Tunnel "SCIROCCO" facility available at CIRA (Centro Italiano Ricerche Aerospaziali of Capua), where the nominal values of the heat flux conditions during a suborbital re-entry have been reproduced (see Figure 2.2.7) [22].

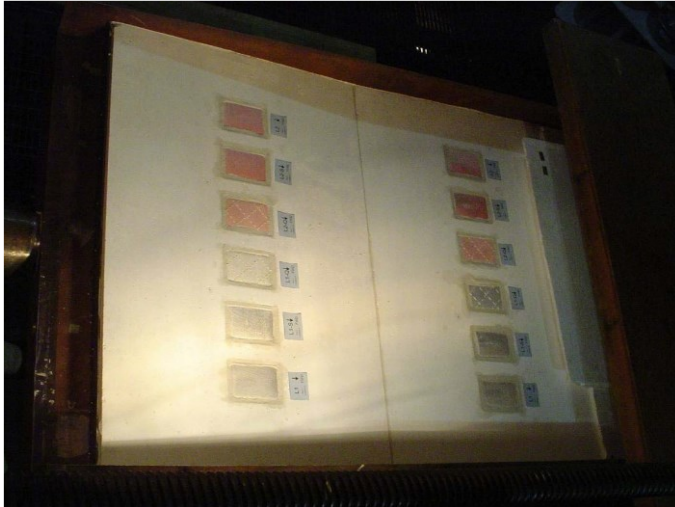


Figure 2.2.6 - Sled loaded with samples [68].



Figure 2.2.7 - Test article at the end of the PWT test [22].

The aforementioned experimental studies carried out at NASA LaRC represent the basis for the aero-thermal a preliminary validation of FSI modeling for a hypersonic deployable re-entry system introduced in the present work of thesis.

3. Numerical Models

In the present Section, a description of the numerical models used in this PhD thesis are discussed.

First, the system of dynamic equations of motion for a point mass characterized by three degrees of freedom is presented. This numerical tool makes possible the preliminary evaluation of the main aerodynamic and aero-thermodynamic loads on a body in hypersonic flow regime.

Then, a brief description of the theories at the basis of the hypersonic CFD and the non-linear FE commercial codes *Cd-Adapco STAR CCM+ v 10* [42] and *Abaqus/Standard v 6.13* [43] are described.

Finally, a non-linear aero-elastic analytical model based on the extraction of the natural modes of the structure of a multi-layer flexible plate is developed.

3.1 Dynamic models

One of the first step to preliminarily compute the entry trajectory of a capsule is to solve the dynamic equations of motion for a point mass characterized by three degrees of freedom. Even though the three-dimensionality of the capsule should be considered, and therefore the momentum, taking into account the position of the Center of Gravity (CoG), in order to evaluate a preliminary entry trajectory, this aspect of the dynamic can be neglected, considering the body as a point mass. A sketch of the loads acting on a capsule during the atmospheric entry trajectory has been depicted in Figure 3.1.1. Where M is the capsule mass, W is the capsule weight force, t is the time, V is the entry velocity, r is the radius of curvature of the trajectory, γ is the flight path angle, and L and D are the lift and drag respectively.

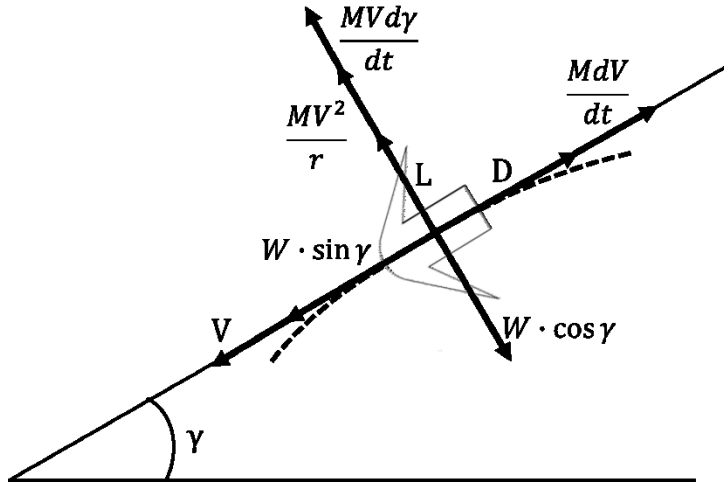


Figure 3.1.1 – Sketch of the acting loads on a re-entry capsule.

Taking into account the loads acting on a capsule during the atmospheric entry, and considering angular velocity and the model of the planet atmosphere, the set of first order non-linear ordinary differential equations shown in Equation (3.1.1) has been written and solved by numerical integration at discrete time-steps and taking advantage of the Euler's method [7].

$$\left\{ \begin{array}{l} \frac{dV}{dt} = -\frac{\rho V^2}{2\beta} - g \sin \gamma + \omega_m^2 r \cos \lambda (\sin \gamma \cos \lambda - \cos \gamma \sin \psi \sin \lambda) \\ V \frac{d\gamma}{dt} = \left(\frac{V^2}{r} - g \right) \cos \gamma + 2\omega_m \cos \lambda \cos \psi + \omega_m^2 \cos \lambda (\cos \gamma \cos \lambda - \sin \gamma \sin \psi \sin \lambda) \\ V \frac{d\psi}{dt} = -\frac{V^2}{r} \cos \gamma \cos \psi \tan \lambda - 2\omega_m (\sin \lambda - \tan \gamma \sin \psi \cos \lambda) - \omega_m^2 r \frac{\cos \psi \sin \lambda \cos \lambda}{\cos \gamma} \\ \frac{dH}{dt} = V \sin \gamma \\ \frac{d\lambda}{dt} = \frac{V}{r} \cos \gamma \sin \psi \\ \frac{d\Lambda}{dt} = \frac{V}{r} \cdot \frac{\cos \gamma \cos \psi}{\cos \lambda} \end{array} \right. \quad (3.1.1)$$

Where, H is the altitude, β the ballistic coefficient, g the gravity acceleration, r the radius of curvature of the trajectory, ψ the azimuth angle, λ the latitude, Λ the longitude and ω_m the Mars angular velocity.

Starting from the trajectory and the velocity profile computed by solving the Equation (3.1.1), some important parameters can be estimated, such as the stagnation point heat flux and the stagnation point pressure.

Sutton and Tauber [69] have proposed an engineering formula for the evaluation of the stagnation-point heat flux.

$$\dot{q}_0 = k \sqrt{\frac{\rho}{R_c}} V^3 \quad \begin{array}{l} k = 1.7415e^{-4} \text{ (Earth)} \\ k = 1.9027e^{-4} \text{ (Mars)} \end{array} \quad (3.1.2)$$

Where ρ is the atmospheric density and R_c is the nose curvature radius.

Finally, according to Newton's theory in hypersonic flow [70] the stagnation point pressure assume the formulation presented below.

$$p_0 = \rho V^2 \quad (3.1.3)$$

3.2 Hypersonic CFD model

The fluid dynamic governing equations can be written in a generic vector form as shown in Equation (3.2.1) [7].

$$\frac{\partial \underline{u}}{\partial t} + \nabla \cdot (\underline{\mathcal{F}} - \underline{\mathcal{G}}) = \underline{\mathcal{S}} \quad (3.2.1)$$

In the aforementioned formulation \underline{u} is the vector of conserved quantities.

$$\underline{u} = \begin{bmatrix} \rho_1 \\ \rho_2 \\ \vdots \\ \rho_i \\ \rho \underline{V} \\ \rho \mathcal{E} \end{bmatrix} \quad (3.2.2)$$

Where ρ is the atmospheric density, \underline{V} is the mass velocity of the fluid and \mathcal{E} is the total energy.

$\underline{\mathcal{F}}$ is the non-dissipative part of the flux vector.

$$\underline{\mathcal{F}} = \begin{bmatrix} \rho_1 \underline{V} \\ \rho_2 \underline{V} \\ \vdots \\ \rho_i \underline{V} \\ \rho \underline{V} \underline{V} + \rho \underline{\mathcal{U}} \\ \rho \underline{\mathcal{E}} \underline{V} + \rho \underline{V} \end{bmatrix} \quad (3.2.3)$$

Where $\underline{\mathcal{U}}$ denotes the singular tensor. $\underline{\mathcal{G}}$ represent the dissipative part of the flux vector.

$$\underline{\mathcal{G}} = \begin{bmatrix} J_1 \\ J_2 \\ \vdots \\ J_i \\ \underline{\tau}_d \\ \lambda \nabla T + \underline{\tau}_d \cdot \underline{V} - \sum_i h_i J_i \end{bmatrix} \quad (3.2.4)$$

Where J_i is the mass diffusivity of the i^{th} species, τ_d is the dissipative part of the stress vector and h_i is the sensible enthalpy per unit mass of the i^{th} species.

Finally, $\underline{\mathcal{S}}$ is the product vector.

$$\underline{\mathcal{S}} = \begin{bmatrix} \omega_1 \\ \omega_2 \\ \vdots \\ \omega_i \\ 0 \\ 0 \end{bmatrix} \quad (3.2.5)$$

Where ω_i represent the mass production of the i^{th} species.

The solution of this system of equations for the hypersonic flow field in continuum regime has been solved by means of the commercial CFD software *Cd-Adapco STAR-CCM+* v. 10 [42].

In the present work, the numerical simulations have been performed with a density-based, time implicit, and numerical resolution scheme through a control volume based technique. The AUSM (Advanced Upstream Splitting Method) scheme has been employed for convective numerical fluxes. This procedure has been successfully used for similar problems in previous works by Savino et al [7], [71].

The density-based approach consists in the simultaneous solution of the continuity, momentum and energy equations, while the pressure field is determined from the equation of state. Since the governing equations are coupled, a number of iterations of the solution loop must be performed before a converged solution is obtained. The non-linear governing equations are linearized to produce a system of equations for the dependent variables in every computational cell. The resultant linear system is then solved to furnish an updated flow field solution at each iteration. The governing equations have been linearized by means of an implicit formulation. An implicit scheme foresees that, for a given variable, the unknown value in each cell is computed by means of a relation including both existing and unknown values from neighboring cells. Each unknown will therefore appear in more than one equation in the system and these equations must be solved simultaneously to give the unknown quantities.

During hypersonic flights, due to the high total enthalpy and to the presence of strong shock waves, the huge energy conversion in sensible enthalpy can cause dissociation and ionization phenomena. However, since in this work suborbital trajectories, or atmosphere made predominantly by a single component (such as Mars atmosphere, which is 95%, made of carbon dioxide) are considered, the atmosphere has always been assumed as an ideal gas, considering that the total flow enthalpy is not able to trigger significant dissociation phenomena.

In addition, a laminar viscous model has been assumed. Despite the high velocities that a capsule encounters during the atmospheric entry, because of the extremely low fluid density in the higher layers of the atmosphere, and the relatively small dimensions of the capsule, the Reynolds number is low enough in order to use the laminar model in the preliminary study. Furthermore, the transport properties (i.e. the dynamic viscosity, the thermal conductivity and the mass diffusivity) have been evaluated according to the kinetic theory of gases [72].

Two-dimensional and Three-dimensional simulations have been carried out. Different conditions were set for the computational domain boundaries.

A pressure far-field condition was set for the boundary inlet, in order to model free stream conditions. An axis-symmetry condition for the symmetry surface in the two-dimensional simulation, and periodic conditions on the lateral surfaces of the three-

dimensional model have been set. Furthermore, a no-slip condition for the surface of the capsule and a pressure outlet for the downstream surface have been set.

For the three-dimensional simulation, a radiation model, using surface-to-surface radiation approach implemented in *Cd-Adapco STAR-CCM+ v. 10*, has been used, in order to predict the radiative equilibrium temperature of the capsule surface at maximum stagnation pressure condition.

3.3 Non-linear FE model

In order to evaluate the dynamic behavior of a plate, a FEA using the commercial code *Abaqus/Standard v 6.13* has been carried out [43]. As known, in the non-linear dynamic, the strains depend nonlinearly on displacements, and the $[\bar{B}]$ matrix, which relates displacement and strains is non-linear.

$$d\vec{\varepsilon} = [\bar{B}]d\vec{a} \quad (3.3.1)$$

It is known that

$$[\bar{B}] = [\bar{B}_0] + [\bar{B}_L(\vec{a})] \quad (3.3.2)$$

where $[\bar{B}_0]$ is the small strain matrix (linear) and $[\bar{B}_L]$ depends on displacements (\vec{a}). Finally, the stiffness matrix $[\bar{K}]$ is equal to

$$[\bar{K}] = \int_V [\bar{B}]^T [D] [\bar{B}] dV = [K_0] + [K_L] \quad (3.3.3)$$

In which $[D]$ is the usual set of elastic constants, while $[K_0]$ and $[K_L]$ are the linear stiffness matrix (due to the small displacements) and the large displacement matrix respectively.

In *Abaqus/Standard v 6.13*, it is possible to activate and deactivate the calculation of the large displacement stiffness matrix by means of the keyword NLGEOM at the beginning of the dynamic step.

General non-linear dynamic analysis in *Abaqus/Standard v 6.13* uses implicit time integration to calculate the dynamic response of a system. For the present work, general-purpose conventional shell S4R with reduced integration elements have been used. These elements allow transverse shear deformation. They use thick shell theory as the shell

thickness increases and become discrete Kirchhoff thin shell elements as the thickness decreases. Furthermore, 4-node quadrilateral membrane elements (M3D4R) with reduced order and hourglass control have been used. Those elements are sheets in space that can carry membrane force but do not have any bending or transverse shear stiffness, so the only nonzero stress components in the membrane are those components parallel to the middle surface of the membrane: the membrane is in a state of plane stress.

Abaqus/Standard v 6.13 uses the Hilber-Hughes-Taylor time integration scheme for dynamic solutions (see Equation (3.3.4)):

$$M^N \ddot{u}^N|_{t+\Delta t} + (1 + \alpha)(I^N|_{t+\Delta t} - P^N|_{t+\Delta t}) - \alpha(I^N|_t - P^N|_t) + L^N|_{t+\Delta t} = 0 \quad (3.3.4)$$

where M^N is the consistent mass matrix, I^N is the internal force vector, P^N is the external force vector. In this context, the terms “matrix” and “vector” refer to matrices and vectors in the space of the nodal variables u^N , and the superscript N indicate the N -th degree of freedom.

Furthermore, L^N is the sum of all Lagrange multiplier forces associated with degree of freedom N . The operator definition is completed by the Newmark formulae for displacement and velocity integration

$$u|_{t+\Delta t} = u|_t + \Delta t \dot{u}|_t + \Delta t^2 \left(\left(\frac{1}{2} - \beta \right) \ddot{u}|_t + \beta \ddot{u}|_{t+\Delta t} \right) \quad (3.3.5)$$

$$\dot{u}|_{t+\Delta t} = \dot{u}|_t + \Delta t \left((1 - \gamma) \ddot{u}|_t + \gamma \ddot{u}|_{t+\Delta t} \right)$$

The numerical parameters α , β and γ associated with the Hilber-Hughes-Taylor operator are tuned differently for moderate dissipation and transient fidelity applications. Furthermore, they stabilize the algorithm. They assume the formulation shown in Equation (3.3.6).

$$\beta = 1/4 (1 - \alpha)^2; \quad \gamma = 1/2 - \alpha \quad \text{and} \quad -\frac{1}{3} \leq \alpha \leq 0 \quad (3.3.6)$$

These time integration operators are implicit, which means that the operator matrix must be inverted and a set of simultaneous non-linear dynamic equilibrium equations must be solved at each time increment. This solution is done iteratively using Newton's method.

Marching through a simulation with a finite time increment size generally introduces some degree of numerical damping.

The relation presented in Equation (3.3.7) provides control of the numerical damping associated with the time integrator while preserving desirable characteristics of the integrator. The numerical damping grows with the ratio of the time increment to the period of vibration of a mode. The case of $\alpha=0$, results in no damping and is exactly the trapezoidal rule.

For the present work, linear and non-linear dynamic simulations have been carried out, in order to assess the vibrational behavior of the plate. Furthermore, SPRINGA elements implemented in *Abaqus/Standard v 6.13* have been used in the present work in order to simulate the stiffness of the stitching between the layers. A SPRINGA element acts between two nodes, with its line of action being the line joining the two nodes, so that this line of action can rotate in large-displacement analysis.

Finally, the critical damping ζ_i for the given mode i , in direct-integration dynamic analysis formulation, can be formulated in terms of the Rayleigh damping expression.

$$\zeta_i = \frac{\alpha_R}{2\omega_i} + \frac{\beta_R\omega_i}{2} \quad (3.3.7)$$

Where ω_i is the natural frequency, and α_R and β_R are the damping factors. The α_R factor introduces damping forces caused by the absolute velocities of the model. This damping factor defines mass proportional damping.

The β_R factor introduces damping proportional to the strain rate $\dot{\epsilon}$, which can be thought of as damping associated with the material itself. β_R defines damping proportional to the elastic material stiffness D^{el} . β_R is interpreted as defining viscous material damping in *Abaqus/Standard v 6.13*, which creates an additional "damping stress" σ_d proportional to the total strain rate $\dot{\epsilon}$ (see Equation (3.3.8)).

$$\sigma_d = \beta_R D^{el} \dot{\epsilon} \quad (3.3.8)$$

Where D^{el} is the material's current elastic stiffness.

3.4 Non-linear theoretical model based on the natural modes of the structure

In order to evaluate the non-linear dynamic behavior of a multi-layered plate, the von Kármán's three dimensional large deflection theory [29] and a hybrid Raleigh-Ritz-Galerkin approach [60] have been used to derive the equations of motion. Using this approach, the Lagrangian of the problem has to be described.

$$L = T - U \quad (3.4.1)$$

Where T is the kinetic energy

$$T = \int_0^a \int_0^b \frac{m}{2} \left(\frac{\partial w}{\partial t} \right)^2 dx dy \quad (3.4.2)$$

and U is the elastic potential energy

$$U = U_B + U_S + U^{St} \quad (3.4.3)$$

U_B and U_S represent the bending and stretching energies given by von Kármán's large deflection theory for a single plate layer respectively (see Equation (3.4.4)). The principal source of structural non-linearity is the tension that results from the in-plane stretching energy U_S that is a consequence of the large out-of-plane bending.

$$U_B = \frac{D}{2} \int_0^b \int_0^a \left\{ \left(\frac{\partial^2 w}{\partial x^2} \right)^2 + \left(\frac{\partial^2 w}{\partial y^2} \right)^2 + 2\nu \frac{\partial^2 w}{\partial x^2} \frac{\partial^2 w}{\partial y^2} + 2(1-\nu) \left(\frac{\partial^2 w}{\partial x \partial y} \right)^2 \right\} dx dy + \frac{N_x^A}{2} \int_0^b \int_0^a \left(\frac{\partial w}{\partial x} \right)^2 dx dy + \frac{N_y^A}{2} \int_0^b \int_0^a \left(\frac{\partial w}{\partial y} \right)^2 dx dy \quad (3.4.4)$$

$$U_S = \frac{1}{2Eh} \int_0^b \int_0^a \left\{ \left(\frac{\partial^2 F}{\partial x^2} \right)^2 + \left(\frac{\partial^2 F}{\partial y^2} \right)^2 + 2\nu \frac{\partial^2 F}{\partial x^2} \frac{\partial^2 F}{\partial y^2} + 2(1-\nu) \left(\frac{\partial^2 F}{\partial x \partial y} \right)^2 \right\} dx dy$$

Where F is the Airy stress function for a given layer. An expression of the Airy stress function is given below.

$$\left(\frac{\partial^2 F}{\partial x^2}\right) = N_y ; \left(\frac{\partial^2 F}{\partial y^2}\right) = N_x ; \left(\frac{\partial^2 F}{\partial x \partial y}\right) = N_{xy} \quad (3.4.5)$$

For point-wise tack locations, the stitching energy (U^{St}) may be written as shown in Equation (3.4.6). In this formulation, the stitches constraining the layers are simple linear springs with k^{St} equal to the spring constant of the stitch. The stitching energy may take different forms depending on the desired pattern. Equation (3.4.6) shows the formulation assumed by the stitching energy where the first term represents the point-wise stitching between the first (L1) and the second (L2) layer, and the second term represents the point-wise stitching between the second (L2) and the third (L3) layer. The summation indices indicate the number of stitches.

$$U^{St} = \frac{k^{St}}{2} \sum_i (w^{L1} - w^{L2})^2|_{x_i, y_i} + \frac{k^{St}}{2} \sum_i (w^{L2} - w^{L3})^2|_{x_i, y_i} \quad (3.4.6)$$

In order to assess the aero-elastic behavior of the TPS the first order Piston Theory (PT) [29] will be used. An expression of the aerodynamic virtual work is given by Equation (3.4.7).

$$\delta W_{aero} = - \int_0^b \int_0^a (\Delta p \delta w) dx dy \quad (3.4.7)$$

Where the aerodynamic pressure (Δp) is given by first-order PT

$$\Delta p = \frac{2q}{Mach} \left[\frac{\partial w}{\partial x} + \frac{1}{V_\infty} \frac{\partial w}{\partial t} \right] \quad (3.4.8)$$

where q is the dynamic pressure.

Furthermore, in order to satisfy simply supported deflection boundary conditions as well as a condition of vanishing axial stress the deflection and Airy stress function are expanded in modal form using the mode-shape function $\phi_{nm}(x, y)$:

$$\phi_{nm}(x, y) = \sin\left(\frac{n\pi x}{a}\right) \sin\left(\frac{m\pi y}{b}\right) \quad (3.4.9)$$

$$w = \sum_n \sum_m q_{nm}(t) \phi_{nm}(x, y); \quad F = \sum_n \sum_m f_{nm}(t) \phi_{nm}(x, y) \quad (3.4.10)$$

The stress function expansion is an approximate particular solution to the following strain compatibility condition [29].

$$\frac{\nabla^4 F}{Eh} = \left(\frac{\partial^2 w}{\partial x \partial y} \right) - \frac{\partial^2 w}{\partial x^2} \frac{\partial^2 w}{\partial y^2} \quad (3.4.11)$$

A Galerkin approach is used to solve Equation (3.4.11) for the stress function modal coordinate f_{nm} , in terms of the deflection coordinate q_{nm} .

The Lagrangian is then written in terms of deflection coordinates only, and the Lagrange equation of the following form is applied:

$$\frac{d}{dt} \left(\frac{\partial L}{\partial \dot{q}_{nm}} \right) - \frac{\partial L}{\partial q_{nm}} + Q_{nm} \quad (3.4.12)$$

where Q_{nm} is the generalized force.

Substituting w ($q_{nm}(t), \phi_{nm}(x, y)$) into the energy equations and rewriting the Lagrange equation in a matrix form, the system of non-linear integro-differential equations has been obtained, which for a three-layer case assume the formulation that follows (see Equation (3.4.13)):

$$\begin{aligned} M^{L1} \ddot{\vec{a}} + Z^{L1} \dot{\vec{a}} + D^{L1} \vec{a} + [B^{L1} + A^{L1}] \vec{a} + I^{L1} \{\vec{a} - \vec{b}\} + S^{L1} &= 0 \\ M^{L2} \ddot{\vec{b}} + D^{L2} \dot{\vec{b}} + B^{L2} \vec{b} + I^{L2} \{\vec{b} - \vec{c}\} + I^{L2} \{\vec{b} - \vec{a}\} + S^{L2} &= 0 \\ M^{L3} \ddot{\vec{c}} + D^{L3} \dot{\vec{c}} + B^{L3} \vec{c} + I^{L3} \{\vec{c} - \vec{b}\} + S^{L3} &= 0 \end{aligned} \quad (3.4.13)$$

Where \vec{a} , \vec{b} and \vec{c} are the modal coordinate vectors of the three layers. M^L, B^L, D^L, I^L and S^L are the diagonal mass matrix, the diagonal bending stiffness matrix, the diagonal damping matrix, the spring stitching matrix and the stretching energy vector respectively. Therefore, since the principal source of structural non-linearity is the tension that results from the in-plane stretching, the non-linearity of the system lies in the stretching energy vector S^L . Furthermore, Z^L and A^L are the aerodynamic damping and the aerodynamic stiffness matrix respectively. The aerodynamic pressure is applied only to the outermost layer (L1), since it is the only layer exposed directly to flow.

An extended formulation of the aforementioned matrices has been reported in the Appendix I.

Furthermore, in addition to the aero-elastic analysis, in order to evaluate the plate response to an impulse force, the aerodynamic stiffness and damping terms for the outermost Nextel layer are removed and replaced with the external force vector F^e (see Equation (3.4.14)).

$$F^e = F_{app} \delta(t - t_0) \phi(x, y) \Big|_{x_0, y_0} \quad (3.4.14)$$

Finally, in order to assess the aero-elastic behavior of the plate the equation set (3.4.13) are solved using the 4th order Runge-Kutta integration scheme in MATLAB.

4. Aerodynamic (AD) and Thermal (T) Analysis of a Deployable Capsule

In order to present a computational methodology to preliminary evaluate the main aerodynamic and thermal loads of a deployable capsule in hypersonic flow regime, this Section is focused on the description of the EDL phase (Section 4.1), and the preliminary Aerothermodynamic assessment (Section 4.2) of the lander of the Small Mars Satellite mission. It has to be noted that only the dynamic equations of motion for a point mass characterized by three degrees of freedom have been considered.

As outlined in Figure 4.1, three phases have been identified during the Mars entry trajectory, after the separation from the propulsion module.

- *First phase*: above the Mars entry atmosphere, the “umbrella-like” flexible heat shield is deployed.
- *Second phase*: the capsule is decelerated; the heat flux and pressure reach a maximum and then are reduced. Once the capsule is in subsonic regime, a parachute is deployed and the separation of the TPS occurs.
- *Third phase*: when the capsule velocity is relatively small (less than 25 (m/s)) the touch down occurs and an airbag can be inflated.

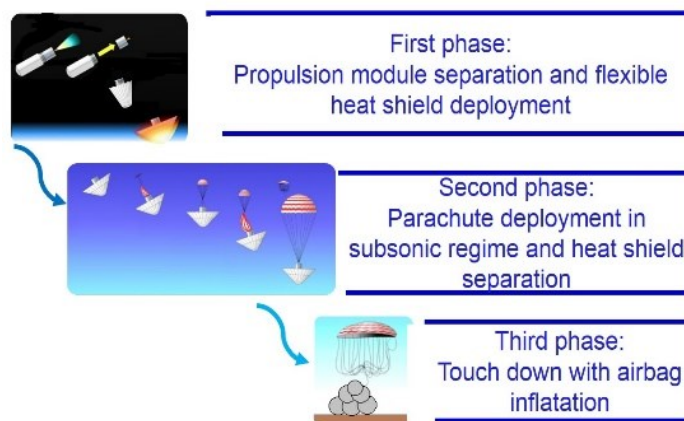


Figure 4.1 - EDL operation sequence.

4.1 Preliminary aerodynamic and thermal analysis

In order to compute the entry trajectories, the set of first order non-linear ordinary differential equations (3.1.1) presented in Section 3.1 has been solved. For entry trajectories air density, pressure and temperature have been assumed to vary according to the COSPAR Mars Reference Atmosphere Model [73] (see Table 4.1.1).

<i>Height (Km)</i>	<i>Temperature (K)</i>	<i>Density (Kg/m³)</i>
0	214.0	1.55E-02
10	205.0	6.470E-03
20	188.3	2.630E-03
30	175.0	9.800E-04
40	162.4	3.400E-04
50	152.2	1.080E-04
60	144.2	3.180E-05
70	139.5	8.730E-06
80	139.0	2.290E-06
90	139.0	6.010E-07
100	139.0	1.590E-07
110	149.4	4.140E-08
120	159.7	1.190E-08
130	170.0	3.760E-09
140	245.1	1.090E-09
150	288.6	4.730E-10

Table 4.1.1 - COSPAR Mars Reference Atmosphere Model

First of all, a parametric analysis of the Velocity, the Mach number, the deceleration, the stagnation point pressure and stagnation point heat flux profiles at Mars atmospheric entry, as a function of ballistic coefficient (β) and Flight Path Angle (FPA) has been carried out.

For the SMS configuration, a drag coefficient (C_d) of 1 has been considered, due to the half-cone angle of 45° [7].

The initial conditions, in terms of relative initial velocity, FPA, ballistic coefficient and entry altitude relative to the equatorial Mars radius have been selected. Since the initial mass of 150 (Kg) and the diameter of 3(m), give a ballistic parameter of 21 (Kg/m²), a range of ballistic parameter between 10 and 30 (Kg/m²) has been selected. A value of 5.5 (Km/s) and 125 (Km) for the relative initial entry velocity and the initial entry altitude respectively, and a range of FPA between -12° and -14° have been chosen. Particular emphasis was placed on the results at ballistic parameter of 21 (Kg/m²) and FPA of -13° .

Figure 4.1.1 shows the maximum stagnation point pressure, while the maximum stagnation point heat flux is shown in Figure 4.1.2, thus, the maximum radiative equilibrium temperature and the landing velocity as a function of the ballistic coefficient (β) and the FPA (γ) have been shown in Figure 4.1.3 and Figure 4.1.4 respectively.

These results show that the variation of the maximum stagnation point heat flux, the maximum stagnation point pressure and the maximum radiative equilibrium temperature are affected by the variation of both, the ballistic coefficient and FPA.

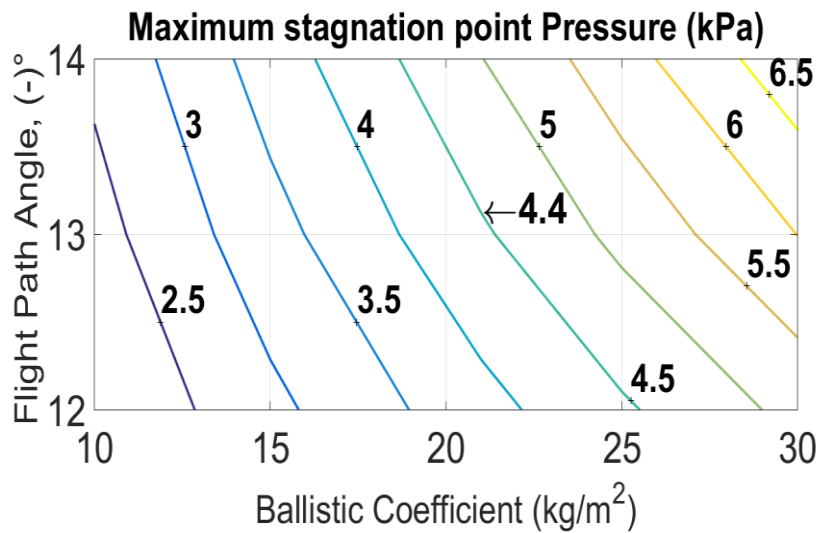


Figure 4.1.1 - Maximum stagnation point pressure

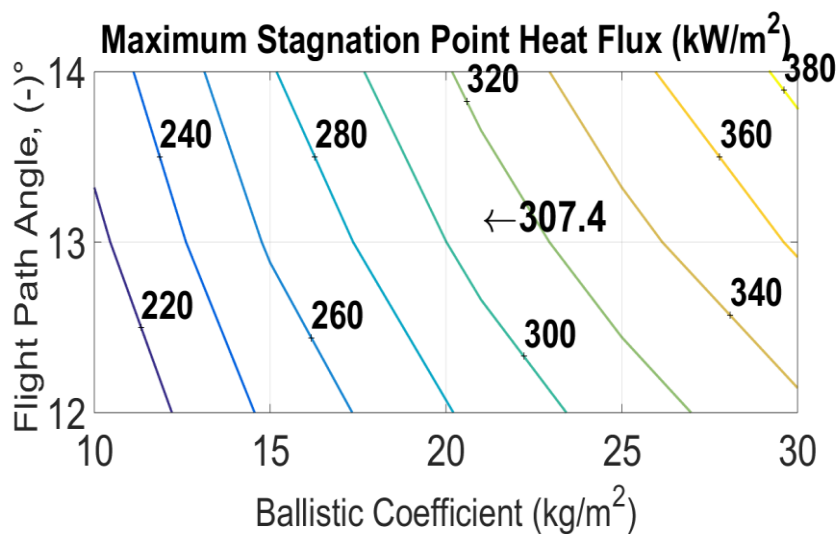


Figure 4.1.2 - Maximum stagnation point heat flux

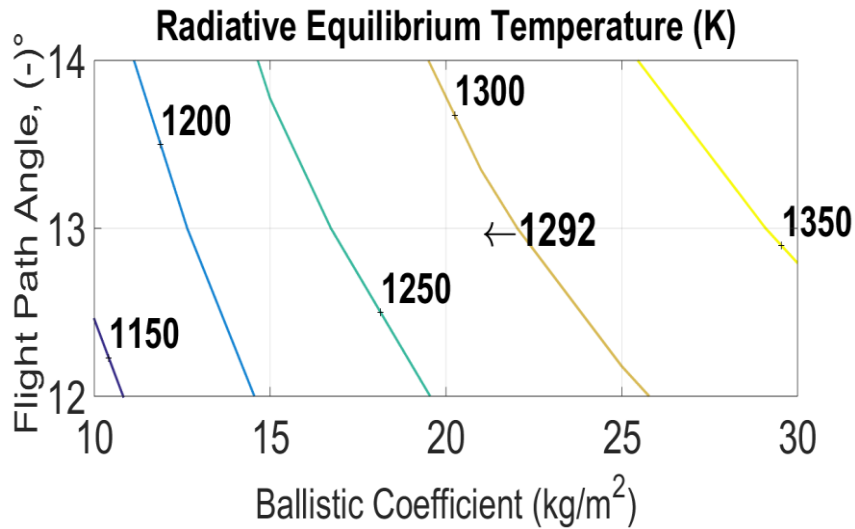


Figure 4.1.3 - Maximum stagnation point radiative equilibrium temperature

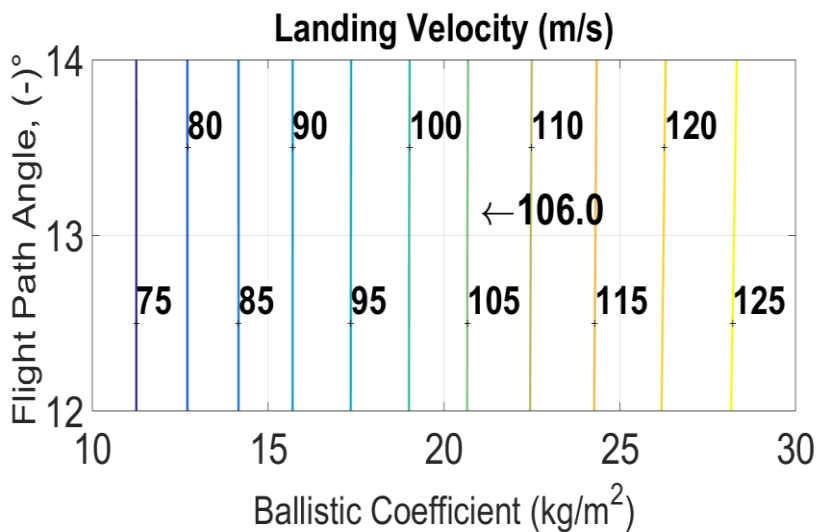


Figure 4.1.4 - Landing velocity

Furthermore, as expected, the landing velocity does not change with the initial entry FPA, but is strongly affected by the value of the capsule ballistic coefficient. As shown in Figure 4.1.4, the terminal velocity of a Mars entry system is generally larger than a few hundred m/s, even though the ballistic coefficient is lower than 30.

Furthermore, in order to show the entry trajectory main parameters for the nominal case, the simulation with β equal to 21 (Kg/m^2), FPA of -13° , entry velocity of 5.5 (Km/s),

and entry altitude in the Mars atmosphere of 125 (Km) has been carried out. Figure 4.1.5 shows the trend of the main trajectory parameters as a function of the altitude.

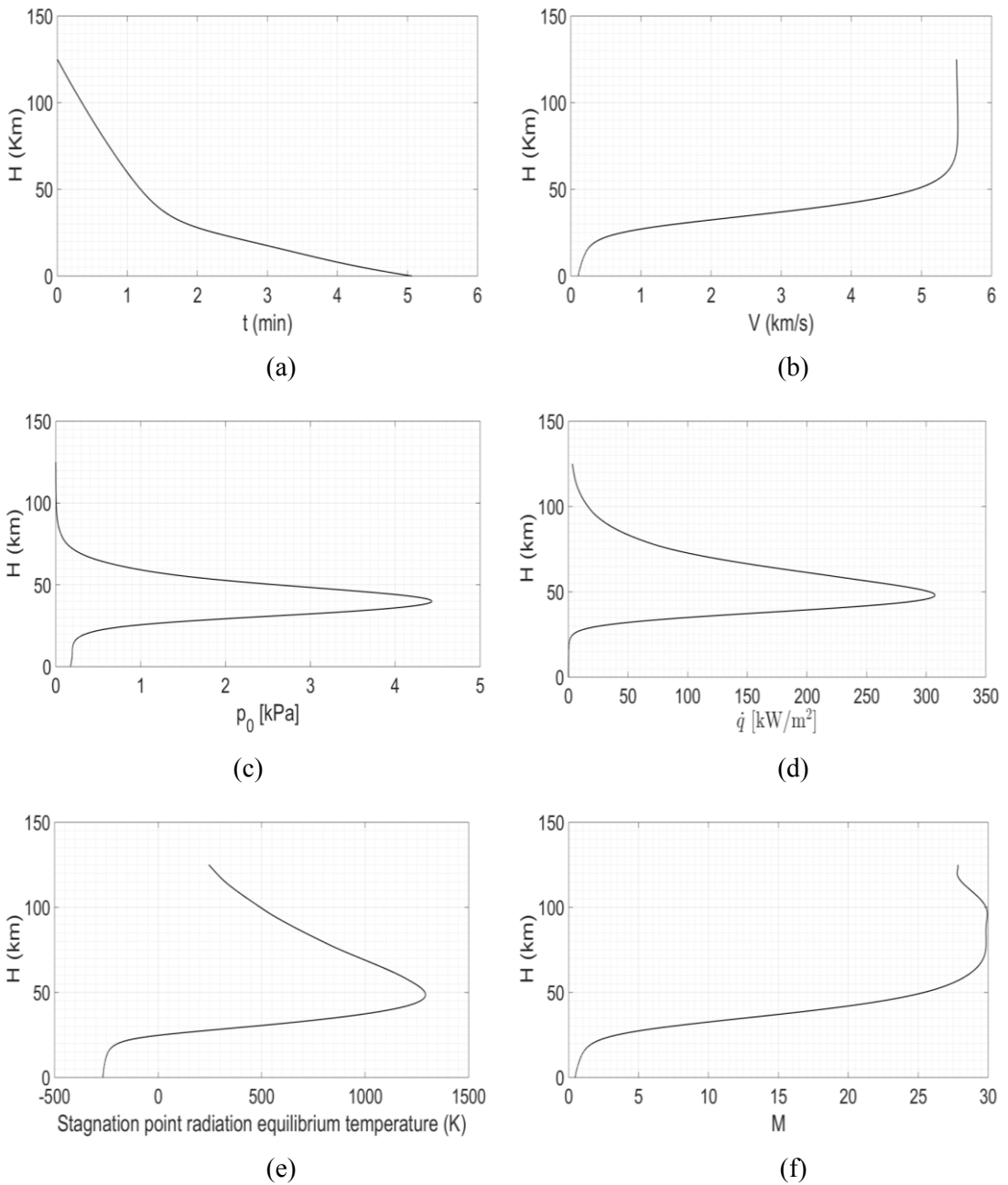


Figure 4.1.5 - Mars entry trajectory duration (a), the entry velocity (b), maximum stagnation point pressure (c), the maximum stagnation point heat flux (d), the maximum radiative equilibrium temperature (e) and the Mach number (f).

A comparison among past Mars entry trajectories and a nominal SMS Mars entry trajectory has been conducted [21].

As shown in table Table 4.1.2 the possibility of using a deployable TPS significantly reduce the ballistic coefficient of the overall entry system.





	SMS	VIKING	PATHFINDER	PHOENIX
				
Relative Entry velocity (Km/s)	5.5	4.5	7.6	5.87
Relative Entry FPA [°]	-15	-17.6	-13.8	-13.2
Ballistic Parameter (Kg/m ²)	21	64	62	65
Entry altitude (Km)	125	82	125	125

Table 4.1.2- Mars landers entry parameters [21].

As shown in Figure 4.1.6 (c)-(d) for the SMS mission, stagnation point heat flux and stagnation point pressure are more than 2.5 times smaller than other EDL systems studied for Mars atmospheric entry that have used a fixed heat shield.

This result proves that without the use of any external, complicated and expensive aero brake system, the landing performances have been improved by two or 3 times, respect a fixed shield.

Although the velocity during the entry path is much slower than the several km/s of the entry velocity of the capsules that present a fixed heat shield (see Figure 4.1.6(a)), it is still too large as impact velocity for a lander. As a result, all previous and currently planned EDL architectures deploy a supersonic parachute to increase the descent β and slow the vehicle to subsonic speeds before too much altitude is lost. In addition, due to the Mars atmosphere particularly thin, another challenge is to reduce the velocity in a shorter distance, since the parachute inflation occurs at lower altitude compared to the Earth atmosphere.

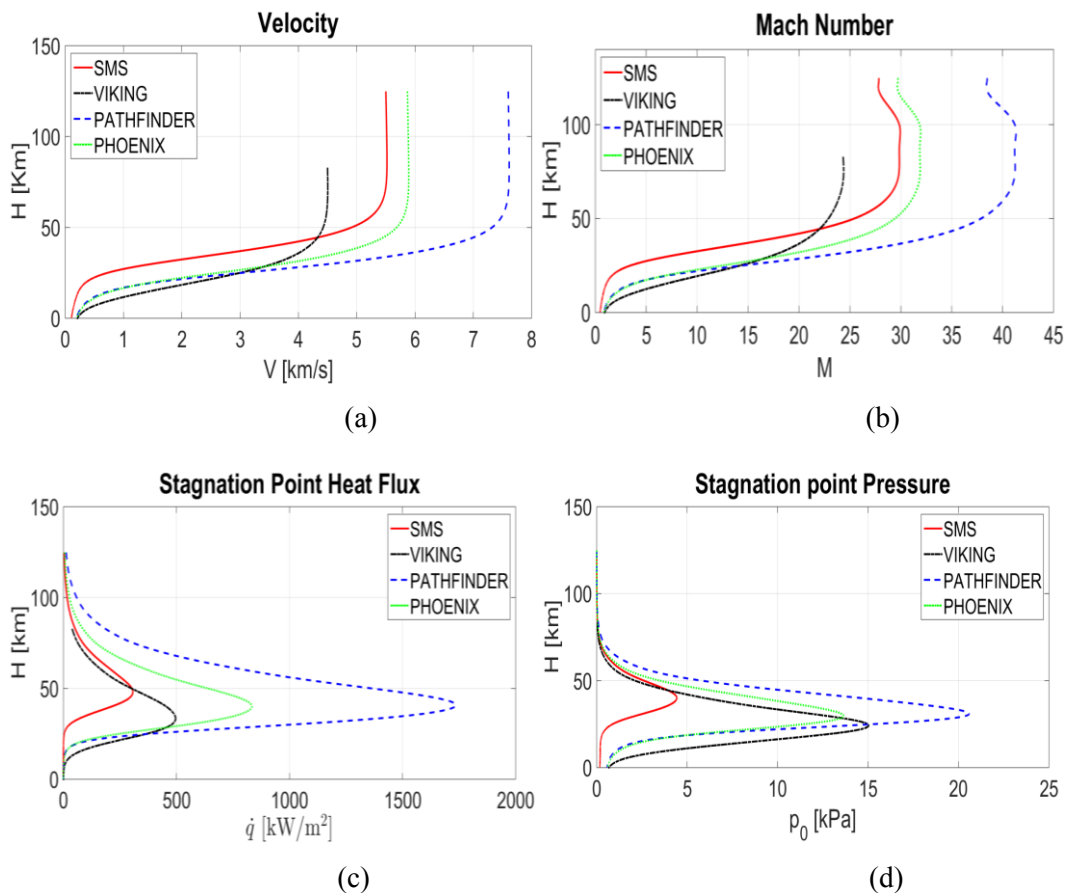


Figure 4.1.6 – Speed (a), Mach number (b), Stagnation point heat flux (c) and stagnation point pressure (d) of SMS and three previous Mars landers (Viking, MPF and Phoenix).

As shown in Figure 4.1.6 (b), thanks to the “umbrella like” concept, the SMS capsule reaches a subsonic regime at higher altitudes than previous landers. This allows reducing the complexity of the system using a single subsonic parachute, and reduces the cost of the overall mission. The use of a subsonic parachute is very important because it also allows reducing, or eliminating, the instability and fluctuations.

Therefore, a parachute analysis has been carried out to assess the performance of SMS in terms of landing capability using a single subsonic parachute. In order to simulate the shield ejection in the entry trajectory after the parachute deployment, an analysis of the variation of the landing speed as a function of the lander mass has been performed. For this analysis, four alternative values for the diameter have been considered (see Figure 4.1.7).

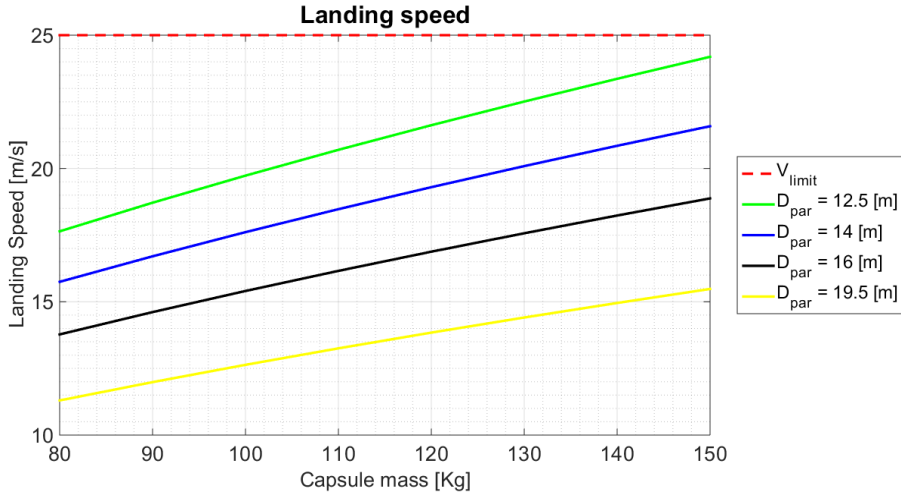


Figure 4.1.7 – SMS landing speed using a subsonic parachute

As shown in Figure 4.1.7 using a subsonic parachute and ejecting the TPS during the descent phase, the landing speed can be sensitively reduced to values lower than 18 (m/s) which is a speed compatible with the use of a passive shock absorber, such as a vented air bag.

4.2 Hypersonic CFD aerothermodynamics

This part of the work provides the study of aerothermodynamics. The work is intended to assess the thermal and aerodynamic loads in the most severe conditions along the capsule reentry path shown in Section 4.1.

The two-dimensional and three-dimensional computations in continuum flow regime, i.e. at altitudes below 70 km, have been obtained by Computational Fluid Dynamics (CFD), by means of the commercial code *Cd-Adapco STAR-CCM+ v. 10* [42].

In particular, two-dimensional axisymmetric analysis allow estimating the distribution of the thermal and mechanical loads on the surface of the capsule and the drag coefficient under the axisymmetric hypothesis. The three-dimensional analysis allow to calculate the pressure and thermal distribution on the capsule TPS.

Table 4.2.1 reports the free stream parameters and some operative test conditions for all the simulations carried out.

H (Km)	ρ (Kg/m ³)	T (K)	p (Pa)	V (Km/s)	M	Kn	Tw (K)
30	9.8e ⁻⁴	175	32.2	1.5	7.3	2e ⁻⁵	730
40	3.4e ⁻⁴	162.4	10.4	3.6	18.05	5.7e ⁻⁵	1400
50	1.08e ⁻⁴	152.2	3.09	4.9	25.5	1.8e ⁻⁴	1500
60	3.18e ⁻⁵	144.2	8.67e ⁻¹	5.36	28.5	5e ⁻⁴	1430
70	8.73e ⁻⁶	139.5	2.29e ⁻¹	5.49	29.6	2e ⁻³	1240

Table 4.2.1– Input data to CFD

Figure 4.2.1 shows the value of the free stream Knudsen number for the given capsule diameter according to the Mars atmosphere.

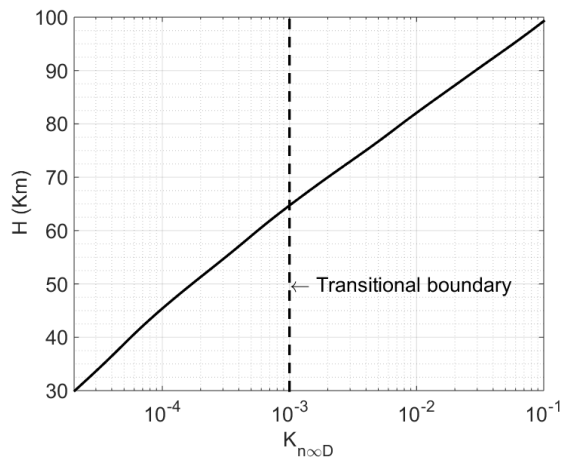


Figure 4.2.1–Knudsen number

The two-dimensional and three-dimensional computational grids (Figure 4.2.2) were generated by the software *ANSA 13.2* [74]. The two-dimensional grid is composed of about 40,000 quadrilateral cells, whose density becomes larger approaching the capsule. In particular, the nominal CFD computational grid used for simulations has been obtained adapting a coarser mesh in the shock layer. This choice provides the best resolution in the most critical region of the flow field where, in particular, high temperature and velocity gradients must be considered.

The three-dimensional grid has been created according to the capsule geometric parameters. The three-dimensional grid is composed of about 750,000 hexahedral cells, whose density becomes larger approaching the capsule surface. As well the two-dimensional

grid, the nominal CFD computational grid used for three-dimensional simulations has been obtained adapting a coarser mesh in the shock layer.

Different conditions were set for the computational domain boundaries for both cases: a pressure far-field condition was set for the boundary (labeled as 1), in order to model free stream conditions; axis-symmetry conditions for the symmetry surface for the two-dimensional simulation, and periodic conditions on the lateral surfaces of the three-dimensional model (labeled as 2); no-slip conditions for the surface of the capsule (labeled as 3); and a pressure outlet for the downstream surface (labeled as 4).

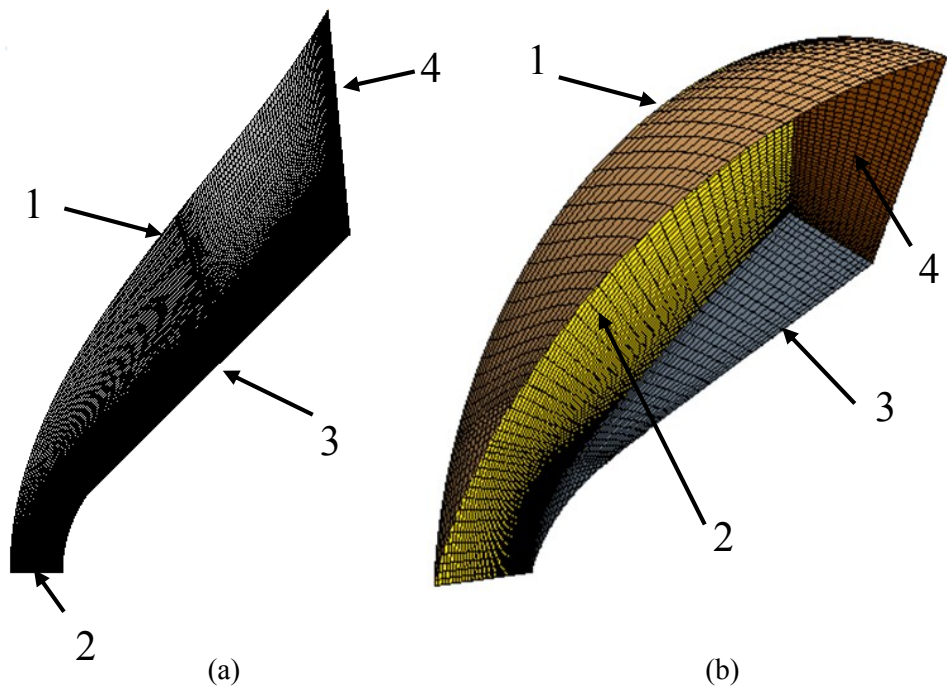


Figure 4.2.2 - Two-dimensional (a) and three-dimensional (b) CFD mesh.

The free stream conditions have been imposed according to the entry trajectories parameters reported in Table 4.2.1. The no-slip assumption on the wall was justified by the nearly continuum regime, because CFD analyses have been performed only for Knudsen numbers less than $2e^{-3}$. All numerical simulations considered fully-catalytic wall conditions, assuming a constant wall temperature as shown in Table 4.2.1. These assumptions have been made to get estimations for the hot-wall convective heat flux. For the three-dimensional simulation a radiation model, using surface-to-surface radiation approach implemented in

Cd-Adapco STAR-CCM+ v. 10 has been used, in order to predict the radiative equilibrium temperature of the capsule surface at maximum stagnation pressure condition. To this end, an emissivity coefficient for the capsule surface of 0.8 has been selected.

The Mars two-dimensional tests were aimed at the evaluation of the drag coefficients at zero angle of attack as a function of altitude and at the evaluation of local quantities such as heat flux and pressure along the capsule surface.

Figures from 4.2.3 to 4.2.7 show the pressure distribution along the capsule at altitudes from 30 to 70 Km computed by the CFD code. As shown, there is good agreement in terms of stagnation point pressure between the hypersonic Newton's theory (Equation (3.1.3)) and the CFD results.

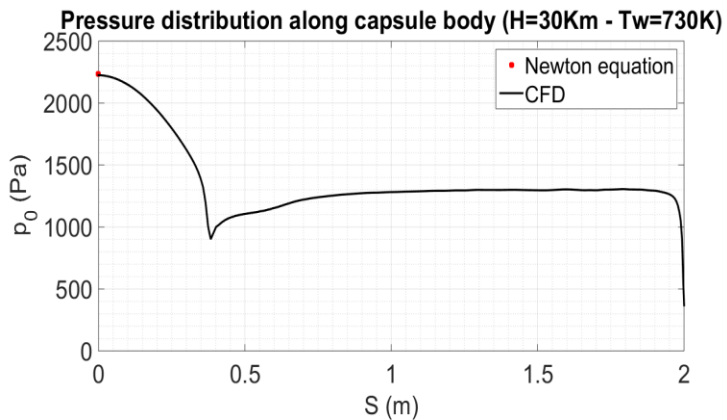


Figure 4.2.3 - CFD pressure distribution at 30 Km

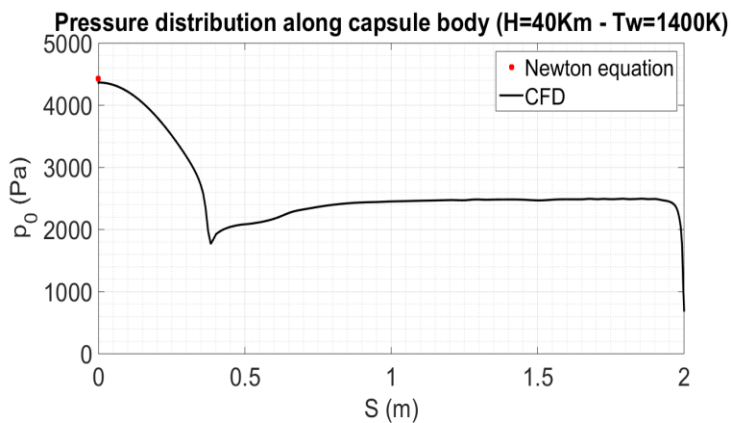


Figure 4.2.4 - CFD pressure distribution at 40 Km

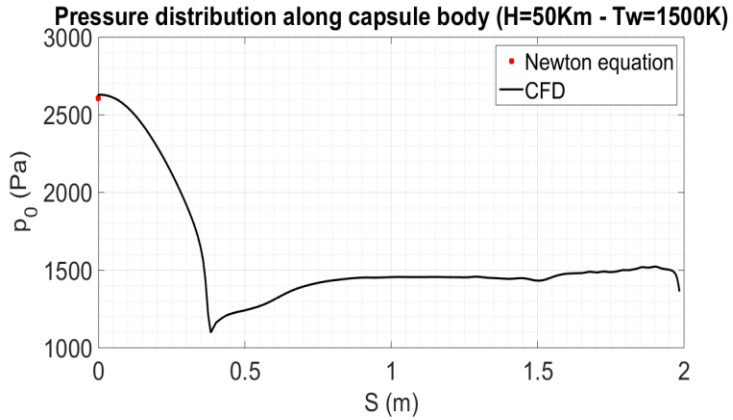


Figure 4.2.5 - CFD pressure distribution at 50 Km

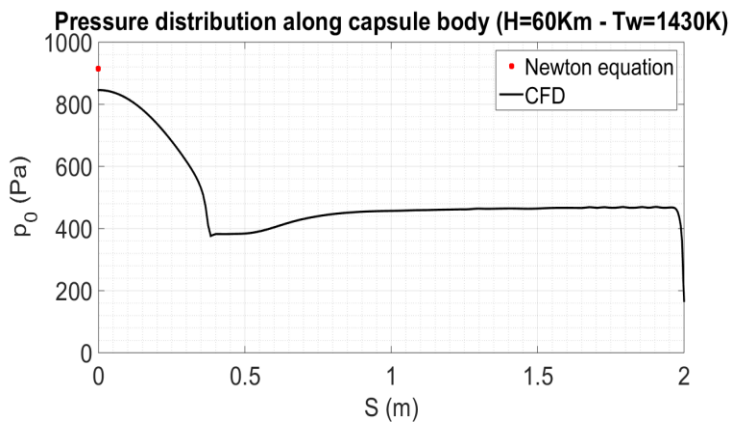


Figure 4.2.6 - CFD pressure distribution at 60 Km

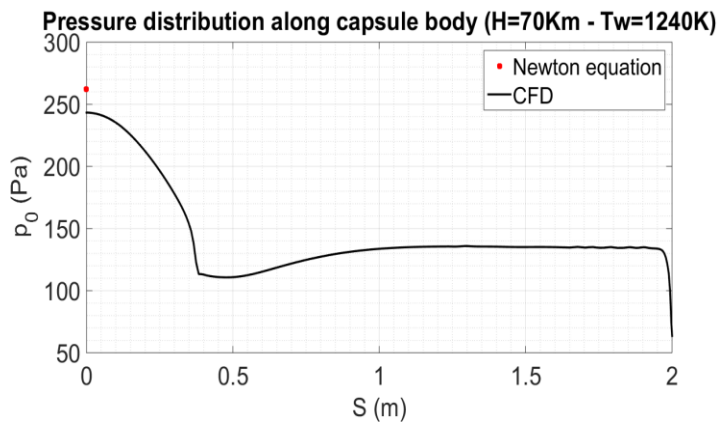


Figure 4.2.7 - CFD pressure distribution at 70 Km

Furthermore, in order to preliminary predict the heat flux distribution on the capsule surface, Figures from 4.2.8 to 4.2.10 show the distribution of the heat flux along the capsule at 30 Km, 50 Km, and 70 Km.

As expected the CFD results are coherent with the assumption of single component and ideal gas, made for the CFD flow, since the CFD code gives conservatives values of the stagnation point heat flux compared to the Tauber/Sutton theory (Equation (3.1.2)).

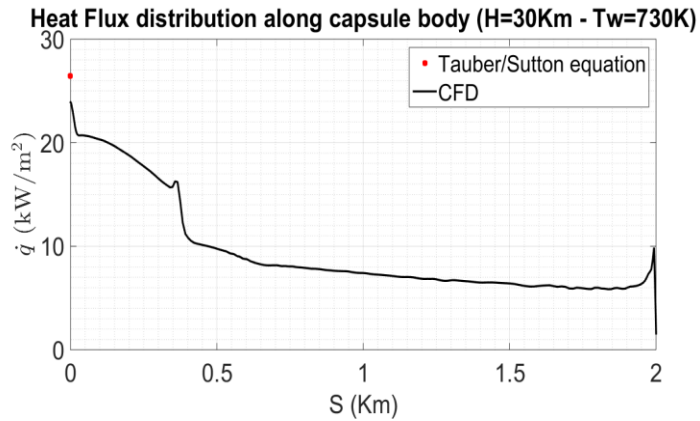


Figure 4.2.8 - CFD heat flux distribution at 30 Km

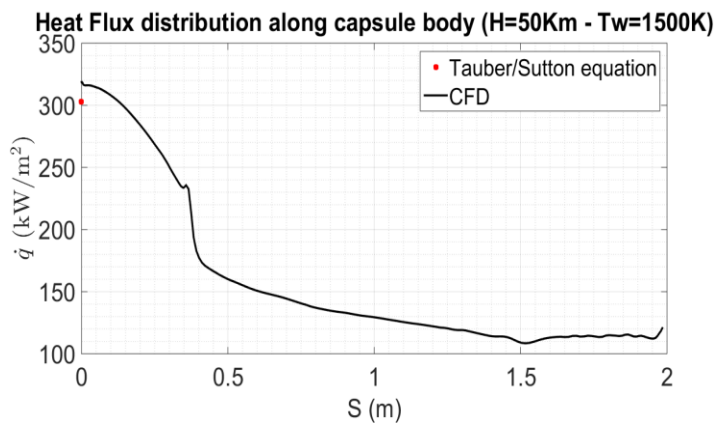


Figure 4.2.9 - CFD heat flux distribution at 50 Km

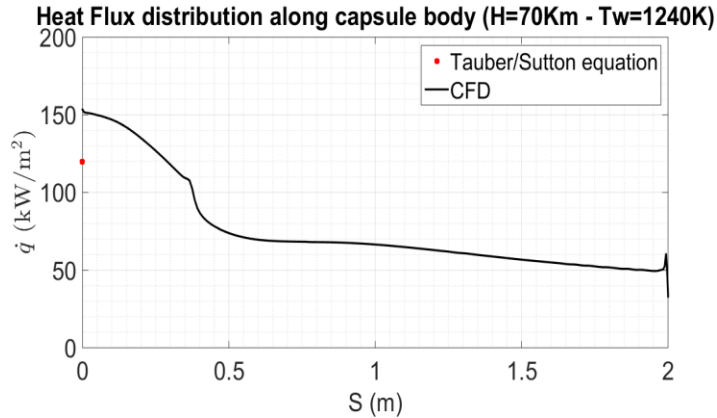


Figure 4.2.10 - CFD heat flux distribution at 70 Km

Figures 4.2.11 and 4.2.12 show the comparison between the stagnation point pressure and the stagnation point heat flux evaluated by the CFD and the equations of motion. As shown, there is good agreement in terms of stagnation point pressure prediction (see Figure 4.2.11); this means that the Newton theory is a valuable tool to predict the stagnation point pressure for a blunt body in hypersonic flow field. Regarding the stagnation point heat flux, as well known, the correct evaluation of this parameter during the planetary entry trajectory is a very hard task to accomplish. Moreover, the more the altitude decrease (entering in the continuum flow regime), the more the CFD code results are closer to the Tauber/Sutton equation results. Furthermore, the drag coefficient evaluated using the CFD calculations has been shown in Figure 4.2.13. This result proves goodness of the assumption of a C_d equal to 1 for the preliminary evaluation using the dynamic equation of motion presented in Section 4.1.

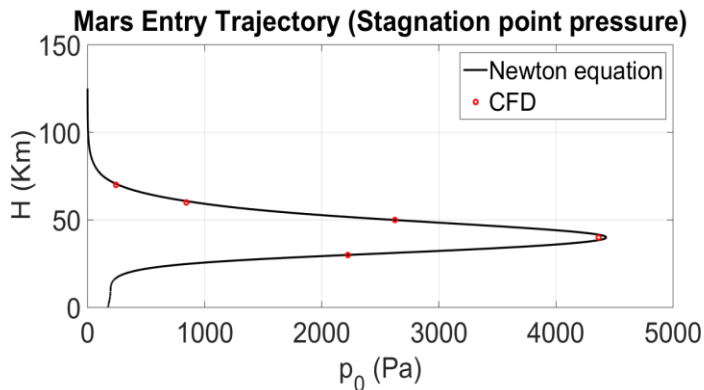


Figure 4.2.11 – CFD and Newton theory comparison results

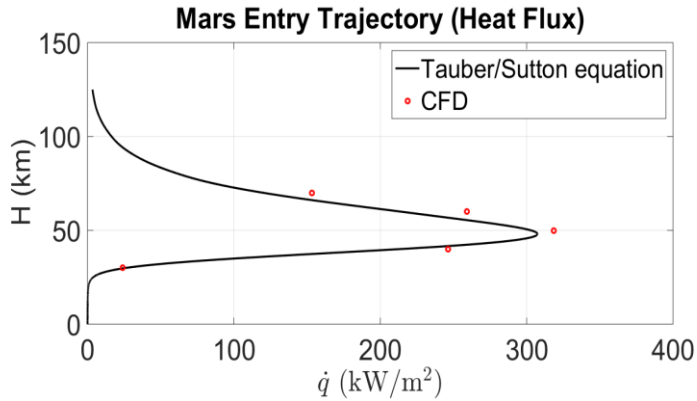


Figure 4.2.12 – CFD and Tauber/Sutton equation comparison results

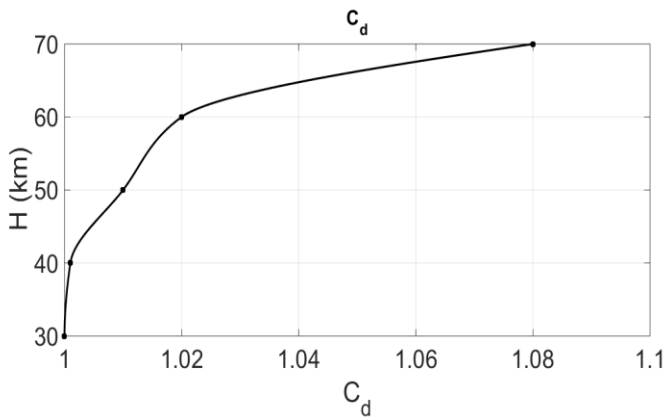


Figure 4.2.13 – CFD drag coefficient

In order to show the flow field around the capsule at maximum stagnation point pressure and maximum stagnation point heat flux conditions, Figures 4.2.14 and 4.2.15 show the Mach number, the pressure and the temperature contours around the capsule nose for the aforementioned conditions.

Furthermore, the CFD three-dimensional results show the pressure distribution, the convective heat flux distribution and the temperature distribution on the capsule surface at the maximum stagnation point pressure condition (40 Km) (see Figures from 4.2.16 to 4.2.18) and at the maximum stagnation point heat flux condition (50 Km) (see Figures from 4.2.19 to 4.2.21).

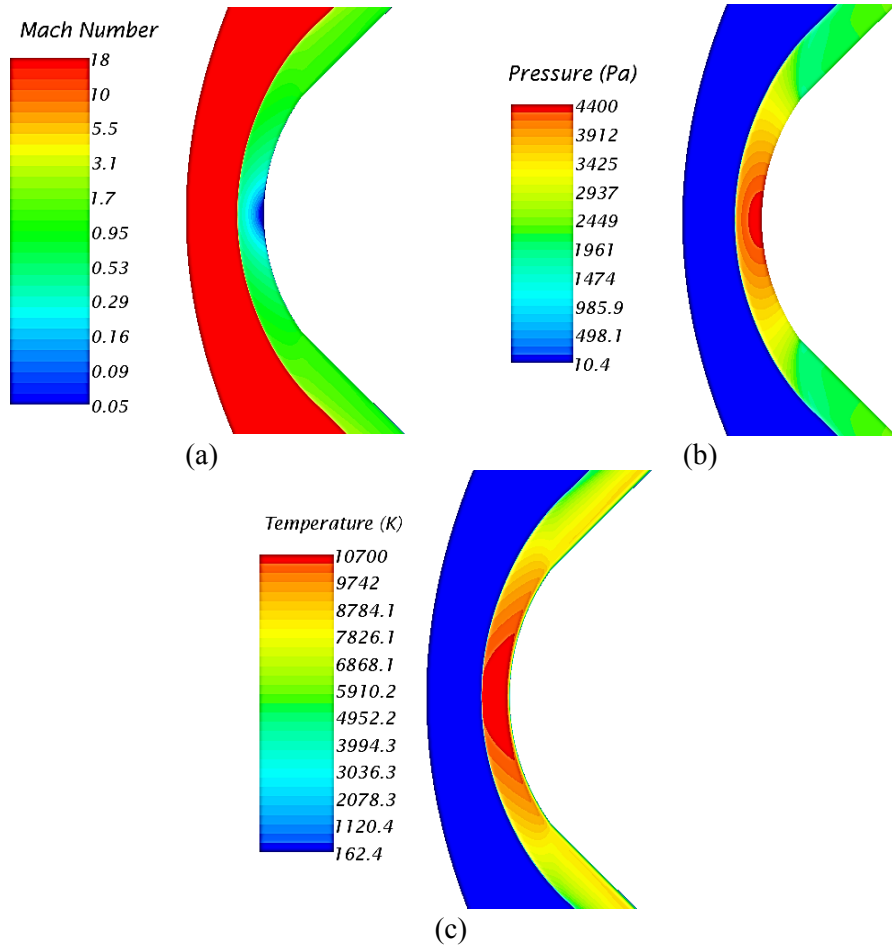


Figure 4.2.14 - Mach number (a), Pressure (b) and Temperature (c) contours at maximum stagnation point pressure condition (40 Km)

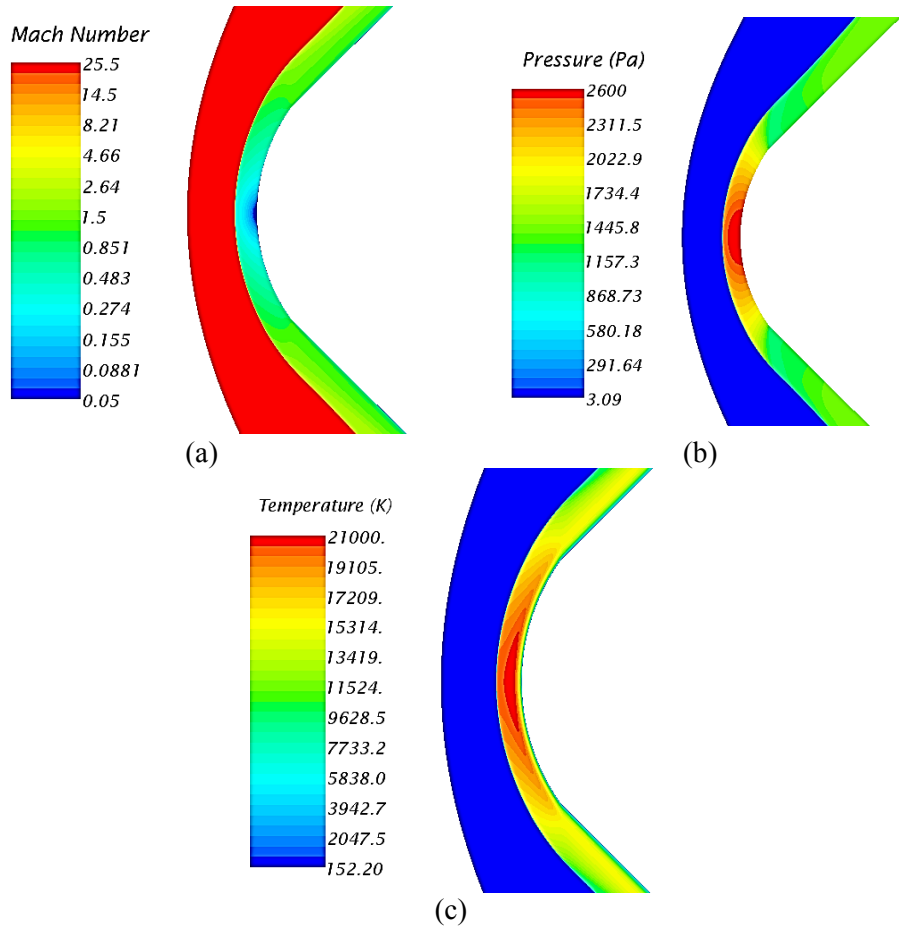


Figure 4.2.15 - Mach number (a), Pressure (b) and Temperature (c) contours at maximum stagnation point heat flux condition (50 Km)

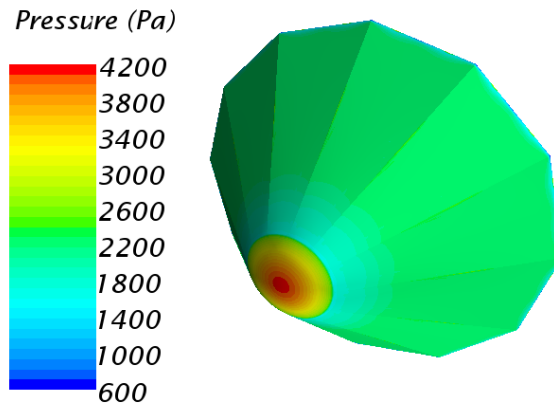


Figure 4.2.16 - CFD surface SMS pressure contour at maximum stagnation point pressure condition (40 Km)

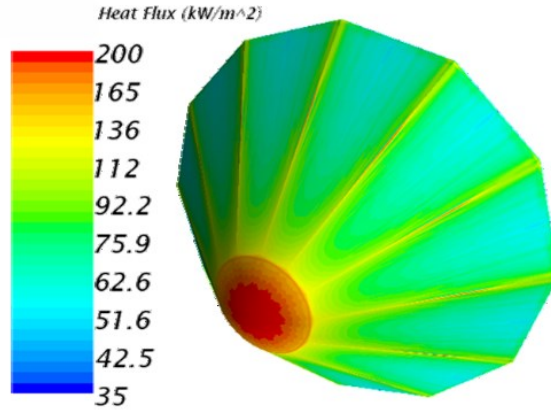


Figure 4.2.17 - CFD surface SMS heat flux contour at maximum stagnation point pressure condition (40 Km)

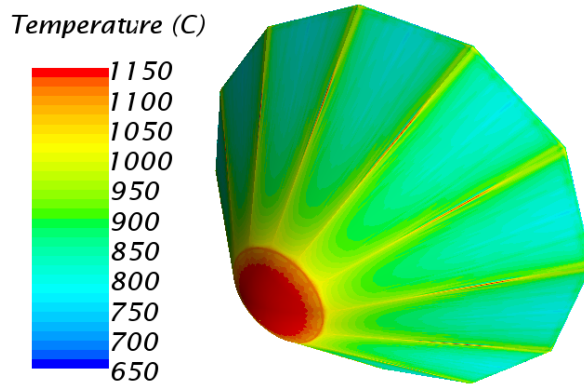


Figure 4.2.18 - CFD surface SMS temperature contour at maximum stagnation point pressure condition (40 Km)

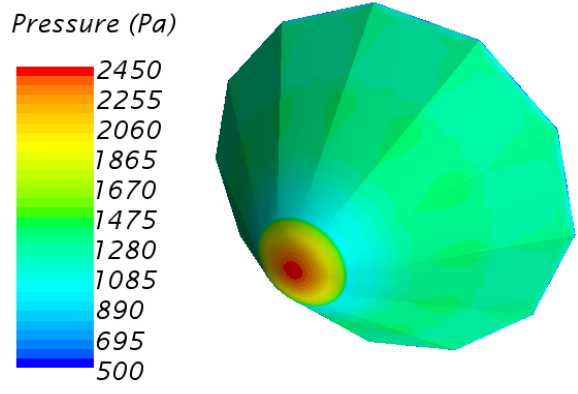


Figure 4.2.19 - CFD surface SMS pressure contour at maximum stagnation point heat flux condition (50 Km)

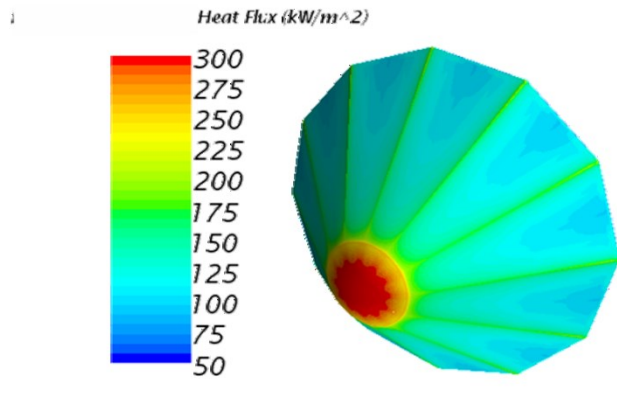


Figure 4.2.20 - CFD surface SMS heat flux contour at maximum stagnation point heat flux condition (50 Km)

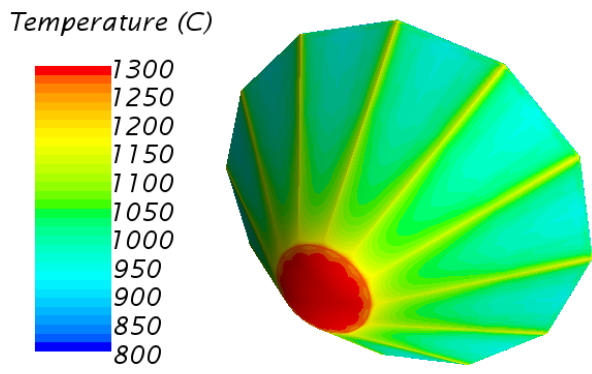


Figure 4.2.21 - CFD surface SMS temperature contour at maximum stagnation point heat flux condition (50 Km)

5. Aero-Thermal (AT) and Aero-Elastic (AE) Analysis of Flexible Materials

In order to develop a computational methodology to investigate the AT and the AE behavior of several materials, in the present section a loosely coupled FSI approach based on the integration of structural and fluid dynamic commercial software and the non-linear theoretical model based on the natural modes of the structure described in Section 3.4 are presented.

First, the coupled FSI approach for the AT interaction is applied and validated considering the work carried out at NASA Langley Research center [65] - [67]. The aim of that work was to test several candidate materials for the TPS of the IRVE-3 experiment program for the severe thermal conditions experienced by the flexible TPS along a planetary entry trajectory.

Then, the computational study of the non-linear AE behavior of a multi-layered TPS is presented. In order to validate the specific computational model and the overall strategy for structural and aerodynamics analyses of flexible structures, the simplified TPS sample tested in the 8' High Temperature Tunnel (HTT) at NASA LaRC has been selected as a baseline for the validation of the present work [59].

5.1 AT response of a multi-layer TPS using a FSI loosely coupled approach

In order to validate and present the FSI approach for the AT interaction the work carried out at NASA Langley Research center [65] - [67] has been considered.

The experimental tests have been conducted in the 8' Foot HTT combustion heated, hypersonic blow-down wind tunnel. The duration of the test was approximately 90 sec. A dual wedge sled was mounted in the wind gallery so that two test conditions could be run simultaneously (see Figure 5.1.1).

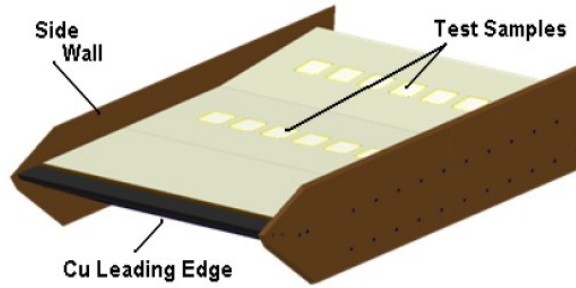


Figure 5.1.1 - Sketch of the test sled [65].

The low-pressure conditions presented by Hughes et al. [65] at a sled angle of 5° have been selected (see Table 5.1.1). A comparison between CFD results conducted with the commercial code *Vulcan v6.0.1* [65], and *Cd-Adapco STAR-CCM+ v.10* [42] CFD code is summarized in Table 5.1.2.

Low-pressure test conditions

Composition – Mole fractions	N ₂ =0.7154, O ₂ =0.0237, CO ₂ =0.0841, H ₂ O=0.1682, Ar=0.0086
Flow Conditions	<ul style="list-style-type: none"> • Mach 7 • 813 (Pa) • 206 (K) • 2039 (m/s)

Table 5.1.1 - Definition of low-pressure tunnel conditions [65].

Sample AoA	Sled AoA	<i>Vulcan</i>		<i>STAR-CCM+</i>	
		HFL (W/cm ²)	Pressure (Pa)	HFL (W/cm ²)	Pressure (Pa)
10	5	11	3740	11,2	3776
5	5	5,9	1860	6,1	1848

Table 5.1.2 - CFD results comparison

AT coupling has been simulated using two commercial codes, *Abaqus/Standard v 6.13* for the material thermal distribution, and *Cd Adapco STAR-CCM+ v 10* to solve flow motion equations and aerodynamic heating conditions. For the structural model an uncoupled heat transfer implicit scheme has been used, in which the temperature field is calculated without considering the stress/deformation study. Diffusive heat transfer elements (DC3D8) have been selected from *Abaqus/Standard v 6.13* elements library to simulate the thermal conduction inside the texture. The flow field is turbulent and the numerical simulations have been performed with a K-Epsilon 3D, time implicit numerical scheme. The *SIMULIA Co-Simulation Engine (CSE)* solver has been used to exchange data between the two model interfaces.

An implicit staggered numerical scheme (Figure 5.1.2) has been used to realize data transfer between the Fluid Dynamic solver *Cd Adapco STAR-CCM+ v 10* and the FE structural solver *Abaqus/Standard v 6.13*. In order to simulate a steady state condition a time step (T_s) of 0.5 (s) and a maximum physical time of 90 (s) have been set.

As shown in Figure 5.1.2, for each time step the boundary heat flux evaluated by the fluid solver (1) is projected on the structural surface (2). Then, the FE solver calculates the temperature field (3) and project it on the fluid domain (4). In an implicit time scheme, this transfer can occur more times per step, until convergence is reached. Since we are utilizing a domain-decomposition approach, each domain will be suitably discretized for the appropriate solver.

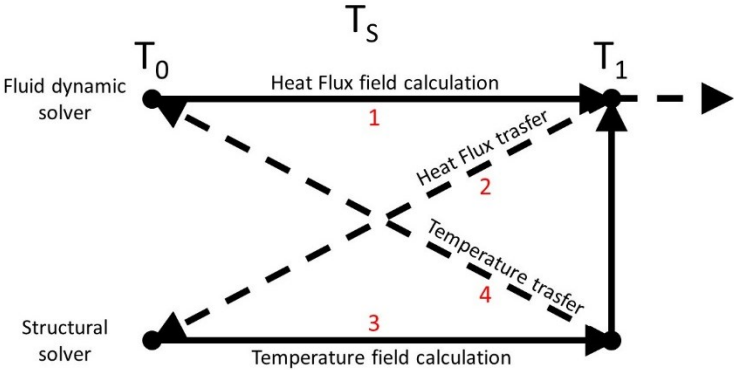


Figure 5.1.2 - Implicit staggered algorithm for each time step

As benchmark sample, the layup 6 shown in Figure 5.1.3, placed in a forward location, and the low-pressure flow condition have been selected, due to the good nominal results

obtained by experimental tests. The top surface of the layup 6 structural model has been coupled with the relative wall of the CFD domain according to the dimensions reported by Del Corso, Bruce, Liles and Hughes [66]; only a section of the wind tunnel has been modeled (see Figure 5.1.4). The layup 6 is a Coupon TPS made of four layers. The Refrasil C1554-48 outer fabric layer is exposed directly to the Mach 7 flow in the 8’HTT. The Pyrogel 6650 insulator fabric is used to prevent excessive heating through the thickness. The Kapton fabric is intended to act as a gas barrier between the aero-shell bladder and the aero-shell TPS. All layers material properties are summarized in Table 5.1.3. As evaluated by Del Corso, Bruce, Liles, and Hughes [66], a contact resistance of 18 (m^2K/W) has been introduced to simulate the gap among texture layers.

Material	Layer Type	Thickness (mm)	Density (Kg/m ³)	Conductivity (W/m·K)	Specific Heat (J/Kg·K)	Emissivity
Refrasil C1554-48	Outer	0.66	924	0.865	1172	0.7
Pyrogel 6650	Insulator	6.35	110	0.01 at 0°C 0.02 at 130°C 0.03 at 480°C	1046	-
Kapton	Barrier	0.03	1468	0.12	1022	-

Table 5.1.3 - Layup 6 material properties [65].

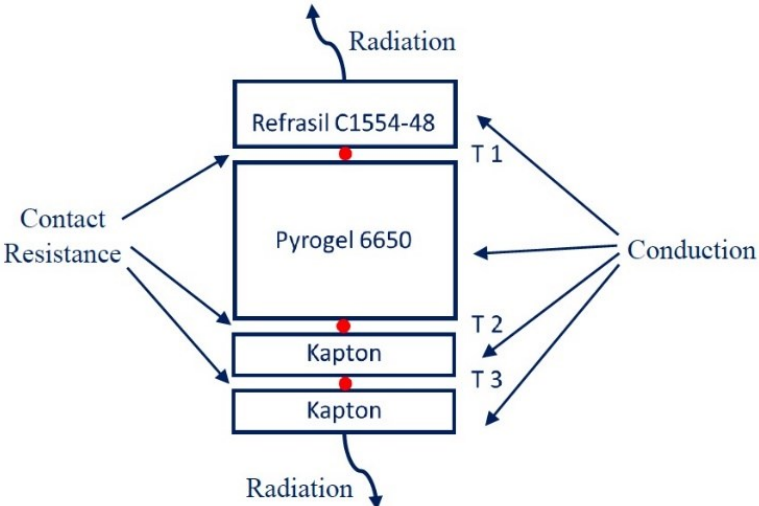


Figure 5.1.3 - TPS coupon layup 6 and thermocouple locations

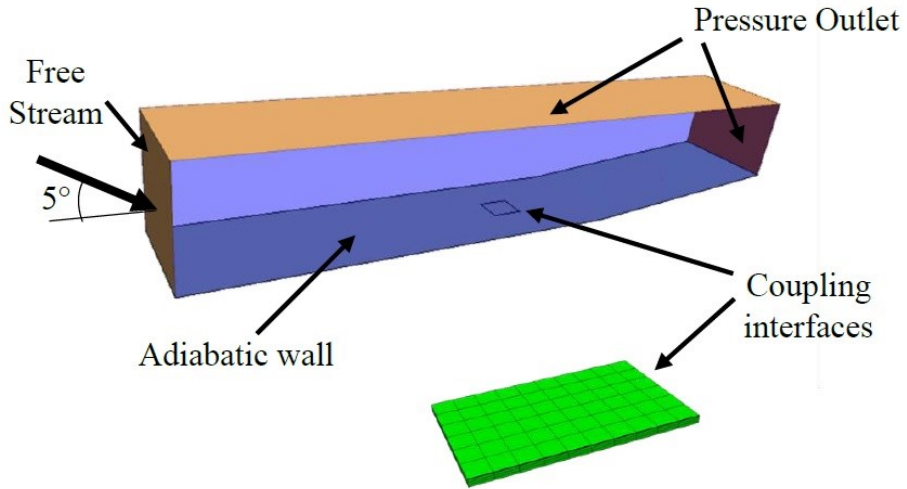


Figure 5.1.4 - CFD and FEM coupling models

Del Corso et al. [67] modeled and evaluated materials layup and TPS coupon using MSC Patran Thermal [75]. While Del Corso et al. [67] obtained the temperature distribution through the layup 6 applying the constant value of the Heat Flux ($5.9 \text{ (W/cm}^2\text{)}$) on the top surface of the TPS coupon. In the FSI loosely coupled approach, the Heat Flux between the TPS and the fluid has been updated for each time step, resulting in a more accurate solution. A comparison between experimental results, the AT interaction simulation methodology presented in this work, and the numerical simulation results presented by Hughes et al. [65] is depicted in Figure 5.1.5.

As shown, to simulate the AT interaction including the influence of the variation of the heat flux due to the variation of the surface temperature gives results that are more accurate.

Despite all, the transient is still a difficult part of the solution to simulate accurately.

As highlighted above, same material properties and flow conditions of the numerical simulations carried out at NASA LaRC have been used for the CFD-FEM coupling approach presented.

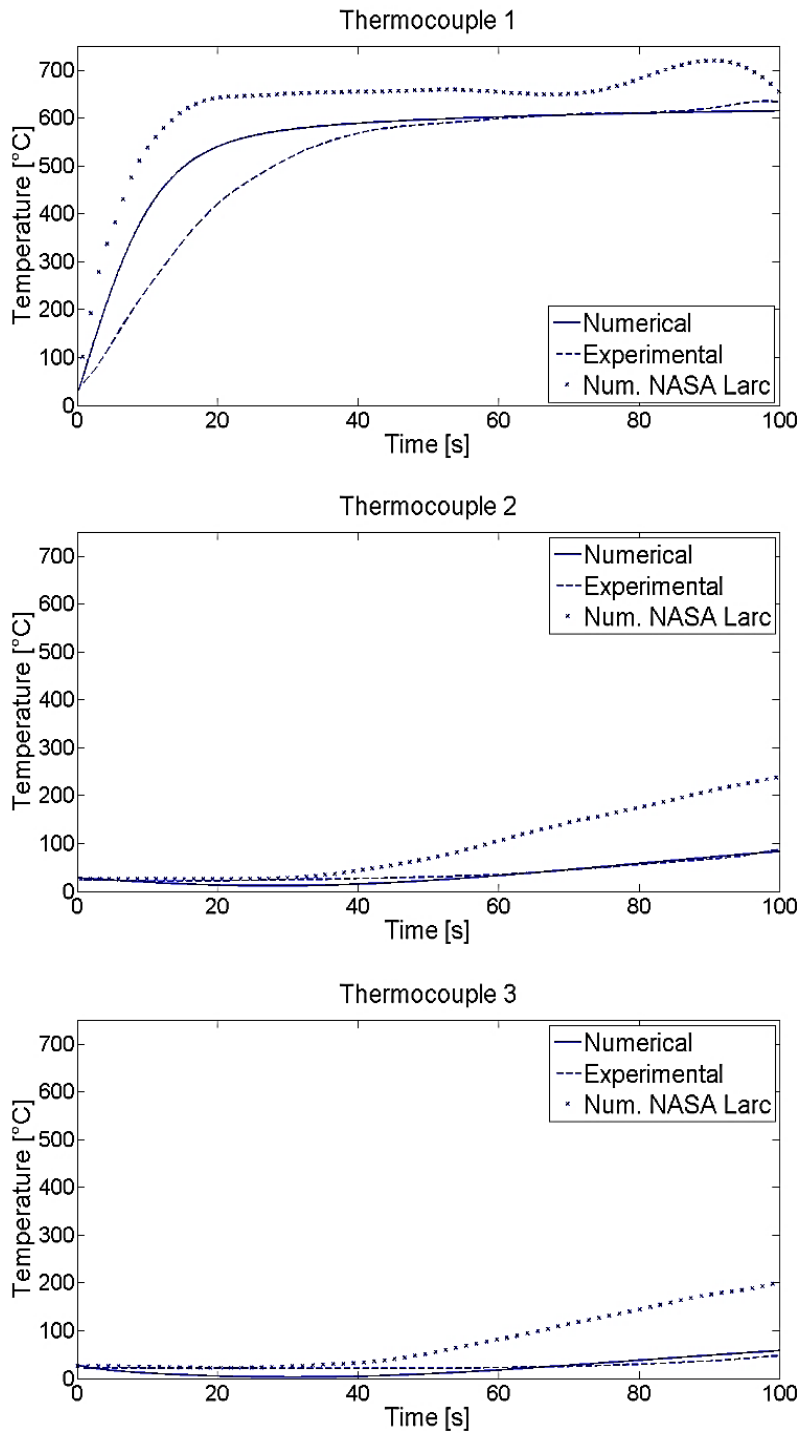


Figure 5.1.5 - Comparison between experimental and numerical results at Thermocouple 1 (top), Thermocouple 2 (middle), and Thermocouple 3 (low).

5.2 Non-linear AE response of a multi-layer TPS

In order to validate and present the specific Modal-Based (MB) computational AE model summarized in Section 3.4, the square TPS specimen tested in the 8' High Temperature Tunnel (HTT) [59] has been chosen as reference (see Figure 5.2.1).

The size of the sample is 60 (cm) x 60 (cm) and consists of two layers of Nextel 440-BF20 and one layer of Aluminized Kapton Kevlar (AKK), stitched together in a 5 cm square pattern.

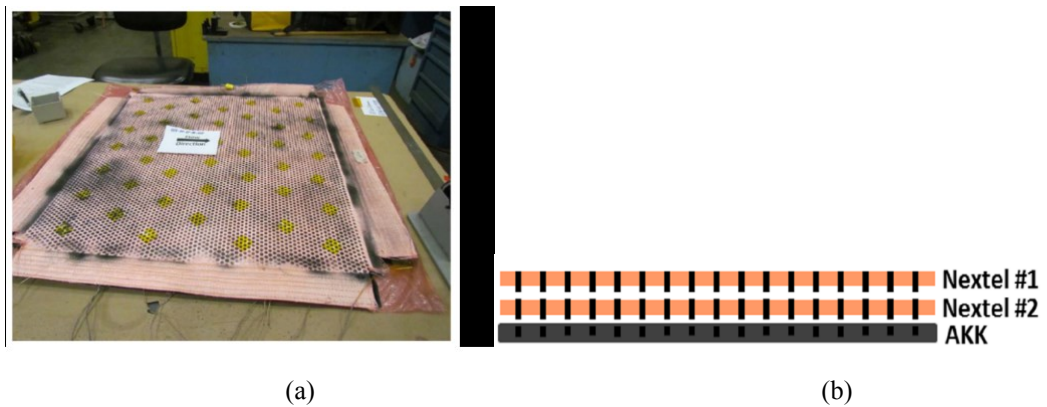


Figure 5.2.1 – TPS sample layout

Material properties of the Nextel and the AKK are given in Table 5.2.1.

<i>Material</i>	<i>Young's modulus E (GPa)</i>	<i>Poisson's ratio ν</i>	<i>Mass/area (Kg/m²)</i>	<i>Thickness (mm)</i>
<i>Nextel 440-BF20</i>	190	0.26	0.46	0.508
<i>Aluminized Kapton Kevlar (AKK)</i>	124	0.36	0.14	0.154

Table 5.2.1 - Material properties of the TPS layers

In addition to the analytical MB model presented in Section 3.4, obtained according to the aforementioned material and geometric properties, a FE model has been developed (see Figure 5.2.2) using the commercial software *Abaqus/Standard v 6.13* [43].

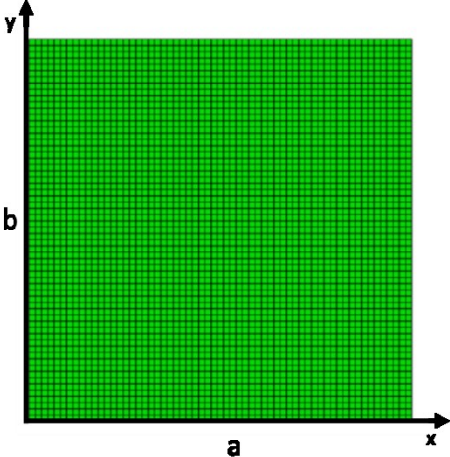


Figure 5.2.2 - Finite Element Mesh

where a and b are the TPS dimensions. The stitching between layers has been simulated with a 5 cm pattern using SPRINGA elements implemented in *Abaqus/Standard v 6.13*. (see Figure 5.2.3).

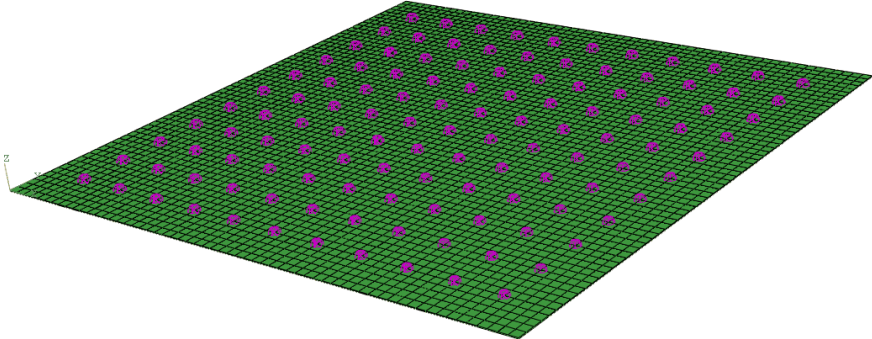


Figure 5.2.3 – Stitching pattern using spring elements

Finally, *SIMPLY-SUPPORTED* (SS) (out-of-plane displacements equal to 0) boundary conditions have been applied to the edges of the model for the case without pre-tensioning; while, due to the dynamic nature of the pre-tensioned problem, *PINNED* (all

displacements equal to 0) boundary conditions have been considered for the pre-tensioned simulation.

The FE model has been developed in order to correlate and validate the non-linear structural results obtained by the MB theory, without the aerodynamic influence.

To this end, since experimental Ground Vibration Tests (GVTs) have been performed, in order to validate the MB structural model, a comparison among an impulse analysis of the MB model, of the FE model, and the GVTs results has been made and presented in Section 5.2.1.

Then, the MB computational model has been used to numerically derive the AE behavior of the TPS under the hypersonic fluid conditions encountered in the 8thHTT, and the influence of the number of layers and the stitching pattern on the AE response. The results of the aforementioned simulations are presented in Section 5.2.2.

5.2.1 Structural non-linear response of the TPS

Before to test the square TPS sample in the 8thHTT, Ground Vibration Tests (GVTs) using two accelerometers and a transducer hammer have been performed. Those tests have been carried out with and without tension, in and out of the tunnel sled, and pre-and post-tunnel run (see Figure 2.2.1).

Therefore, in order to validate and present the structural part (i.e. without aerodynamics) of the non-linear computational MB model discussed in Section 3.4, a comparison among an impulse analysis of the MB model, of the FE model, and the GVTs results has been made.

Before evaluating the non-linear AE response of the fabric, it is of interest to calculate the linear natural frequencies of the TPS first, neglecting the non-linear terms S^L of the equation (3.4.13). Since it is preferred to have all three layers connected together to prevent hot gas from damaging the body of the entry capsule, a stitching stiffness k^{St} of 50000 (N/m) has been chosen for both the MB and the FE models.

Since the lower modes and natural frequencies are most important for the flutter behavior of the TPS, a total of 36 half-waves (6 on the x direction and 6 on the y direction) has been selected for the linear analysis. A comparison among natural frequencies of the three-layer fabric, including a pre-tension of 525 (N/m) as applied to the experimental

specimen, using eigenvalue extraction, has been summarized in Table 5.2.1.1, for both the MB and the FE analysis.

As shown, there is good agreement between the natural frequencies of the two models when the same SS BC's are applied, for the pre-tensioned simulation. While, for the untensioned case, there is a good agreement below 250 (Hz).

Furthermore, there is a small difference between the pre-tensioned natural frequencies evaluated with the MB model and the FE model with PINNED BC's.

Since it is not possible to have SS condition for the FE dynamic simulation, all the following pre-tensioned FE dynamic analysis are simulated with PINNED BC's.

The SS natural frequencies of the FE pre-tensioned case shown in Table 5.2.1.1 have the purpose to prove that the only source of difference between the MB case and the PINNED case are the BCs.

Mode	MB		FE		
	Untensioned (Hz)	Tensioned (525 N/m) (Hz)	Untensioned (Hz)	Tensioned (525 N/m) (Hz)	
				SS	PINNED
1,1	17.97	48.85	17.97	48.92	50.13
1,2 - 2,1	44.92	84.71	44.93	84.85	86.62
1,3 - 3,1	89.85	135.60	89.96	135.86	137.9
1,4 - 4,1	152.69	202.18	152.81	203.00	206.04
1,5 - 5,1	233.38	285.32	232.50	287.10	294.24
1,6 - 6,1	331.74	385.53	324.39	388.56	392.77
2,2	71.88	115.84	71.88	116.20	120.47
2,3 - 3,2	116.79	164.49	116.75	165.03	170.95
2,4 - 4,2	179.60	230.08	179.24	231.00	237.58
2,5 - 5,2	260.24	312.76	257.98	314.62	323.29
2,6 - 6,2	358.50	412.70	346.76	415.44	425.59
3,3	161.66	211.50	161.26	212.30	221.15
3,4 - 4,3	224.42	276.15	222.90	277.27	288.28
3,5 - 5,3	304.95	358.30	299.39	359.76	371.66
3,6 - 6,3	403.02	457.87	380.80	459.00	472.67
4,4	287.08	340.10	282.53	341.23	355.18
4,5 - 5,4	367.41	421.74	353.60	422.43	438.36
4,6 - 6,4	465.17	520.88	418.72	518.70	534.18
5,5	447.43	502.90	410.48	501.06	518.88
5,6 - 6,5	544.68	601.51	448.17	591.11	607.89
6,6	641.13	699.43	463.67	665.71	678.09

Table 5.2.1.1 – linear MB and FE natural frequencies using the eigenvalue extraction

Then, in order to compare non-linear analytical results with GVTs results, a dynamic response to an impulse force has been numerically developed. A value of 0.001 (N) has been set for the impulse force amplitude (F_{app} in the Equation (3.4.14)). In order to excite the greatest number of modes in the frequency interval of our interest, the force has been applied in a point with $x_0, y_0 = 0.1$. As done for the linear case, a number of 36 half-waves (6 on the x direction and 6 on the y direction) has been selected for the non-linear analysis.

The Fast Fourier Transform (FFT) of the specimen deflection and acceleration time histories is not a fully correct approach to compare the results with the linear natural frequency computation due to the non-linear characteristics of the present problem. Nevertheless, it allows one to verify the matching of peak frequencies and a first assessment of the overall vibrational response. For the above-mentioned reasons and due to some uncertainties about the experimental measurements, the successive plots report only normalized results.

Since the critical Rayleigh damping for the FE model assumes the expression shown in the Equation (3.3.7), α_R and β_R have been set in order to have the same amount of critical damping for the first two modes of the FE model and the MB model.

Furthermore, in order to figure out the right amount of critical damping, three critical damping values for the first two modes have been taken into account:

$$\zeta_{1,2}=0.01 ; \zeta_{1,2}=0.05 ; \zeta_{1,2}=0.1$$

Figure 5.2.1.1 shows the comparison among the experimental GVTs, the MB and the FE numerical average FFT results normalized by the maximum FFT amplitude for the displacement (a) and the acceleration (b) of the untensioned case with $\zeta_{1,2}=0.01$.

Then, Figure 5.2.1.2 shows the comparison among the experimental GVTs, the MB and the FE numerical FFT results normalized by the maximum FFT amplitude for the displacement (a) and the acceleration (b) of the untensioned case with $\zeta_{1,2}=0.05$.

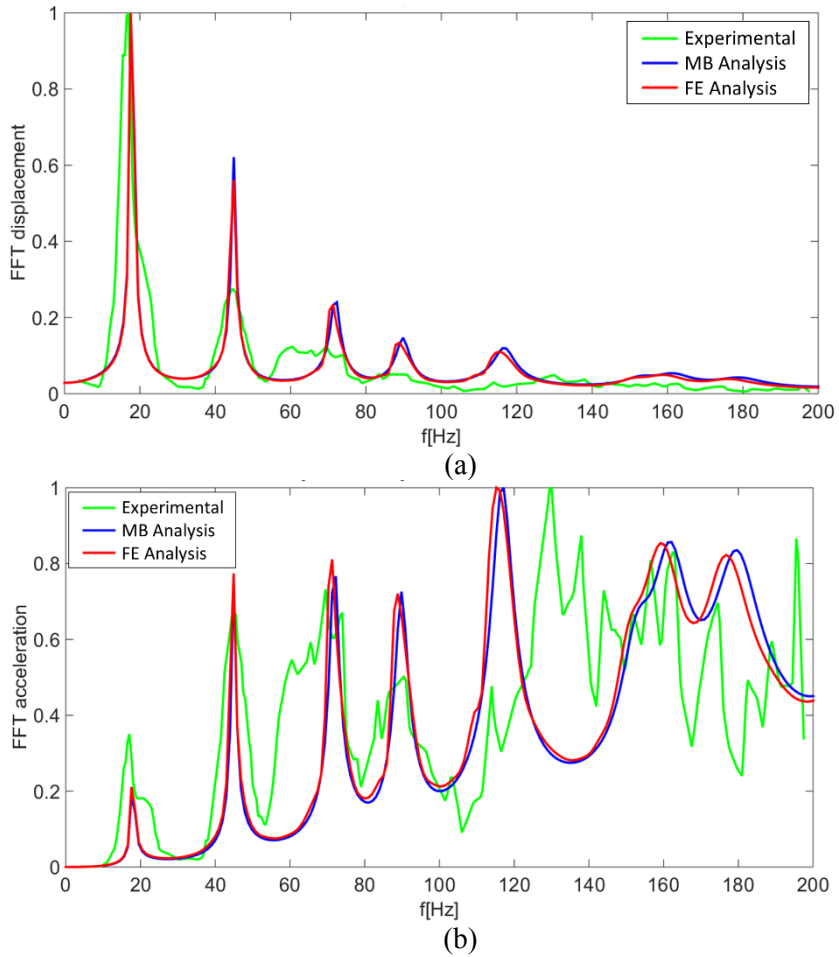
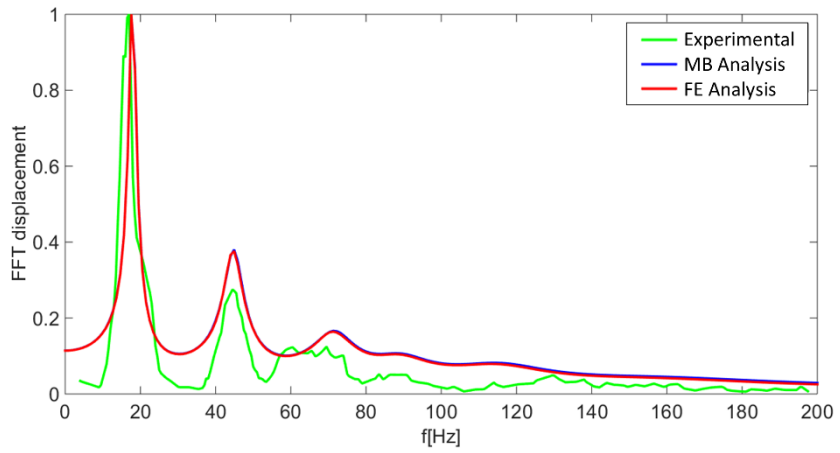
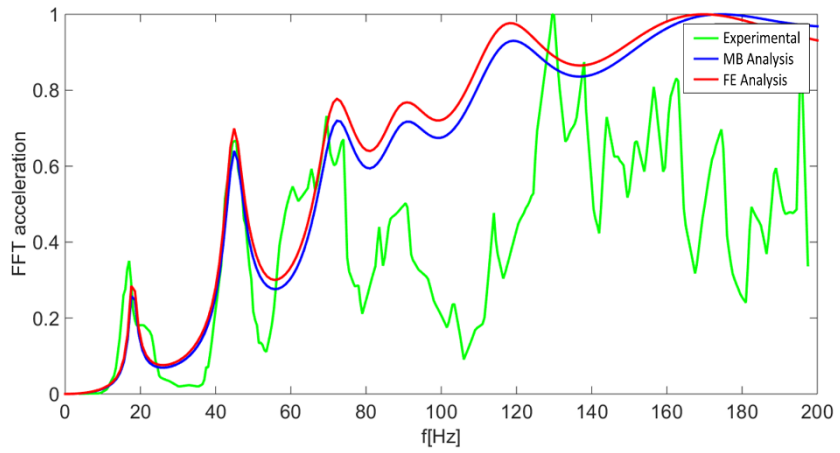


Figure 5.2.1.1 - Non-linear impulse response comparison normalized for the case with $\zeta_{1,2}=0.01$: FFT displacement (a) and FFT acceleration (b).

Finally, Figure 5.2.1.3 shows the comparison among the experimental GVTs, the MB and the FE numerical FFT results normalized by the maximum FFT amplitude for the displacement (a) and the acceleration (b) of the untensioned case with $\zeta_{1,2}=0.1$.

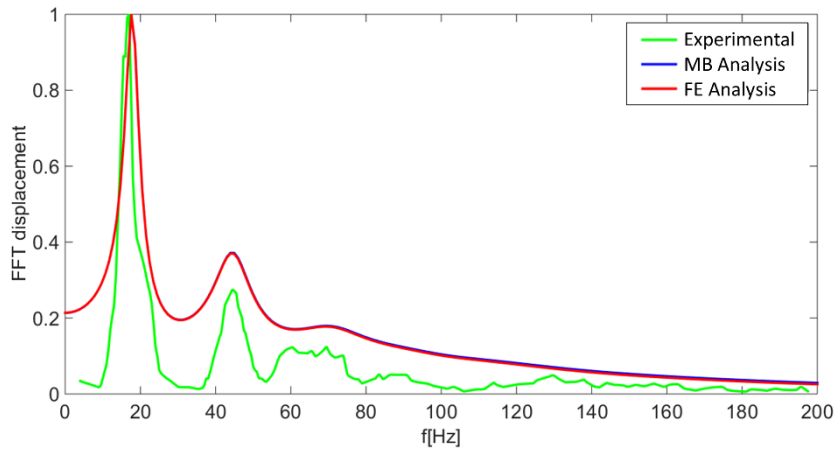


(a)

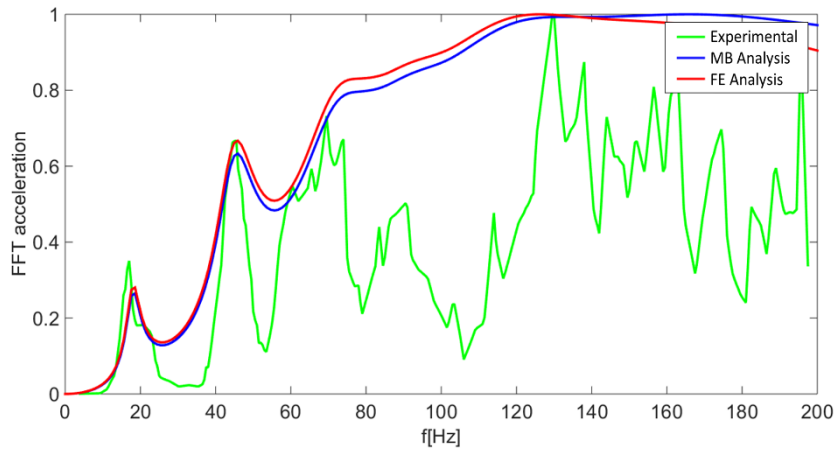


(b)

Figure 5.2.1.2 - Non-linear impulse response comparison normalized for the case with $\zeta_{1,2}=0.05$: FFT displacement (a) and FFT acceleration (b).



(a)



(b)

Figure 5.2.1.3 - Non-linear impulse response comparison normalized for the case with $\zeta_{1,2}=0.1$: FFT displacement (a) and FFT acceleration (b).

As shown, there is good agreement in terms of peak frequency location among the three cases. Furthermore, since the non-linear impulse response with $\zeta_{1,2}=0.01$ gives the best results, all the following AE simulations will be carried out with a critical damping for the first two modes of 0.01.

Moreover, a comparison among the experimental GVTs, the MB and the FE numerical FFT results normalized by the maximum FFT amplitude for the acceleration of the pre-tensioned case with $\zeta_{1,2}=0.01$ has been carried out (see Figure 5.2.1.4).

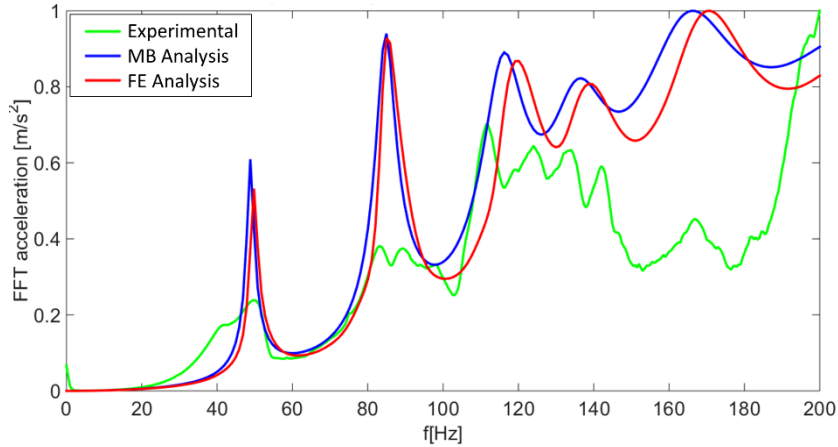


Figure 5.2.1.4 - Non-linear impulse response comparison normalized for the pre-tensioned case with $\zeta_{1,2}=0.01$.

Furthermore, a non-linear analysis response to a sinusoidal force applied to the center of the TPS, and with $\zeta_{1,2}=0.01$ has been carried out (see Figure 5.2.1.5).

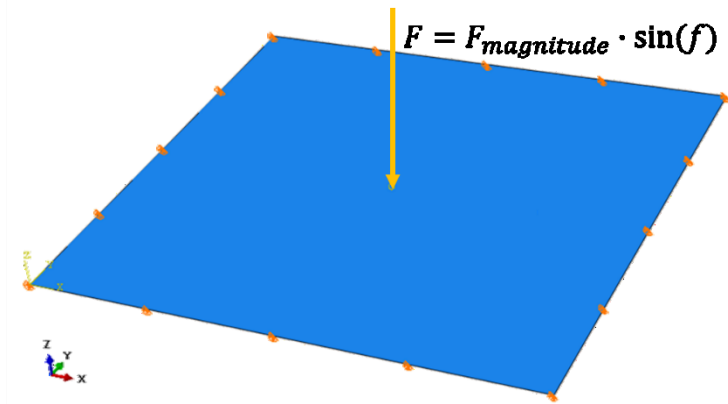


Figure 5.2.1.5 – Sketch of the TPS under the sinusoidal force applied to the center of the specimen

Where $F_{\text{magnitude}}$ is the Force magnitude and f is the force frequency. Figure 5.2.1.6 shows the time history comparison between the MB and the FE analysis of the deflection times the Nextel thickness ratio (W/h_N) at $F_{\text{magnitude}}=0.5$ (N) and f equal to the first natural frequency 17.89 (Hz) for the untensioned case, at the center of the plate. As shown, there is good agreement between the two solutions. This result proves even more the goodness of the MB code to predict the non-linear behavior of the TPS.

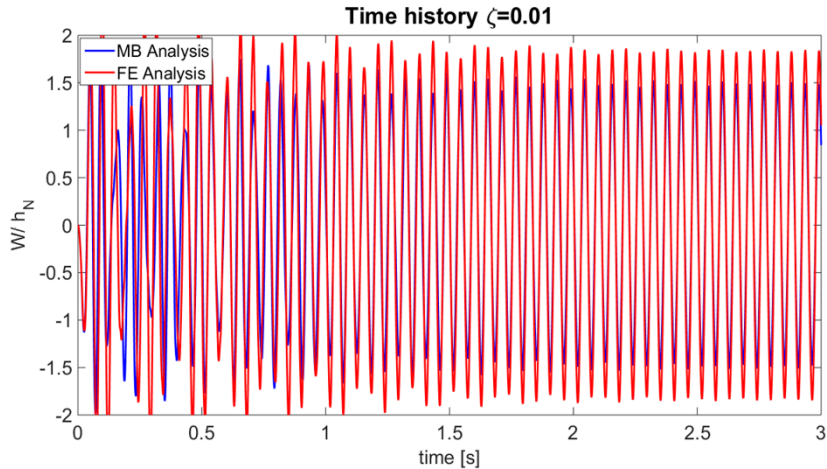


Figure 5.2.1.6 – Time history of the W/h_N ratio for the sinusoidal analysis with $f=17.89$ and $F_{\text{magnitude}}=0.5$.

Finally, an analysis of the force magnitude influence on the vibrational non-linear behaviour of the TPS has been carried out. This analysis has been obtained for three values of the force magnitude: 0.01, 0.1 and 0.5 (N); and for the untensioned and the pre-tensioned cases. Furthermore, the frequency swipe has been carried out in both directions; increasing (FWD) and decreasing (BWD) the force frequency.

Figure 5.2.1.7 shows the RMS of the ratio W/h_N , where h_N is the thickness of the Nextel, as a function of the force frequency for the three forces magnitude investigated for the untensioned case.

As expected, the more the force is increasing, the more the frequency peak increase and goes to higher frequencies. Moreover, while the force magnitude is 0.01 (N), the frequency peak of the FWD and the BWD solutions are the same, for the value of the force magnitude of 0.1 and 0.5 (N), the FWD and the BWD plots are not the same and the solution is non-linear.

Finally, Figure 5.2.1.8 shows the RMS of the W/h_N ratio as a function of the force frequency for the three forces magnitude investigated for the pre-tensioned case.

As shown, in this case, adding a pre-tensioning to the TPS edge, not only the natural frequency of the plate are increased, but even with a force magnitude of 0.1 (N) the FWD and BWD solutions have the same value.

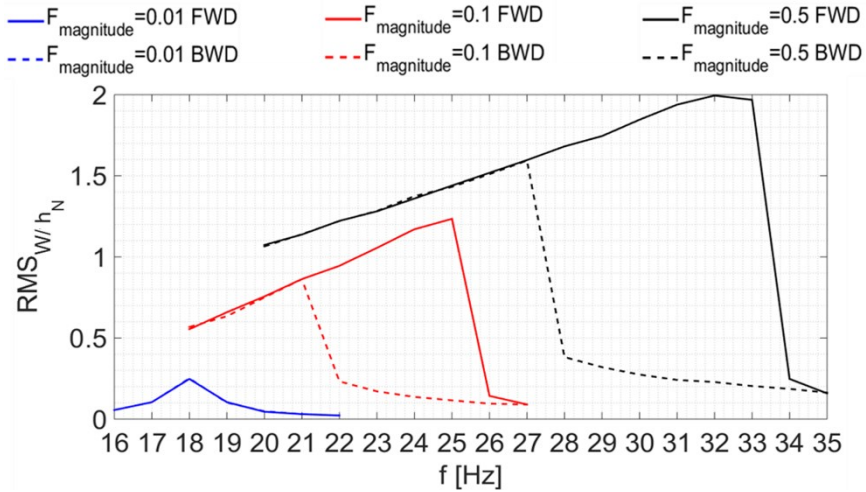


Figure 5.2.1.7 –RMS of the W/h_N ratio as a function of the frequency of the TPS for $F_{\text{magnitude}} = 0.01, 0.1$ and $0.5 (N)$: untensioned case

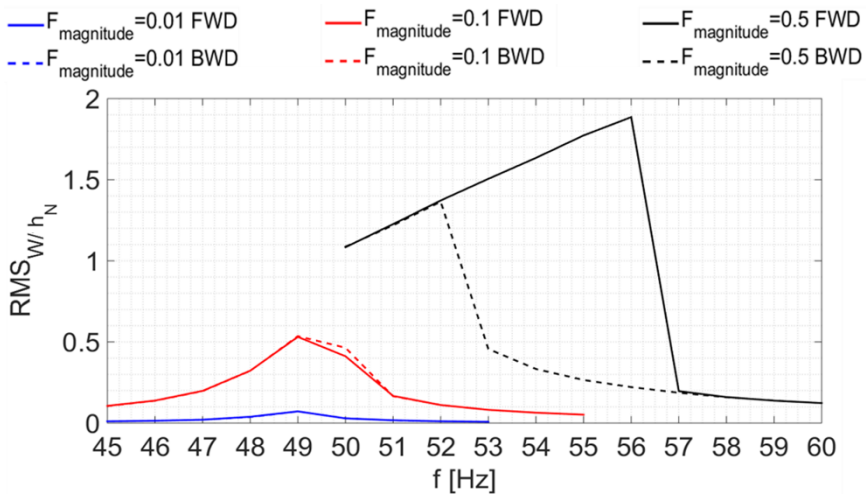


Figure 5.2.1.8 - RMS of the W/h_N ratio as a function of the frequency of the TPS for $F_{\text{magnitude}} = 0.01, 0.1$ and $0.5 (N)$: pre-tensioned case

5.2.2 AE non-linear response of the TPS surrounded by hypersonic flow

As highlighted, in order to validate and present the specific MB computational AE model, the square TPS specimen tested in the 8' High Temperature Tunnel (HTT) [59] has been chosen as reference. Figure 2.2.2 shows the TPS coupon mounted in the 8' HTT sled.

Table 5.2.2.1 shows Mach numbers and dynamic pressures experienced by the sample test in the 8' HTT as a function of the Angle of Attack (AoA). The tunnel run time is also limited to a maximum of 90 seconds, since the compressed air and liquid oxygen needed for a single run are stored in a bottle farm with a fixed capacity.

Angle of Attack (AoA)	Local Mach Number	Dynamic Pressure (Pa)
0	5.8	33094
2.5	5.6	46884
5	5.35	60763
7.5	5.1	74463
10	4.8	88252

Table 5.2.2.1 - Measured Mach number and dynamic pressure in the 8' HTT [59]

In the AE experiment carried out at NASA LaRC two tunnel tests have been conducted for the case with the three-layer TPS sample, labelled as #RUN22 and #RUN23, respectively. Only two AoA have been tested, the 2.5° and the 5° case. The difference between the two runs is how the angle of attack was changed in time. For the #RUN22, the tunnel was initially set at 5° for 5 seconds and 2.5° for 3 seconds. For #RUN23, the tunnel was initially set at 2.5° for 3 seconds and 5° for 5 seconds. This procedure was implemented to see if the response trends were path dependent.

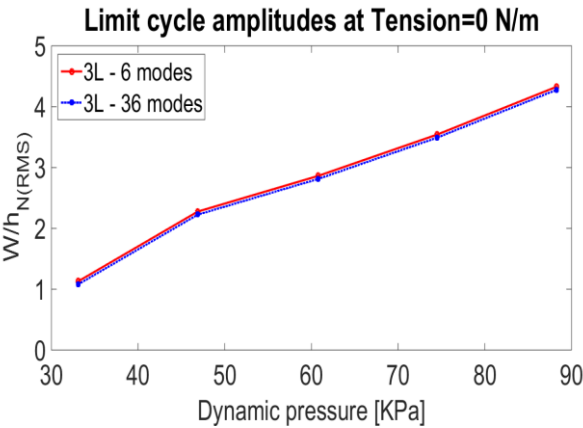
A stitching stiffness k^{St} of 50000 (Nm), a constant critical damping of 0.01 and a pre-tension of 525 (N/m) have been chosen for the computational model.

Since it is expected that the influence of the modes with the half-waves in the flow direction is greatest, and in order to reduce the computational time, 6 half-waves in the flow direction and 1 half-wave in the spanwise direction have been selected. In order to prove the validity of this assumption, an aero-elastic calculation taking into account 36 modes (6 spanwise and 6 stream-wise) has also been carried out, for the untensioned case.

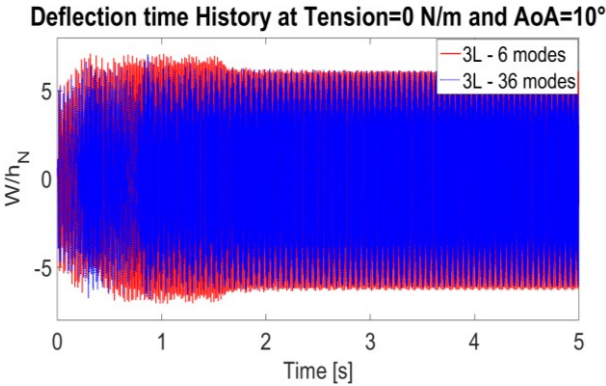
Deflection time histories at the accelerometer location near the trailing edge of the sample, located at $x/a, y/b = 0.8, 0.5$, as a function of flow Mach number and dynamic pressure summarized in Table 5.2.2.1 were computed using the non-linear numerical procedure previously outlined. Because of the solution is chaotic in time the Root Mean Square (RMS) amplitude has been used as a measure of deflection magnitude. Since the

objective of this simulation is to check the convergence of the solution, the simulation time has been set to 5 seconds.

Figure 5.2.2.1 shows that there is no difference in terms of $W/h_{N(RMS)}$ amplitudes between the simulation with 36 modes and the simulation with only 6 modes (a). Furthermore, a comparison of the deflection time histories for the critical case at an AoA of 10° has been shown (b).



(a)



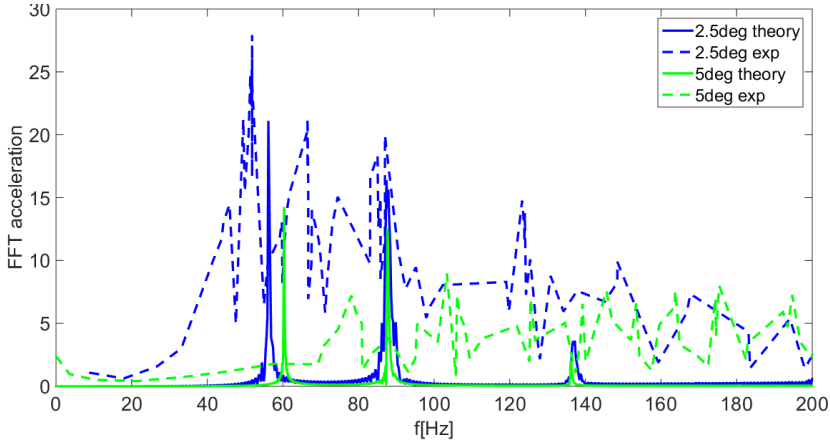
(b)

Figure 5.2.2.1 - Limit cycle amplitudes as a function of dynamic pressure untensioned (a) and deflection time history at $x/a, x/b=0.8,0.5, AoA=10^\circ$, untensioned (b)

Theoretical and experimental FFTs of the deflection time histories for the TPS sample and tunnel #RUN22 and #RUN23, are measured at the accelerometer location. Figure 5.2.2.2 shows the results for the theoretical and experimental frequency spectra. The MB theoretical

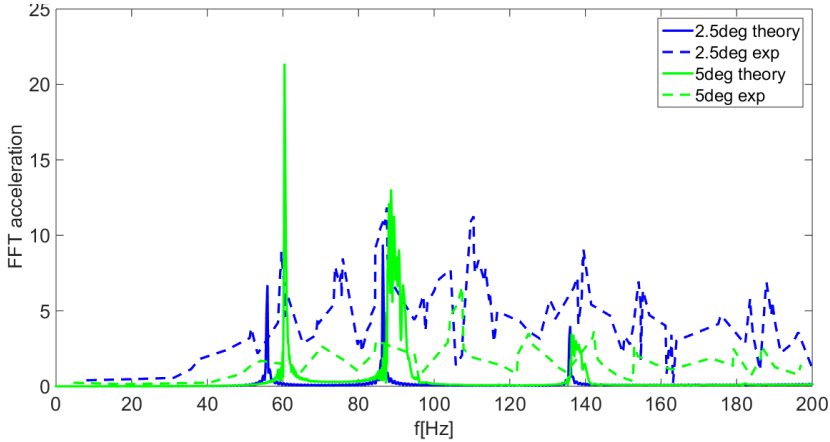
model reasonably predicts the peak frequency and amplitude for both runs. The small uncertainty of the results may be due to excitation sources neglected in the present computational model such as turbulent boundary layer fluctuations inside the wind tunnel, the initial condition chosen, and/or the structural damping. Despite these sources of uncertainty, the present result shows good agreement in terms of peak frequency and amplitude between theory and the experiment.

#RUN22



(a)

#RUN23



(b)

Figure 5.2.2.2 - Non-linear response comparison between experiment and theory for #RUN22 (a) and #RUN23 (b) at $x/a, x/b=0.8,0.5$

Furthermore, for both structural and thermal considerations, it may be required to increase the number of layers of the TPS. To this end, the AE behavior of three different situations, with different layer configurations, is investigated.

As done before, it is of interest to calculate the natural frequencies of the TPS using linear theory. As before, the plate nonlinearities are ignored for this purpose, neglecting the S^L terms of the Equation (3.4.13).

Three Test Cases (TCs) have been investigated: the three-layer (3L), the five-layer (5L) and the nine-layer (9L). For all the test cases, only the last layer is made of AKK, while the other layers are made of Nextel 440 BF-20; all of the layers are stitched together in a 5 cm square pattern.

This choice has been made in order to simulate a real case, in which it is important to limit heating on the backside of the sample and gas penetration during a test, or the atmospheric entry. As chosen for the validation of the 3L model, 6 half-waves on the flow field direction and 1 half-wave on the span wise direction has been selected for the computational model. A pretension of 525 (N/m) has also been set for each TC. The critical structural damping has been set to 0.01 and a stitching stiffness k^{St} of 50000 (Nm) has been chosen.

Natural frequencies for each TC have been summarized in Table 5.2.2.2.

Frequency	3L (Hz)		5L (Hz)		9L (Hz)	
	Untensioned	Pre-tensioned	Untensioned	Pre-tensioned	Untensioned	Pre-tensioned
f_{11}	17.97	48.85	18.55	46.75	18.86	45.54
f_{21}	44.93	84.71	45.37	82.18	47.16	80.73
f_{31}	89.85	135.61	92.75	133.45	94.31	132.23
f_{41}	152.7	202.18	157.62	201.29	160.3	200.79
f_{51}	233.38	285.32	240.94	286.52	245.04	287.19
f_{61}	331.74	385.53	342.53	389.58	348.36	391.8

Table 5.2.2.2 - Natural frequencies comparison

As expected, by increasing the number of layers for the untensioned case increases the natural frequency of each mode. Otherwise, by pre-tensioning the TPS, because of the increase of the thickness of the whole TPS, the natural frequencies of the first four modes tend to decrease but after the 4-th mode, the natural frequency increases.

Deflections time histories, at the accelerometer location, as a function of flow Mach number and dynamic pressure (summarized in Table 5.2.2.1), were computed using the non-

linear MB computational model. The simulation time (8 sec) has been set to enable an investigation of the steady state.

Figure 5.2.2.3 shows the deflection time history of the ratio W/h_N of the three different TCs in a particular condition, when the AoA is equal to 2.5° for the untensioned case. As shown, the deflections of the TCs 3L and 5L, after a short transient experience a non-linear vibrational phenomenon known as the Limit Cycle Oscillation (LCO). However the response of the TC 9L decays with the time. Furthermore, Figure 5.2.2.4 shows the deflection time history of the three different TCs when the AoA is equal to 10° . As shown in this case, all three TCs are experience LCO, with amplitudes higher than the case at 2.5° .

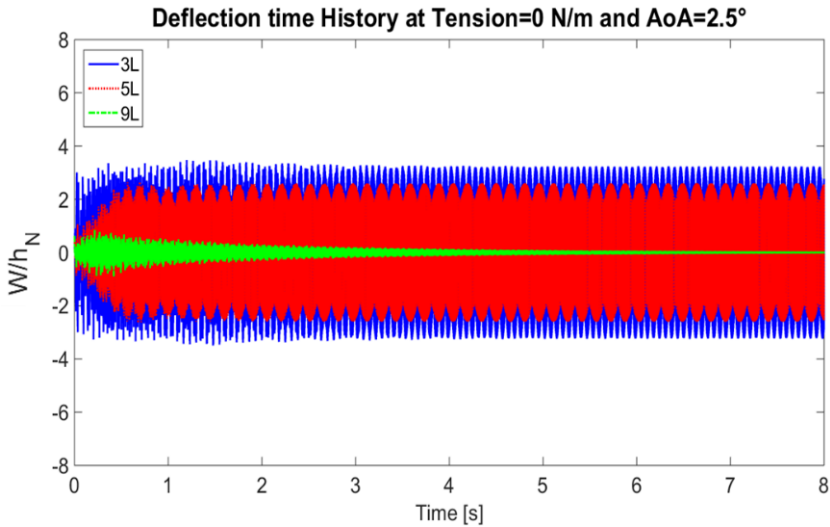


Figure 5.2.2.3 - Deflection time history comparison at $x/a, x/b=0.8,0.5, AoA=2.5^\circ$, untensioned

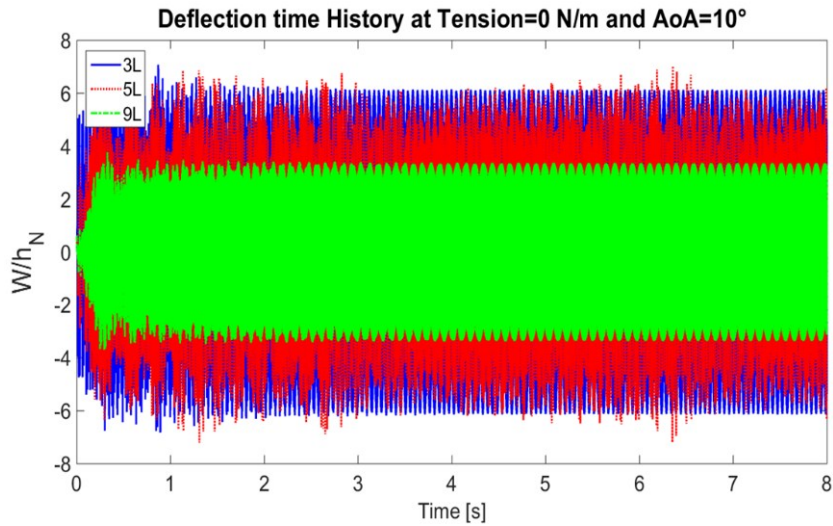


Figure 5.2.2.4 - Deflection time history comparison at $x/a, x/b=0.8,0.5$, $AoA=10^\circ$, untensioned

Figure 5.2.2.5 shows the deflection time history of the three TCs, at the accelerometer location, at the AoA equal to 10° for the pre-tensioned case. As shown, while the deflection amplitude of the TC 9L decays after a short transient, the deflection amplitudes of the TCs 3L and 5L seem to reach a constant value after a longer transient.

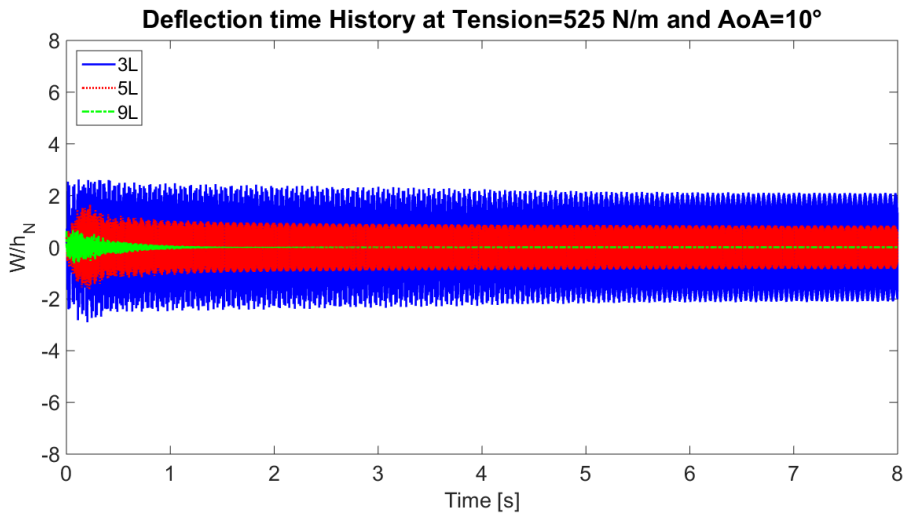
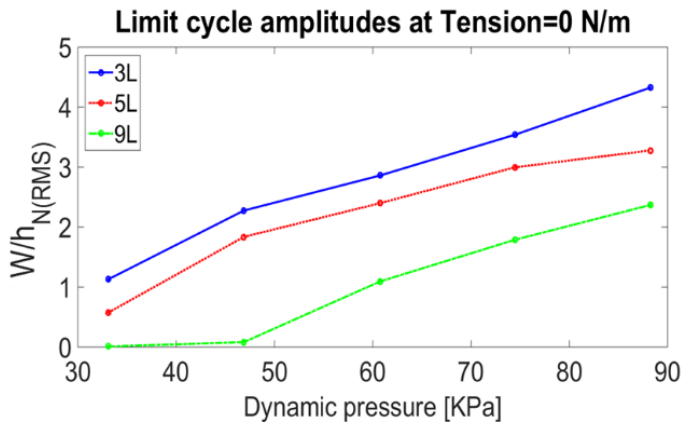


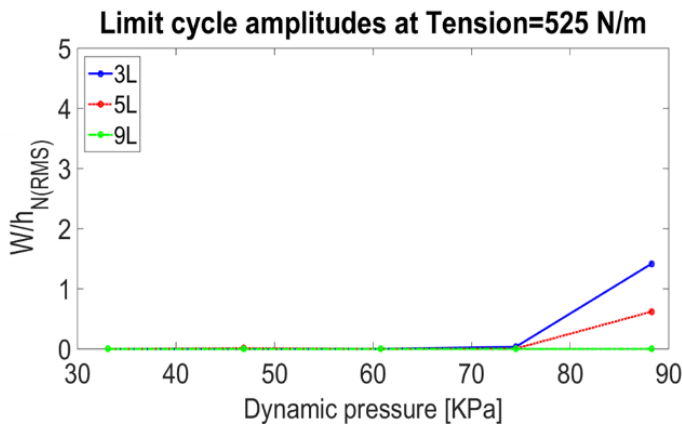
Figure 5.2.2.5 - Deflection time history comparison at $x/a, x/b=0.8,0.5$, $AoA=10^\circ$, pre-tensioned

Furthermore, a comparison among the deflection amplitudes of the three TCs at each AoA for the untensioned and pre-tensioned cases has been made.

Since the LCOs were chaotic in time, the RMS value of the ratio W/h_N was used. Figure 5.2.2.6 shows the $W/h_{N(RMS)}$ amplitudes, as a function of dynamic pressure for all the TCs, for the untensioned and the pre-tensioned case. As expected, by increasing the number of layers, for equal values of the dynamic pressure, the deflection amplitude tends to decrease for both the untensioned and pre-tensioned cases. Moreover, at an AoA equal to 2.5° the TC 9L is still stable, while the TCs 5L and the 3L are already in the LCO regime for the untensioned case.



(a)



(b)

Figure 5.2.2.6 - Limit cycle amplitudes as a function of dynamic pressure untensioned (a) and tensioned (b).

Thus, as shown, when including the pre-tensioning in the solution, the TC 9L is stable for all the flow conditions investigated, while the 5L and the 3L TC experience the LCO after 70 (*kPa*).

Finally, even if on one hand all the layers need to be perfectly bonded, on the other hand the weight of the stitch should be reduced in order to decrease the energy necessary for the launch. To this end, it is of interest to investigate the stitching density on the aero-elastic response of the TPS.

Four TCs have been taken into account: the nominal case with the spacing between stitching point of 5 cm (TC A); a second case with a gap between stitching point of 10 cm (TC B); a third case with a spacing between stitching point of 15 cm (TC C); and a fourth case with a single stitching point in the middle of the TPS (TC D) (see Figure 5.2.2.7).

Again, before calculating the aero-elastic response, the natural frequencies of the TPS using the eigenvalue extraction linear theory, neglecting the non-linear terms S^L in Equation (3.4.13), have been computed.

As was previously chosen for the validation of the 3L model, 6 half-waves in the flow direction and 1 half-wave in the spanwise direction, a value of the structural damping equal to 0.01, and a stitching stiffness k^{St} of 50000 (*Nm*) have been selected. Only the case with the pre-tension equal to 525 (*N/m*) has been studied for each TC. Natural frequencies for each TC have been summarized in Table 5.2.2.3.

Then, deflections time histories at the accelerometer location as a function of flow Mach number and dynamic pressure, as summarized in Table 5.2.2.1, were computed. The simulation time has been set again to 8 seconds. Figure 5.2.2.8 shows the $w/h_{N(RMS)}$ amplitudes, as a function of dynamic pressure for all the TCs. As shown, while the TCs A, B, and C seem to show a similar, nearly stable, response up to the AoA equal to 7.5° , for the case D the LCO occurs at an angle of attack equal to 2.5° .

Figures 5.2.2.9 and 5.2.2.10 show a comparison among the deflection time histories of the four different TCs, for the AoA equal to 2.5° and 5° , at 46 (*kPa*) and 60 (*kPa*) respectively. Since the transient is quite short, only the first 2 seconds have been depicted. As shown in Figure 5.2.2.9, all the TCs exhibit a stable behavior. However, when the AoA is equal to 5° , as shown in Figure 5.2.2.10, the deflections of the cases A, B and C tend to

decrease with time, while the TC-D presents a limit cycle behavior with a maximum RMS deflection w/h_N equal to 2.

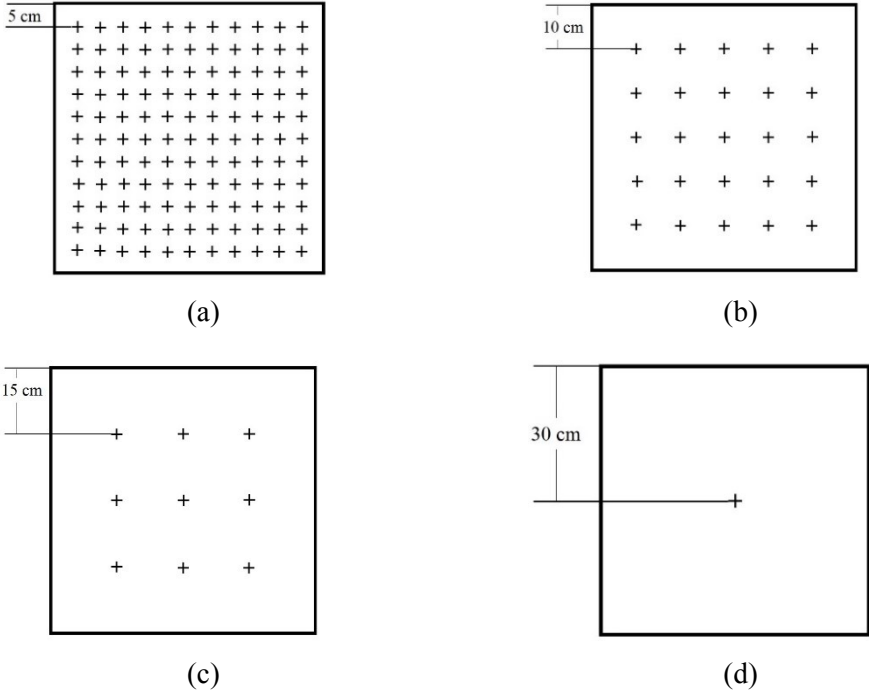


Figure 5.2.2.7 - Sketch of the four different stitching patterns: A (a), B (b), C (c), D (d)

Frequency [Hz]	5 cm (A)	10 cm (B)	15 cm (C)	30 cm (D)
	Pre-tension 525 N/m	Pre-tension 525 N/m	Pre-tension 525 N/m	Pre-tension 525 N/m
f_{11}	48.85	48.84	48.82	48.12
f_{21}	84.71	84.68	84.34	79.16
f_{31}	135.61	135.58	134.93	137.75
f_{41}	202.18	202.17	200.25	200.25
f_{51}	285.32	285.30	285.7	285.76
f_{61}	385.52	394.29	387.15	394.29

Table 5.2.2.3 - Natural frequencies

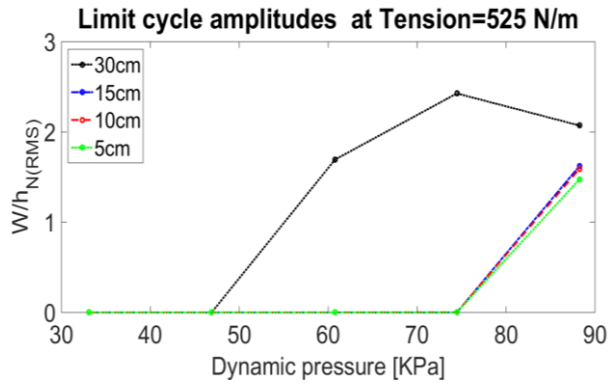


Figure 5.2.2.8 - Limit cycle amplitudes as a function of dynamic pressure: pre-tensioned.

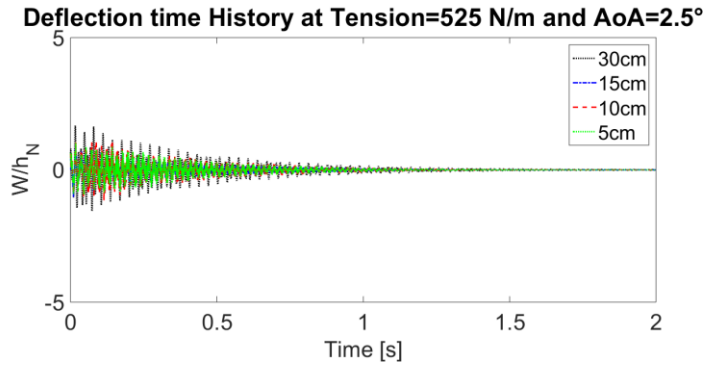


Figure 5.2.2.9 - Deflection time history comparison at $x/a, x/b=0.8,0.5$, $AoA=2.5^\circ$, pre-tensioned

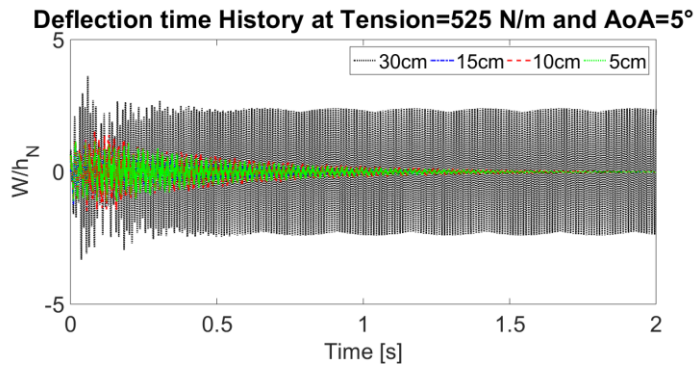


Figure 5.2.2.10 - Deflection time history comparison at $x/a, x/b=0.8,0.5$, $AoA=5^\circ$, pre-tensioned

6. Aero-Thermal (AT) and Structural (S) Analysis of a Deployable Capsule

In the present section, a preliminary analysis of the in-flight behavior of a deployable configuration in Low Earth Orbit (LEO) entry conditions has been presented.

The capsule with a flexible TPS in umbrella-like configuration presented by Iacovazzo, Carandente, Savino and Zuppardi [13] has been selected as reference; such configuration is depicted in Figure 6.1.

The present LEO re-entry demonstrator consists of a cylinder containing the payload and all the subsystems necessary for the mission, umbrella-like frame work, off-the-shelf ceramic fabrics for the conical deployable aero-brake and a light-weight, temperature-resistant material for the rigid hemispherical nose. When completely deployed, the aero-brake forms a half-cone angle of 45° and a maximum reference diameter of 900 (mm) is achieved.

The relevant flight characteristics have been evaluated by Iacovazzo, Carandente, Savino and Zuppardi [13] for this deployable capsule along a typical suborbital re-entry trajectory based on sounding rocket launch. In particular, two flight conditions of the trajectory computed in the aforementioned work have been considered, corresponding to the maximum heat flux and the maximum stagnation point pressure (see Table 6.1).

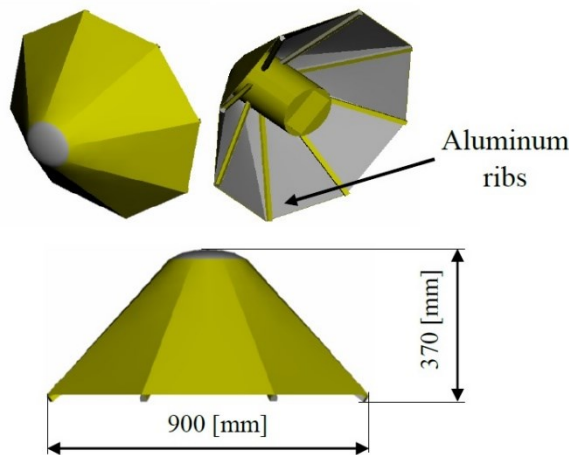


Figure 6.1 - Schematic configuration for a re-entry demonstrator to be testes on board REXUS rocket (half cone angle 45°) [13].

	Altitude (Km)	Velocity (m/s)	Mach
Max Heat Flux	47.5	840	2.5
Max stagnation point pressure	40	575	1.7

Table 6.1- Flight conditions at maximum heat flux and max stagnation pressure evaluated by Iacovazzo, Carandente, Savino and Zuppardi [13].

Fluid dynamic numerical simulations have been carried out with the *Cd-Adapco STAR-CCM+ v. 10* CFD software. Due to the LEO re-entry conditions selected, the flow field around the capsule is considered to be laminar, and the solver computes the steady three-dimensional flow field with a time implicit numerical scheme. The radiative model takes into account the emissivity of the fabric (0.443) and of the aluminum (0.1) and an ambient temperature of 270 (K) is considered to simulate radiative heat transfer between the capsule and the surrounding ambient. A constant wall static temperature of 270 (K) has been considered to evaluate cold wall heat fluxes.

Only a quarter of the volume has been meshed and modeled due to symmetry conditions. Referring to Figure 6.2, free stream conditions are imposed at the domain boundary labeled as 1, no-slip conditions for the velocity and radiative equilibrium at the capsule wall (labeled as 2), pressure outlet along downstream and side surfaces (labeled as 3).

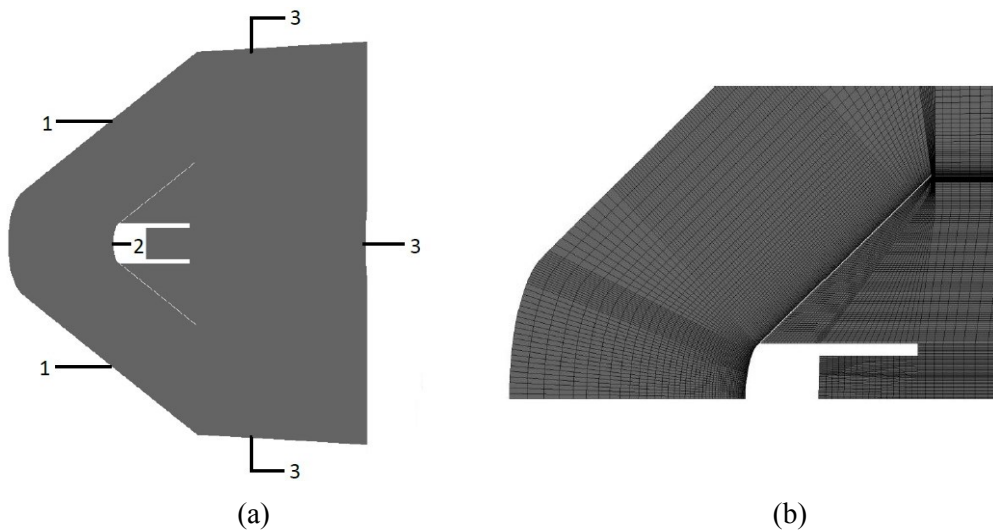


Figure 6.2 - Computing mesh for CFD analyses

Both conditions reported in Table 6.1 have been simulated. For the first condition, the Mach number is 2.5 at an altitude of 47 (Km). Relative CFD results, which include Mach number, pressure, and surface boundary heat flux, are summarized in Figure 6.3. Since radiative heat fluxes are not so relevant compared to the convective heat fluxes, because of the cold wall boundary condition imposed in the simulation, only convective heat flux is depicted.

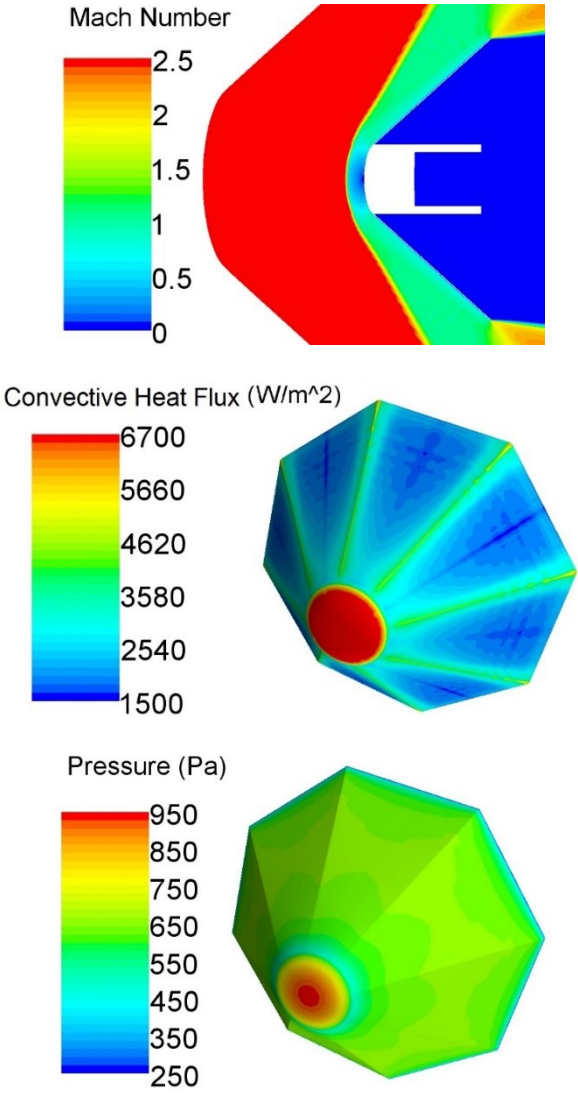


Figure 6.3 - Maximum heat flux condition CFD Results

For the case corresponding to max stagnation point pressure condition along the entry trajectory illustrated in Table 6.1, main results are shown in Figure 6.4. Values of heat flux and stagnation point pressure, computed with the above-mentioned conditions, are summarized in Table 6.2.

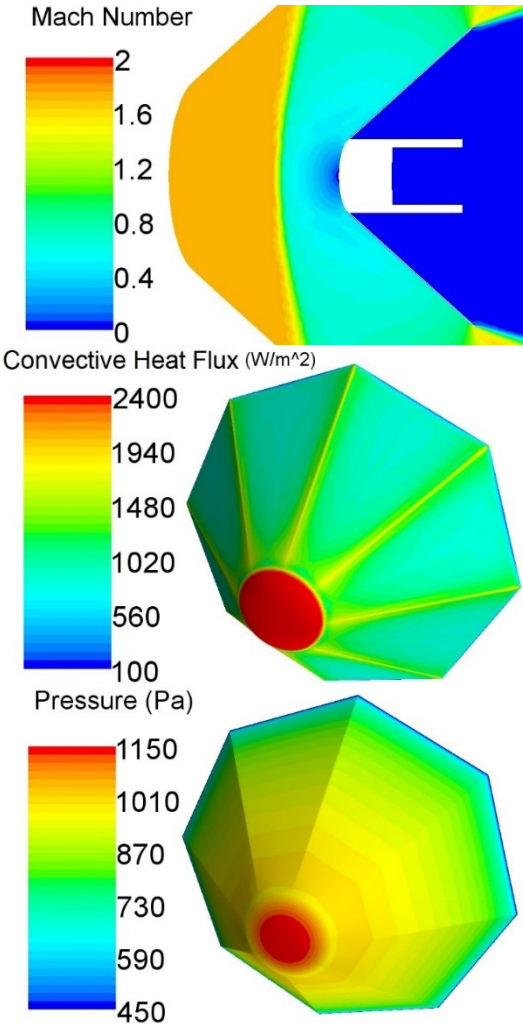


Figure 6.4 - Maximum stagnation point pressure condition CFD results

Preliminary aero-thermo-dynamic and structural analyses using the commercial software *Abaqus/Standard v 6.13* [43] for the structural domain and *Cd-Adapco STAR CCM+ v.10* [42] for the fluid domain have been performed.

First, the AT FSI loosely coupled approach discussed in Section 5.2 is preliminarily applied to investigate the AT behavior of the flexible deployable umbrella-like configuration along suborbital re-entry trajectory aforementioned.

	H (Km)	M	\dot{q}_0 (kW/m ²)	p_0 (kPa)
Max Heat Flux	47	2.5	6.7	0.95
Max stagnation point pressure	40	1.7	2.4	1.15

Table 6.2 – CFD results

Then, a preliminary assessment of the TPS structure has been made using a nonlinear FE simulation model of the flexible shield and of the main structural parts of the deployment mechanism, considering load conditions deriving from the entry phase (e.g. pressure loads).

6.1 Aero-Thermal analysis (AT)

In the present Section, a preliminary assessment of the AT behavior of the flexible deployable umbrella-like configuration along suborbital re-entry trajectory presented in Section 6 using a FSI one-way approach first, and a loosely coupled FSI approach then, has been performed. The heat transfer equations have been solved with *Abaqus/Standard v 6.13*. Due to symmetry conditions, only a quarter of the capsule has been modeled (see Figure 6.1.1). Two materials have been selected, aluminum alloy 7075-T6 for the capsule body and Nextel 440-BF20 for the TPS (the properties of materials are in Table 6.1.1). Numerical simulations have been performed in a three dimensional solid domain solving the energy equation with a coupled, time implicit numerical scheme.

Material	Thickness (mm)	Density (Kg/m³)	Conductivity (W/m·K)	Specific Heat (J/Kg·K)	Emissivity
Nextel 440- BF20	0.5	2700	0.15	1100	0.443
Aluminum Alloy 7075-T6	-	2700	237	880	0.1

Table 6.1.1 - Capsule thermal materials properties

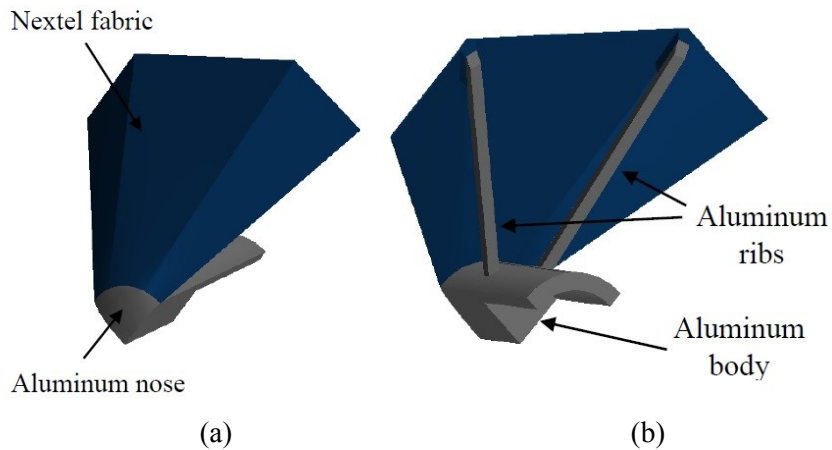
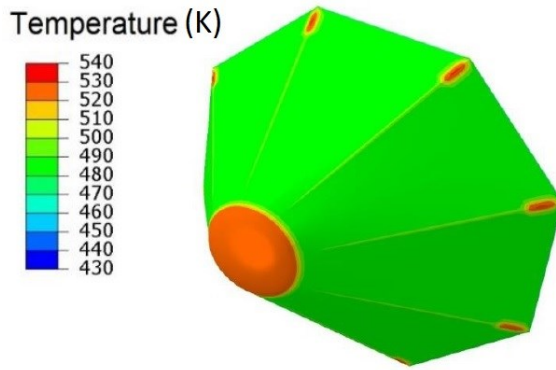
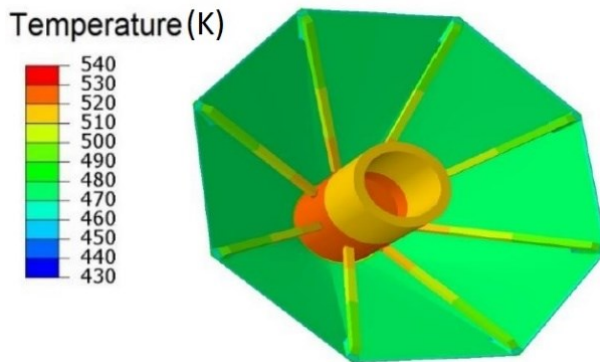


Figure 6.1.1 - Capsule model front (a) and back (b).

First, a one-way approach has been considered, applying the constant convective heat flux distribution obtained by maximum heat flux condition CFD simulation illustrated in Section 6, in order to evaluate temperature distribution, without considering the iteration of the process. Therefore, a constant heat flux distribution of $6700 \text{ (W/m}^2\text{)}$ for the nose, and $2400 \text{ (W/m}^2\text{)}$ for the texture, have been applied on the front surface of the capsule. The radiative model takes into account the emissivity of the fabric (0.443) and of the aluminium (0.1) and an ambient temperature of 270 (K) is considered to simulate radiative heat transfer between the capsule and the surrounding ambient. A four-layer fabric, made of Nextel 440-BF20, has been used for the TPS model. Temperature distribution results are shown in Figures 6.1.2 and 6.1.3.



(a)



(b)

Figure 6.1.2 - Temperature distribution front (a) and back (b)

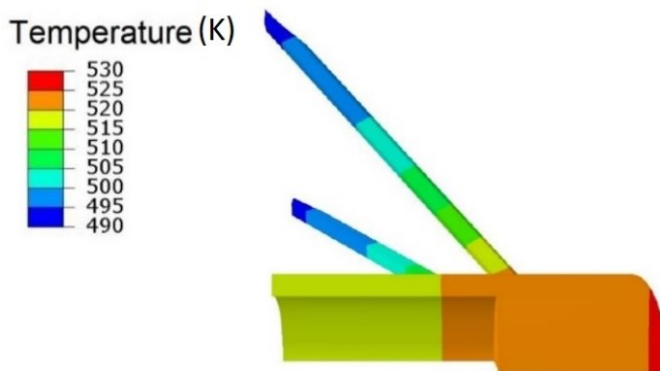


Figure 6.1.3 - Capsule body temperature distribution

Furthermore, in order to better predict the AT behavior of this deployable capsule, an aero-thermal coupling using the partitioned approach presented in Section 5.1 has been performed.

In this case, the mutual interaction between the fluid and the structure using the implicit staggered numerical scheme summarized in Figure 5.1.2 has been taken into account. This numerical scheme has been used to realize data transfer between the Fluid Dynamic solver *CD-Adapco STAR-CCM+ v.10* and the FE structural solver *Abaqus/Standard v 6.13*. In order to simulate a steady state condition a time step of 200 (s) and a maximum physical time of 60000 (s) have been set.

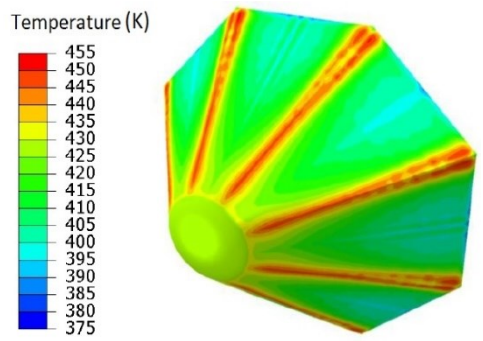
Only the maximum heat flux condition, reported in Table 6.1, has been simulated. As before, the radiation model that takes into account the emissivity of the fabric (0.443) and of the aluminum (0.1) and an ambient temperature of 270 (K) has been considered to simulate radiative heat transfer between the capsule and the surrounding ambient.

As shown in Figure 5.1.2, for each time step the boundary heat flux evaluated by the fluid solver is projected on the structural surface. Then, the FE solver calculates the temperature field and project it on the fluid domain. In an implicit time scheme, this transfer can occur more times per step, until convergence is reached.

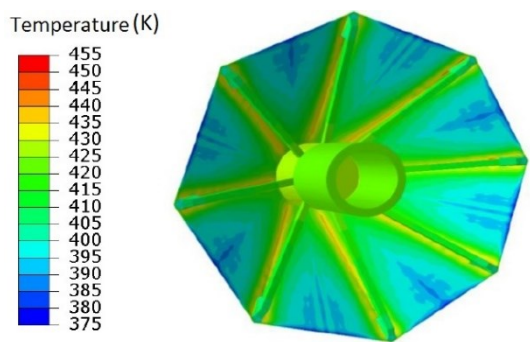
Figures 6.1.4 and 6.1.5 show temperature distribution results in Kelvin.

Comparing with Figures 6.1.2 and 6.1.3, the texture temperature remains nearly unchanged between the one-way approach and a loosely coupled approach. This is due to the low thickness and the low conductivity of the material selected for the fabric. On the contrary, looking at the temperature distribution of the capsule body, there is a slight difference in temperature profiles. This is due to the configuration and to the high conductivity of the aluminum.

Moreover, a maximum temperature of 428 (K) for the nose of the capsule and 455 (K) for the TPS fabric have been calculated, which are significantly below nominal maximum temperatures that aluminum and Nextel could tolerate, allowing use of off-the-shelves materials for a typical suborbital re-entry trajectory based on a sounding rocket launch mission.



(a)



(b)

Figure 6.1.4 - Temperature distribution front (a), and back (b)

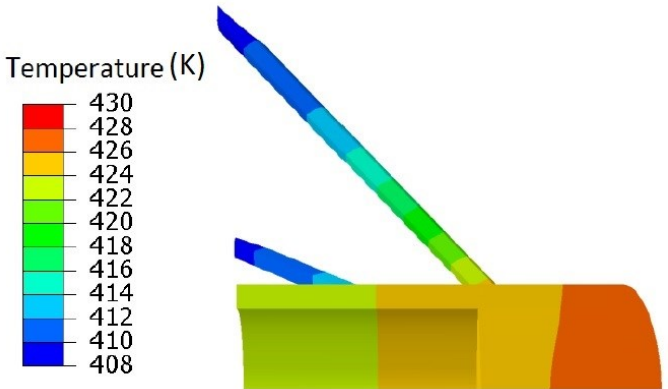


Figure 6.1.5 - Capsule body temperature distribution

6.2 Structural analysis (S)

The structural problem has been addressed with *Abaqus/Standard v 6.13* [43]. Since a geometrically non-linear behavior is expected for the load application case on the thin flexible TPS of the capsule, the Newton's method with the (NLGEOM) large-displacement formulation has been used. For the capsule geometry, the capsule configuration presented by Iacovazzo, Carandente, Savino and Zuppari [13] has been selected, corresponding to an octahedral shape held tensioned by 8 cylindrical ribs with a tube section of 1 (mm) thickness and an external radius of 7 (mm). A CAD model of this configuration is shown in Figure 6.1.

The materials chosen for the simulation are respectively a single layer of Nextel BF-20 for the flexible TPS and aluminum 7075-T6 for the central body and for the ribs (see Table 6.2.1). A single layer of Nextel of 0.5 (mm) of thickness has been used for the structural simulation. Since it has expected the use of more than one layer of Nextel, because of thermal considerations, this choice has been made in order to be conservative.

Moreover, in order to better simulate the fabric behavior, 4-node membrane M3D4R elements implemented in *Abaqus/Standard v 6.13* have been used for the simulation. A brief description of the model and elements used for the simulation is shown in Figure 6.2.1. For the sake of simplicity, only a slice of the capsule has been modeled and symmetry boundary conditions have been applied at symmetry plane location.

Material	Thickness (mm)	Density (Kg/m ³)	Young modulus (GPa)	Tensile Strength (Mpa)	Poisson's ratio
Nextel BF-20	0.5	2700	190	200	0.33
Aluminum 7075-T6	-	2700	70	540	0.33

Table 6.2.1 - Structural model material properties

According to the results obtained by CFD simulation (see Table 6.2), a constant value of the maximum pressure at stagnation point of 1.15 (kPa) has been applied on the texture. This has been done in order to evaluate the TPS static deflection at the maximum stagnation point pressure condition along the flight re-entry trajectory based on the supersonic sounding rocket (REXUS) considered by Iacovazzo, Carandente, Savino and Zuppari [13].

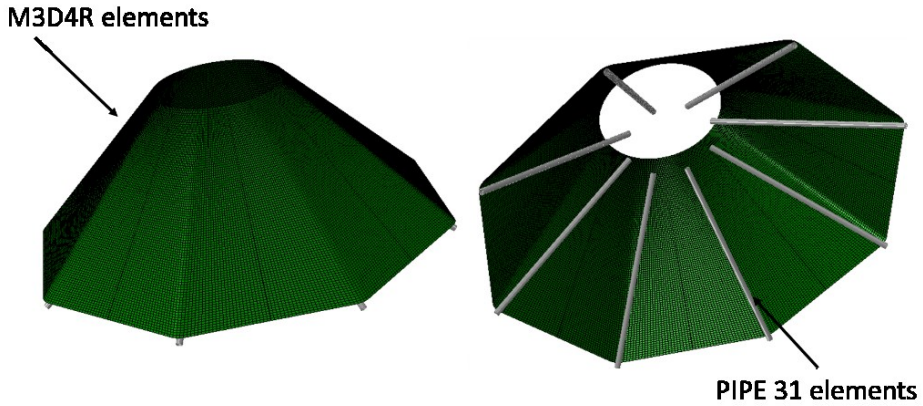


Figure 6.2.1 - Capsule FEM

Figure 6.2.2 shows the deflection magnitude results of the simulation. As can be seen, the maximum deflection is approximately 10 (*mm*).

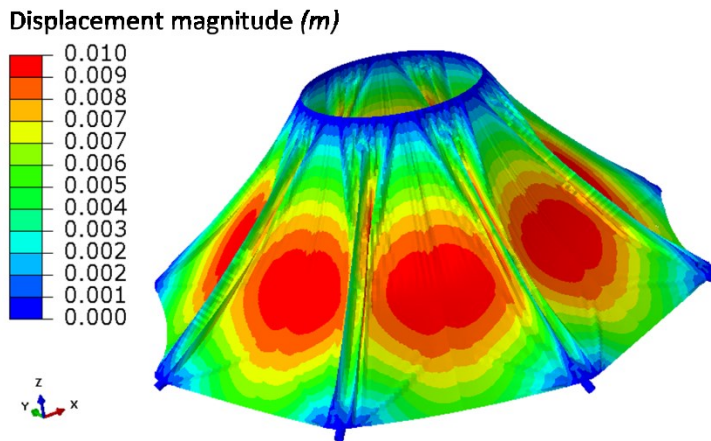


Figure 6.2.2 - TPS deflection magnitude contour

Figure 6.2.3 shows the stress distribution of the Nextel fabric during entry. As shown, the stress level is lower than the allowable limit (200 (*MPa*)); only in very small area, the maximum stress reaches a value of 184 (*MPa*) (see Figure 6.2.4).

The results below prove that this configuration can withstand the most critical dynamic load experienced during the atmospheric re-entry of the deployable capsule considered.

Von Mises stress (MPa)

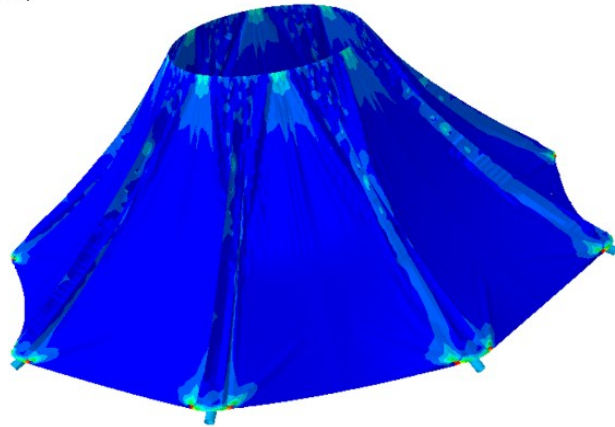
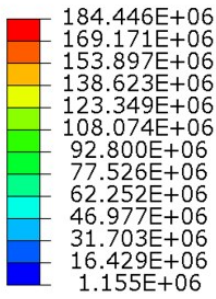


Figure 6.2.3 - TPS Von Mises stress contour

Von Mises stress (MPa)

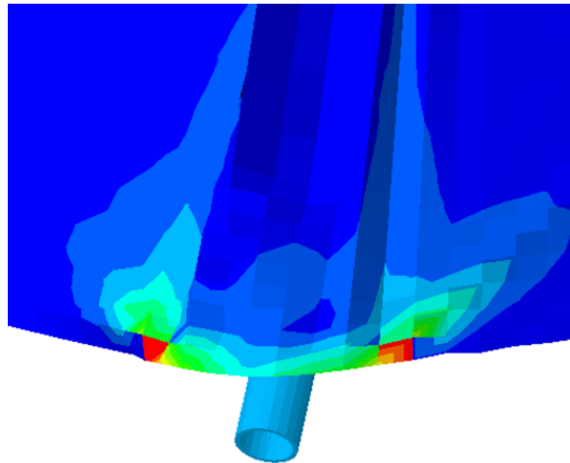
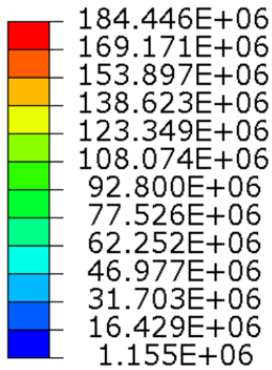


Figure 6.2.4 – TPS Von Mises stress contour (zoom)

7. **Conclusions and Future Work**

In a world where “reusable” and “cheap” represent the key words of the next future technologies, the need to develop new concepts, capable of reduce the costs and the complexity of planet exploration and Earth atmospheric entry systems, was the basis of this thesis work.

In this context, deployable “umbrella-like” configurations represent the future of atmospheric entry systems.

The purpose of this PhD thesis was to present a study on the suitable non-linear aero-thermo-dynamic and AE computational methodologies in order to investigate new flexible material configurations and innovative deployable capsule technology.

First, the use of a computational methodology to preliminary evaluate the main dynamic and thermal loads of a deployable capsule during the Mars atmospheric entry path has proven that such a configuration can improve the landing capabilities.

For the first time, a comparison among several actual Mars landers has proven that the thermal and dynamic loads on the deployable shield respect to a fixed shield configuration can be reduced by 2.5 to 3 times.

Furthermore, even if the correct evaluation of the heat flux in hypersonic flow remain a very hard task to accomplish, CFD results have proven that empiric tools such as Tauber/Sutton equations and the hypersonic Newton theory are valuable tools to predict the preliminary stagnation point heat flux and pressure of a blunt body in hypersonic flow field.

Then, non-linear AE and AT FSI computational methodologies, in order to evaluate several flexible materials configurations, have been investigated.

The FSI-AT study, which has been experimentally validated, has proven that a fully coupled approach, rather than the usual one-way approach, based on the interaction of the most advanced fluid dynamic and structural commercial software provides the most accurate results in terms of temperature prediction across the TPS thickness.

Then, a computational tool based on the natural modes of the structure, which evaluates the non-linear AE behavior of a flexible TPS surrounded by hypersonic flow, has been developed.

The non-linear AE model was previously successfully validated using experimental results and a FEM of the TPS specimen tested at NASA LaRC in Virginia.

The simple, but quite accurate, formulation of such a non-linear model makes it a flexible tool capable of investigating several material configurations in a short amount of time. This can considerably reduce the design costs, giving the possibility to study a wide range of material configurations and flow conditions before the experimental tests.

Finally, a study of a preliminary AT and structural assessment of a deployable capsule in LEO hypersonic flow conditions using a FSI-AT approach and a FE model has been presented. These studies have provided a comprehensive analysis of the structure response to thermal and dynamic loads encountered during the entry phase from a LEO trajectory of a deployable capsule. This work has proven that the “umbrella-like” configuration can withstand the most critical dynamic load experienced during a hypersonic atmospheric re-entry.

In conclusion, the computational methodologies presented, not only have demonstrated the feasibility of investigating and reducing the costs of the AT and AE preliminary assessment of a flexible shield in hypersonic conditions; but this work opens the way to several further studies such as:

- The effect of different stitching shapes among TPS layers.
- The introduction of the temperature influence on the AE response.
- A more accurate aerodynamic theory like the third order PT or even a CFD aerodynamic model on the LCO behavior of the MB model.
- The development of a more accurate FE and CFD model of a deployable capsule in order to evaluate the AE-FSI behavior of such a configuration in hypersonic flow conditions.

Appendix I

The equations of motion of the nonlinear-coupled system shown in Equation (3.4.13) are given in this section. The equations have been vectorized in a manner such that the systems of ODEs can be solved without loops involving the modal coordinates.

The coefficient matrices in the following equations involve integrals of the mode shape functions. The simply-supported mode shape function for a given mode number n is an $r_x \times r_y$ matrix defined as:

$$\phi_n = \phi_{nm}(x, y) = \sin(n\pi\xi) \otimes \sin(m\pi\eta) \quad (\text{I})$$

Where $\xi = x/a$, $\eta = y/b$, and r_x and r_y are the number of discrete points in the numerical discretization of the mode shape, in the x and y directions respectively. The symbol \otimes is the vector outer product [59]. Note that the n^{th} stream-wise mode and the m^{th} span-wise mode are specified by a single modal index n , and a numerical algorithm generates the correct modal indexing for both directions. While ϕ_n is a matrix, the data structure Φ is a third order tensor comprised of mode shapes $1 \dots N$, where N is the total number of modes. Thus Φ has dimensions $r_x \times r_y \times N$.

The square of the mode shape tensor is computed using the element-wise Schur product in three dimensions, known by the symbol \circ [59].

The diagonal mass matrix is

$$M_{nn}^L = \text{mass}^L \int_0^1 \int_0^1 \Phi \circ \Phi d\xi d\eta \quad (\text{II})$$

where mass^L represent the plate mass per area.

The diagonal bending stiffness matrix is

$$B_{nn}^L = D^L \int_0^1 \int_0^1 \left\{ \frac{1}{a^4} \frac{\partial^2 \Phi}{\partial \xi^2} \circ \frac{\partial^2 \Phi}{\partial \xi^2} + \frac{1}{b^4} \frac{\partial^2 \Phi}{\partial \eta^2} \circ \frac{\partial^2 \Phi}{\partial \eta^2} + \frac{2\nu^L}{(ab)^2} \frac{\partial^2 \Phi}{\partial \xi^2} \circ \frac{\partial^2 \Phi}{\partial \eta^2} \right. \\ \left. + \frac{2(1-\nu)}{(ab)^2} \frac{\partial^2 \Phi}{\partial \xi \partial \eta} \circ \frac{\partial^2 \Phi}{\partial \xi \partial \eta} \right\} d\xi d\eta + \frac{N_x^A}{a^2} \int_0^1 \int_0^1 \frac{\partial \Phi}{\partial \xi} \circ \frac{\partial \Phi}{\partial \xi} d\xi d\eta \\ + \frac{N_y^A}{2} \int_0^1 \int_0^1 \frac{\partial \Phi}{\partial \eta} \circ \frac{\partial \Phi}{\partial \eta} d\xi d\eta \quad (III)$$

Then the coefficient matrix for the spring stitching is

$$I_{ni}^L = k^{St} \sum_j \phi_n(\xi = \xi_j, \eta = \eta_j) \phi_i(\xi = \xi_j, \eta = \eta_j) \quad (IV)$$

where the summation over index j refers to the individual point stitches in the system.

The fully populated aerodynamic stiffness and diagonal aerodynamic damping matrices are given by

$$A_{ni} = \frac{2 \cdot q}{a \cdot Mach} \int_0^1 \int_0^1 \frac{\phi_i}{\partial \xi} \circ \phi_n d\xi d\eta \quad (V)$$

$$Z_{nn}^{L1} = \rho_\infty c_\infty \int_0^1 \int_0^1 \Phi \circ \Phi d\xi d\eta \quad (VI)$$

where q is the dynamic pressure, ρ_∞ is the asymptotic atmospheric pressure and c_∞ represent the asymptotic speed of sound.

The stretching energy vector is a nonlinear function of the modal coordinate and is given by

$$S = \text{sum} \{ \Gamma_{nijos} \mid s = 1, \dots, N ; j = 1, \dots, N ; i = 1, \dots, N \} \text{ for } n = 1, \dots, N \quad (VII)$$

with

$$\Gamma = \left((\vec{a} \otimes \vec{a}) \otimes (\vec{1} \otimes \vec{a}) \right) \circ \Omega \quad (VIII)$$

where $\vec{1}$ is a vector of ones the same length as the deflection modal coordinate vector.

The sum operation indicates summation of the specified tensorial dimensions and subsequent reduction in tensor order, or “tensorial collapsing.” The dimensions to be collapsed here are the fourth, third, and second dimensions, indicated by i , j , and k , respectively. Note that the elementwise Schur product now acts in four dimensions. The fourth-order tensor coefficient Ω for the n^{th} mode is defined by

$$\Omega_{n i j s} = \sum_k \frac{1}{2Eh} \left(\frac{a}{b}\right)^4 R_k C_k^2 \{ \alpha_{n i k} \alpha_{j s k} + \alpha_{i n k} \alpha_{j s k} + \alpha_{j i k} \alpha_{n s k} + \alpha_{s i k} \alpha_{j n k} \} \quad (\text{IX})$$

with

$$R_k = \int_0^1 \int_0^1 \left\{ \frac{1}{a^4} \frac{\partial^2 \Phi}{\partial \xi^2} \circ \frac{\partial^2 \Phi}{\partial \xi^2} + \frac{1}{b^4} \frac{\partial^2 \Phi}{\partial \eta^2} \circ \frac{\partial^2 \Phi}{\partial \eta^2} - \frac{2\nu^L}{(ab)^2} \frac{\partial^2 \Phi}{\partial \xi^2} \circ \frac{\partial^2 \Phi}{\partial \eta^2} + \frac{2(1+\nu)}{(ab)^2} \frac{\partial^2 \Phi}{\partial \xi \partial \eta} \circ \frac{\partial^2 \Phi}{\partial \xi \partial \eta} \right\} d\xi d\eta \quad (\text{X})$$

$$C_k = \frac{Eh}{\int_0^1 \int_0^1 \left\{ \frac{\partial^4 \Phi}{\partial \xi^4} \circ \Phi + \left(\frac{a}{b}\right)^4 \frac{\partial^4 \Phi}{\partial \eta^4} \circ \Phi + 2 \left(\frac{a}{b}\right)^2 \frac{\partial^2 \Phi}{\partial \xi^2} \circ \frac{\partial^2 \Phi}{\partial \eta^2} \right\} d\xi d\eta} \quad (\text{XI})$$

$$\alpha_{n i k} = \beta_{n i k} - \gamma_{n i k} \quad (\text{XII})$$

where

$$\beta_{n i k} = \int_0^1 \int_0^1 \frac{\partial \phi_n}{\partial \xi \partial \eta} \circ \frac{\partial \phi_i}{\partial \xi \partial \eta} \circ \phi_k d\xi d\eta; \quad \gamma_{n i k} = \int_0^1 \int_0^1 \frac{\partial^2 \phi_n}{\partial \xi^2} \circ \frac{\partial^2 \phi_i}{\partial \eta^2} \circ \phi_k d\xi d\eta \quad (\text{XIII})$$

Numerical solutions are obtained using the fourth-order Runge–Kutta scheme in MATLAB.

References

- [1] R. Bisplinghoff and J. Dugundji, "Influence of Aerodynamic Heating on Aeroelastic Phenomena," *Pergamon Press*, pp. 288–312, 1958.
- [2] D. Akin, "The parashield entry vehicle concept: basic theory and flight-test developments," *Proceedings of the 4th Annual AIAA/Utah State University Conference on Small Satellites, Logan, UT, August 27–30, 1990*.
- [3] D. Wilde and S. Walther, "Inflatable Re-entry and Descent Technology (IRDT)—further developments," *Proceedings of the 2nd International Symposium of Atmospheric Re-entry Vehicles and Systems, Arcachon, France*.
- [4] S. Hughes, R. Dillman, B. Starr, R. Stephan, M. Lindell, C. Player and F. Cheatwood, "Inflatable Re-entry Vehicle Experiment (IRVE) Design Overview," *18th AIAA Aerodynamic Decelerator Systems Technology Conference and Seminar, Munich, Germany, May 24-26, 2005*.
- [5] B. Goldman, E. Dowell and R. Scott, "Aeroelastic stability of thermal protection system for inflatable aerodynamic decelerator," *Aeroelastic stability of thermal protection system for inflatable aerodynamic decelerator, Journal of Spacecraft and Rockets*, vol. 52, no. 1, pp. 144-156., 2015.
- [6] D. Litton, D. Bose, F. Cheatwood, S. Hughes, H. Wright, M. Lindell, S. Derry and A. Olds, "Inflatable Re-Entry Vehicle Experiment (IRVE) - 4 overview," *21st AIAA Aerodynamic Decelerator Systems Technology Conference and Seminar*, 2011.
- [7] V. Carandente, "Aerothermodynamic and mission analyses of deployable aerobraking Earth re-entry systems", PhD Thesis, 2014.
- [8] V. Carandente and R. Savino, "New concepts of deployable de-orbit and re-entry systems for CubeSat miniaturized satellites," *Recent Pat. Eng.* 8 2–12, 2014.
- [9] V. Carandente, G. Elia and R. Savino, "Conceptual design of de-orbit and re-entry modules for standard CubeSats," *Proceedings of the 2nd IAA Conference on University Satellite Missions and Cubesat Work-shop, Rome, February 4–7, 2013*.
- [10] V. Carandente, R. Savino, M. Iacovazzo and C. Boffa, "Aerothermal analysis of a sample-return reentry capsule," *Fluid Dynamics and Materials Processing*, vol. 9, no. 4, pp. 461-484, 2013.
- [11] R. Savino and V. Carandente, "Aerothermodynamic and feasibility study of a deployable aero-braking re-entry capsule," *Fluid Dyn. Mater. Process.* 8 (4) 453–477, 2012.
- [12] R. Savino, R. Aurigemma, V. Carandente, P. Dell'Aversana, L. Gramiccia, J. Longo, L. Marraffa and F. Punzo, "Study and development of a sub-orbital reentry demonstrator," *Proceedings of the Italian Association of Aeronautics and Astronautics XXII Conference, Naples, Italy, September 9-12, 2013*.

- [13] M. Iacovazzo, V. Carandente, R. Savino and G. Zuppardi, "Longitudinal stability analysis of a suborbital re-entry demonstrator for a deployable capsule," *Acta Astronautica*, vol. 106, pp. 101-110, 2015.
- [14] R. Braun and R. Manning, "Mars Exploration Entry, Descent, and Landng Challenges," *Journal of Spacecraft and Rockets* 44 310-323, 2007.
- [15] K. Edquist, P. Desai and M. Schoenenberger, "Aerodynamics for the Mars Phoenix Entry Capsule," *Journal of Spacecraft and Rockets* 713-726., 2011.
- [16] J. Cruz and J. Lingard, "Aerodynamic Decelerators for Planetary Exploration: Past, Present, and Future," *AIAA Guidance, Navigation, and Control Conference and Exhibit, Guidance, Navigation, and Control and Co-located Conferences*, Colorado, Keystone, 2006.
- [17] B. Raiszadeh, D. Desai and R. Michelltree, "Mars Exploration Rover Heat Shield Recontact Analysis," *21st AIAA Aerodynamic Decelerator Systems Technology Conference and Seminar, Aerodynamic Decelerator Systems Technology Conferences*, 2011.
- [18] I. Clark, A. Hutchings, C. Tanner and R. Braun, "Supersonic inflatable aerodynamic decelerators for use on future robotic missions to Mars," *Journal of Spacecraft and Rockets* 46 (2) 340–352, 2009.
- [19] R. Rohrschneider and R. Braun, "Static aeroelastic analysis of thin-film clamped ballute for titan aerocapture," *Journal of Spacecraft and Rockets* 45 (4) 785–801, 2008.
- [20] D. Lyons and W. Johnson, "Ballute aerocapture trajectories at Neptune," *AIAA Atmospheric Flight Mechanics Conference and Exhibit*, no. AIAA 2004-5181, Providence, RI, USA, 2004.
- [21] P. Pasolini, R. Aurigemma, F. Causa, N. Cimminiello, D. De La Torre Sangrà, P. Dell'Aversana, F. Esposito, E. Fantino, L. Gramiccia, M. Grassi, G. Lanzante, C. Molfese, F. Punzo, I. Roma, R. Savino and G. Zuppardi, "SMALL MARS SATELLITE: a low cost system for Mars exploration," *Proceedings of the 67th International Astronautical Congress, Guadalajara, Mexico*, 2016.
- [22] E. Bassano, R. Savino, R. Lo Forti, A. Ferrarotti, C. Richiello, G. Russo, R. Aurigemma, F. Punzo and P. Dell'Aversana, "IRENE – Italian Re-Entry NacellE for Microgravity Experiments," *Proceedings of the 62nd International Astronautical Congress, CapeTown, October3–7, IAC-11.A2.7.7*, 2011.
- [23] E. Fantino, R. Aurigemma, F. Causa, N. Cimminiello, D. De La Torre, P. Dell'Aversana, F. Esposito, L. Gramiccia, M. Grassi, C. Molfese, P. Pasolini, F. Paudice, F. Punzo, R. Savino and G. Zuppardi, "THE SMALL MARS SATELLITE: A EUROPEAN SMALL-SIZE MARS LANDER," *7th Internetal Conference on Systems & Concurrent Engineering for Space Applications, Madrid*, 2016.
- [24] B. Smith, C. Tanner, M. Mahzari, I. Clark, R. Braun and F. Cheatwood, "A Historical Review of Inflatable Aerodynamic Decelerator Technology Development," *IEEEAC 1267, 2010 IEEE Aerospace Conference, Big Sky, MT*, 2010.

- [25] J. McNamara and P. Friedmann, "Aeroelastic and aerothermoelastic analysis of Hypersonic vehicles: Current status and future trends," *Collection of Technical Papers - AIAA/ASME/ASCE/AHS/ASC Structures, Structural Dynamics and Materials Conference*, pp. 3814, 2007.
- [26] J. McNamara and P. Friendmann, "Aeroelastic and aerothermoelastic analysis in hypersonic flows: past, present, and future," *AIAA Journal* 49 (6) 1089–1122, 2011.
- [27] A. Culler and J. McNamara, "Studies on fluid-thermal-structural coupling for aerothermoelasticity in hypersonic flow," *AIAA Journal*, vol. 48, no. 8, pp. 1721-1738, 2010.
- [28] M. Lightill, "Oscillating Airfoils at High Mach Numbers," *Journal of the Aeronautical Sciences*, Vol. 20, No. 6, 1953.
- [29] E. Dowell, *Aeroelasticity of plates and shells*, 1975.
- [30] J. McNamara, P. Friedmann, K. Powell, B. Thuruthimattam and R. Bartels, "Three-dimensional Aeroelastic and Aerothermoelastic Behavior in Hypersonic Flow," *AIAA-2005-2175, 46th AIAA/ASME/ASCE/AHS/ASC Structures, Structural Dynamics and Materials Conference*, Austin, Texas, Apr. 18-21, 2005.
- [31] E. Livne, "Future of Airplane Aeroelasticity," *Journal of Aircraft*, Vol. 40, No. 6, pp. 1066-1092, 2003.
- [32] E. Livne and T. Weisshaar, "Aeroelasticity of Nonconventional Airplane Configurations-Past and Future," *Journal of Aircraft*, Vol. 40, No. 6, pp. 1047-1065, 2003.
- [33] K. Hall, J. Thomas and E. Dowell, "Proper Orthogonal Decomposition Technique for Transonic Unsteady Aerodynamic Flows," *AIAA Journal*, Vol. 38, No. 10, pp. 1853–1862., 2000.
- [34] D. Lucia, P. Beran and W. Silva, "Reduced Order Modeling: New Approaches for Computational Physics," *Progress in Aerospace Sciences*, Vol. 40, Nos. 1–2, pp. 51–117., 2004.
- [35] E. Dowell and K. Hall, "Modeling of fluid–structure Interaction," *Annual Review of Fluid Mechanics*, Vol. 33, pp. 445–490., 2001.
- [36] P. Trizila, C. Kang, M. Visbal and W. Shyy, "A Surrogate Model Approach in 2D Versus 3D Flapping Wing Aerodynamic Analysis," *AIAA Paper 2008-5914*, 2008.
- [37] B. Glaz, L. Liu and P. Friedmann, "Reduced-Order Nonlinear Unsteady Aerodynamic Modeling Using a Surrogate-Based Recurrence Framework," *AIAA Journal*, Vol. 48, No. 10, pp. 2418–2429., 2010.
- [38] B. Glaz, L. Liu, P. Friedmann, J. Bain and L. Sankar, "A Surrogate Based Approach to Reduced-Order Dynamic Stall Modeling," *AIAA Paper 2010-3042.*, 2010.
- [39] G. Guruswamy, "A review of numerical fluids/structures interface methods for computations using high-fidelity equations," *Comput Struct*, 80:31–41., 2002.

- [40] R. Kamakoti and Shyy, "Fluid–structure Interaction for Aeroelastic Applications," *Progress in Aerospace Sciences, Vol. 40, No. 8, pp. 535–558.*, 2004.
- [41] C. Farhat, K. van der Zee and P. Geuzaine, "Provably second-order time-accurate loosely-coupled solution algorithms for transient nonlinear computational aeroelasticity," *Computer Methods in Applied Mechanics and Engineering 195(17):1973-2001*, 2006.
- [42] *Cd-AdapcoSTAR-CCM+, Cd-AdapcoSTAR-CCM+ v10 User's Guide, Cd-Adapco STAR CCM+ Inc.*.
- [43] *ABAQUS, ABAQUS v 6.13 User's Guide, SIMULIA ABAQUS Inc.*
- [44] C. Mei, K. Abdel-Motagaly and R. Chen, "Review of Nonlinear Panel Flutter at Supersonic and Hypersonic Speeds," *Applied Mechanics Reviews, Vol. 52, No. 10*, 1999.
- [45] E. Dowell, "Panel Flutter: A review of Aeroelastic stability of Plates and Shells," *AIAA Journal, Vol. 8, No. 3*, 1970.
- [46] Eugeni, M., Mastroddi, F. and Dowell, E.H., "Normal form analysis of a forced aeroelastic plate," *Journal of sound and vibration, volume 390, pag. 141-163*, 2017.
- [47] J. Spriggs, A. Messiter and W. Anderson, "Membrane flutter paradox-An explanation by Singular Perturbation Methods," *AIAA Journal, Vol. 7, No. 9*, 1969.
- [48] D. Johns, "Supersonic Membrane Flutter," *AIAA Journal, Vol. 9, No. 5*, 1971.
- [49] R. Scott, R. Bartels and O. Kandil, "An aeroelastic analysis of a thin flexible membrane," *48th AIAA/ASME/ASCE/AHS/ASC Structures, Structural Dynamics, and Materials Conference*, 2007.
- [50] C. Ellen, "Approximate solution of the membrane flutter problem," *AIAA Journal, Vol. 3, No. 6*, 1965.
- [51] K. Yamada, K. Suzuki and M. Hongoh, "Aerodynamic characteristics of three-dimensional membrane aeroshells in supersonic flow," *21st applied aerodynamics conference, no. AIAA 2003-3924, Orlando*, 2003.
- [52] P. Anderson, "Computational continuum and rarefied flow results for ballute applications," *42nd AIAA Aerospace Sciences Meeting and Exhibit, No. AIAA 2004-292, Reno*, 2004.
- [53] R. Kramer, F. Cirak and C. Pantano, "Fluid–Structure Interaction Simulations of a Tension-Cone Inflatable Aerodynamic Decelerator," *AIAA Journal, Vol. 51, No. 7, pp. 1640-1656*, 2013.
- [54] R. Rohrschneider, "Variable-fidelity hypersonic aeroelastic analysis of thin-film ballutes for aerocapture," *PhD thesis at Georgia Institute of Technology*, 2007.
- [55] Z. Wang, S. Yang, D. Liu, X. Wang, M. Mignolet and R. Bartels, "Nonlinear aeroelastic analysis for a wrinkling aeroshell/ballute system," *Collection of Technical Papers - AIAA/ASME/ASCE/AHS/ASC Structures, Structural Dynamics and Materials Conference*, 2010.

- [56] B. Goldman, E. Dowell and R. Scott, "Flutter Analysis of the Thermal Protection Layer on the NASA HIAD," *22nd AIAA Aerodynamic Decelerator Systems (ADS) Conference*, 2013.
- [57] B. Goldman, E. Dowell and R. Scott, "In-Flight Aeroelastic Stability of the Thermal Protection System on the NASA HIAD, Part I: Linear Theory," *55th AIAA/ASME/ASCE/AHS/SC Structures, Structural Dynamics, and Materials Conference*, 2014.
- [58] B. Goldman, E. Dowell and R. Scott, "In-Flight Aeroelastic Stability of the Thermal Protection System on the NASA HIAD, Part II: Nonlinear Theory and Extended Aerodynamics," *56th AIAA/ASCE/AHS/ASC Structures, Structural Dynamics, and Materials Conference, Florida*, 2015.
- [59] B. Goldman, R. Scott and E. Dowell, "Nonlinear Aeroelastic Analysis of the HIAD TPS Coupon in the NASA 8' High Temperature Tunnel: Theory and Experiment," *NASA TM-2014-218267*, 2014.
- [60] B. Goldman and E. Dowell, "Nonlinear Oscillations of a Fluttering Plate Resting on a Unidirectional Elastic Foundation," *AIAA Journal, Vol. 52, No. 10, pp. 2364-2368*, 2014.
- [61] G. Buck, "Testing of Flexible Ballutes in Hypersonic Wind Tunnels for Planetary Aerocapture," *44th American Institute of Aeronautics and Astronautics (AIAA) Aerospace Sciences Meeting and Exhibit; Reno, NV; United States*, 2006.
- [62] I. Clark, J. Cruz, M. Hughes, J. Ware, A. Madlangbayan and R. Braun, "Aerodynamic and Aeroelastic Characteristics of a Tension Cone Inflatable Aerodynamic Decelerator," *20th AIAA Aerodynamic Decelerator Systems Technology Conference and Seminar*, 2009.
- [63] R. Dillman, S. Hughes, R. Bodkin, D. Bose, J. Del Corso and F. Cheatwood, "Flight Performance of the Inflatable Reentry Vehicle Experiment II," *International Planetary Probe Workshop 2010 (IPPW-7), Barcelona, Spain*, 2010.
- [64] R. Dillman, J. DiNonno, R. Bodkin, V. Gsell, N. Miller, A. Olds and W. Bruce, "Flight Performance of the Inflatable Reentry Vehicle Experiment 3," *International Planetary Probe Workshop (IPPW-10); 10th; San Jose, CA; United States*, 2013.
- [65] S. Hughes, J. Ware, J. Del Corso and R. Lugo, "Deployable Aeroshell Flexible Thermal Protection System Testing," *20th AIAA Aerodynamic Decelerator Systems Conference*, 2009.
- [66] J. Del Corso, F. Cheatwood, W. Bruce and S. Hughes, "Advanced High-Temperature Flexible TPS for Inflatable Aerodynamic Decelerators," *21st AIAA Aerodynamic Decelerator Systems Technology Conference and Seminar*, 2011.
- [67] J. Del Corso, W. Bruce, K. Liles and S. Hughes, "Thermal Analysis and Testing of Candidate Materials for PAIDAE Inflatable Aeroshell," *20th AIAA ADS Conference*, 2009.

- [68] S. Hughes, J. Ware, J. Del Corso and R. Lugo, "Deployable Aeroshell Flexible Thermal Protection System Testing," *20th AIAA, ADS Conference*, 2009.
- [69] K. Sutton and R. J. Graves, "A general Stagnation-Point Convective-Heating Equation for Arbitrary Gas Mixtures," *NASA Technical Report NASA-TR-R-376, L-7885*, 1971.
- [70] J. D. Anderson, "Hypersonic and high temperature gas dynamics", *McGraw-Hill*, 1989.
- [71] D. Paterna, R. Monti and R. Savino, "Experimental and numerical investigation of Martian atmosphere entry," *AIAA Journal Space Rockets* 39 2 227–236, 2001.
- [72] R. Savino and G. Pezzella, "Numerical analysis of supersonic combustion ramjet with upstream fuel injection," *International Journal for Numerical Methods in Fluids, Vol. 43, pp. 165–181*, 2003.
- [73] C. Justus and R. Braun, "Atmospheric Environments for Entry, Descent and Landing (EDL)," *5th International Planetary Probes Workshop and Short Course; Bordeaux; France*, 2007.
- [74] "ANSA, ANSA v 13.2.0 User's guide, BETA CAE Systems S.A."
- [75] "MSC Patran Users's Manual, MSC Software Corporation, Santa Ana, CA Version 14.0.018," 2006.